

UNIVERSITÀ DEGLI STUDI
DI MODENA E REGGIO EMILIA

PhD Program in Industrial and environmental engineering “Enzo Ferrari”

Cycle XXXII

*Dynamic modelling and analysis of mechanical systems
operating in the packaging industry*

Candidate: Raffaele Di Canosa

Supervisor: Prof. Francesco Pellicano

PhD Program Coordinator: Prof. Alberto Muscio

Abstract

Dynamic modelling and analysis of mechanical systems operating in the packaging industry

Keywords: Multibody simulation, experimental measurement, complex dynamics, cutting mechanism, vibration analysis

The development of robust and reliable systems in the packaging industry requires the creation and the validation of physical models that can estimate both the mission profile of the components and the sub-assemblies and can provide data related to the status of the system when operating out of the nominal working condition.

The object of the study is a complex mechanical system operating with liquid products filled in a package obtained by overlaying polymeric, metallic and organic materials. The mechanism ensures the execution of several phases, hence it is subjected to multiple stresses, which are both cyclically applied during the standard functioning of the automated machine and which occur randomly in case of deviation from the nominal working conditions.

The study was carried out focusing on three main aspects: the modelling of the entire system and the specific analysis of one of the sub-assemblies, the creation of a test bench for collecting data and validating the model, the correlation of the data with the information provided by the equipment installed on the field.

The mechanical model of the system has been developed using the commercial multi-body software MSC Adams[®]. Due to the complexity of the mechanism, the analysis of the kinematic and the dynamic response of the system was executed by incremental steps, reducing the assembly in simpler sub-systems and evaluating their behaviour in operating conditions which were representative of the real application, even if they were less complex. The achievements and the characteristic parameters identified in the simplified models were extended to the entire system, in order to improve the model and tune the calculated response based on the measurements collected.

One part of the analysis was focused on one specific subsystem, which had the function of cutting the material used for the packaging of the products. The study investigated the parameters competing to the cutting efficiency.

The coherence between the mechanical model and the physical system was investigated and validated by the measurements collected on a test rig. The testing equipment was a simplified version of the real mechanism, that was able to emulate the majority of the stresses applied in the operative life of the machine. Customized sensors were designed and manufactured in order to measure some of the forces exchanged among the sub-assemblies of the system.

The kinematic response of the model was used for defining in terms of time and space the sequence of the events which characterize the system and for identifying the impulsive forces that the sub-systems exchange with the frame, that was equipped with some accelerometers.

The correlation between the sequence of events calculated with the virtual model and the data collected with the accelerometers, required the simplification of the system, first by decomposing and inhibiting some of the stresses both in the model and in the test rig and then applying them in sequence up to the full integration in the complete system. The results were then compared with the data provided by a healthy and damaged system.

Modellazione ed analisi di sistemi meccanici operanti nell'industria del packaging

Lo sviluppo di sistemi robusti ed affidabili operanti nel settore del packaging non può prescindere dalla creazione di modelli virtuali che, quando validati su sistemi fisici, possano stimare e prevedere il comportamento di componenti e sotto sistemi operanti sia in condizioni operative nominali che al di fuori delle stesse.

Il sistema analizzato dal presente studio è un complesso meccanismo facente parte di un macchinario industriale utilizzato per l'impacchettamento di liquidi in un involucro polia-coppiato, la cui componente principale è il cartone. Il meccanismo adempie a più fasi del processo di impacchettamento, risultando pertanto sollecitato sia dai carichi ciclici e ripetibili generati durante il normale funzionamento, che forze create dall'interazione tra i sottosistemi ed il prodotto a causa di una variazione rispetto alle condizioni nominali di esercizio.

Lo studio può considerarsi suddiviso in tre aree principali: la prima, riguarda la creazione di un modello virtuale dell'intero sistema, all'interno della quale ha trovato un particolare spazio di approfondimento l'analisi uno specifico sottoassime, la seconda riguarda la realizzazione di un banco prova, il cui scopo principale è la validazione del modello virtuale, e la terza riguarda la correlazione tra i dati campionati dal banco prova e quelli provenienti dai macchinari installati negli stabilimenti produttivi.

Il modello virtuale del Sistema è stato sviluppato utilizzando il software commerciale multi-body software MSC Adams®. A causa della complessità del meccanismo, l'analisi cinematica e meccanica è stata sviluppata in modo incrementale, partendo dal sottoassime più semplice e valutandone la risposta quando sollecitato in un ambiente rappresentativo delle reali condizioni operative, ma semplificato. I risultati ottenuti nel sottoassime sono poi stati estesi all'intero sistema, al fine di migliorare la corrispondenza tra i risultati ottenuti con il modello virtuale e quelli ricavati sperimentalmente.

Una sezione dello studio è stata dedicata al sottosistema a cui è deputata la funzione di taglio del materiale dell'imballaggio, focalizzandosi sui parametri che principalmente influenzano l'efficienza di taglio.

La realizzazione del banco prova rappresenta una fase fondamentale per l'analisi del Sistema e la raccolta dei dati necessari alla validazione del modello. Il banco prova è una versione semplificata del Sistema reale, ma sufficiente per replicare la maggior parte delle sollecitazioni

gravanti sull'attrezzatura nella reale vita operativa. Il campionamento di dati dal banco prova, ha richiesto la realizzazione di sensori speciali, che potessero essere installati al posto di elementi strutturali del sistema e fornire informazioni in merito alle forze scambiate tra i diversi sotto assiemi.

Le caratteristiche cinematiche del sistema sono state utilizzate anche per esaminare le fasi operative sia in un dominio spaziale che temporale, identificando le sollecitazioni impulsive dovute all'interazione dei sottosistemi e correlandole ai segnali forniti da degli accelerometri installati sul telaio del banco prova. La correlazione di tali dati ha richiesto un approccio analogo a quello adottato nel modello virtuale, partendo quindi da una semplificazione delle sollecitazioni agenti sul sistema ed una successiva composizione fino al raggiungimento del livello di sollecitazione completo. I risultati sono stati poi confrontati con i dati provenienti da sistemi sani e danneggiati.

Contents

1	Introduction.....	8
1.1	Tetra Pak®.....	9
1.2	Packaging Material & Package.....	10
1.3	<i>Filling Machine</i>	Error! Bookmark not defined.
2	Dynamic Model.....	13
2.1	<i>Jaw System Unit</i>	13
2.2	Preliminary considerations	14
2.3	Virtual Model	17
2.3.1	Frame	17
2.3.2	Tensioner.....	19
2.3.3	Wheel	20
2.3.4	Transversal Link Pressure Chain.....	21
2.3.5	Transversal Link Sealing Chain	25
2.3.6	Chain Link.....	26
3	Dynamic Model Analysis and Results	28
3.1	Main Cams	28
3.2	Tensioner.....	31
3.3	Volume Box.....	32
3.4	Folding Flap.....	34
3.5	Wheel	35
4	Experimental Result and Model Validation.....	36
4.1	Instrumental set-up.....	36
4.2	Ball Bearing Load.....	37
4.3	Results	40
4.4	Cutting Force	43
4.5	Cutting Direction (0°)	46

4.6	Volume Box and Folding Flap load.....	58
4.7	Tensioner.....	61
5	Operations out of the nominal conditions.....	64
5.1	Tensioner Spring.....	64
5.2	Volume Box Spring	65
5.3	Volume Box damper	65
5.4	Folding Flap Pin	68
6	Cutting <i>Knife</i>	70
6.1	Test Rig	71
6.2	DoE	75
6.3	Cutting Model.....	83
6.4	Degradation Model	92
6.5	Test rig set up	93
7	Experimental Testing of Ball Bearings	99
7.1	Test Rig	99
7.2	Results	102
8	Vibration Data Analysis	112
8.1	Maintenance Strategies	113
8.2	<i>Filling Machine</i> Equipment.....	115
8.3	FMECA and Field Data	115
8.4	Virtual Model	117
8.5	Vibration Data: Test Rig	119
8.6	Vibration Data: <i>Filling Machine</i>	125
8.7	Fault Injection.....	128
9	Conclusion	134
10	References.....	140

1 Introduction

The industrial sector of the automatic machines represents a really challenging environment for the manufacturers, who have to deliver customized solutions for fulfilling the customers' cogent requirements.

The explosion of the Industry 4.0 and the IoT drives the development of equipment characterized by an increasing integration of the traditional mechanics with mechatronic devices: cams are gradually replaced by the virtual ones, mechanisms by servomotors, physical settings by adaptive controls, which are able to minimize the degradation of the operating parameters.

The number of sensors installed into the equipment is exponentially growing, in order to provide sudden feedbacks to the online controls and to recover the nominal working conditions. The machines are required to be able to auto-diagnose their status, monitor the degradation of the operating parameters and predict their failure.

The final target of such increasing complexity is the customer's satisfaction, that is achieved through a reliable and perfectly operating system, that minimized the production lost because of unexpected failures, the unplanned stops, the duration of the maintenance operations, the down time caused by the spare parts procurement and the high maintenance costs related to the early replacement of components that are not achieving the target lifetime.

Delivering highly reliable systems in a context where the machines are strongly customized and almost unique, requires to the manufacturer a strong effort in designing and modelling the equipment, in order to have a solid base for the reliability calculation, the definition of the proper maintenance intervals, the identification of the correct thresholds for the prognostic and the predictive maintenance, the investigation specific operating conditions that might be led the system out of the nominal ranges generating additional failures, support the trouble shooting of issues occurring during the working life of the machine.

The object of this work concerns the development method and its application for the design and validation of reliable machines, in a closed loop with the data provided from the field. Starting from the modelling of a sub-system of the equipment, then the creation of special sensors for monitoring some of the stresses applied on the mechanism, the investigation of the failures claimed on the field, the development of a test rig for the lifetime testing of components

in the real operative conditions and the analysis of signals for monitoring the status of the equipment.

1.1 Tetra Pak®

Tetra Pak® is the world's leading company that provides “hand-to-hand” solutions from the processing to the packaging of food and the services for keeping highest performances of the lines. It was founded by Dr. Ruben Rausing in 1951 and it is present all over the world with more than 24'000 employees.



Figure 1: Tetra Pak Process Line

Delivering food solutions means that the Company owns knowledge and experience in designing, manufacturing and operating lines that starting from the raw product can supply the final package folded and ready for the distribution.



Figure 2: Packages Portfolio

Tetra Pak®’s motto “PROTECTS WHAT’S GOOD™” reflects its vision of making food safe and available everywhere, focusing on keeping the consumption of all raw materials and energy to a minimum during both the manufacturing process and distribution, by driving a sustainable approach both in the product lifecycle and the process for the environmental innovation.

1.2 Packaging Material & Package

The packaging material is part of the Tetra Pak® core business and it is interested in a continuous process of improvement for matching Customers' sustainable requirements. The packaging material should ensure the safety and the quality of the filled product for its entire shelf life, guaranteeing the mechanical strength of the package, the hermetic tightness and the commercial sterility, acting as barrier against the micro-organisms.

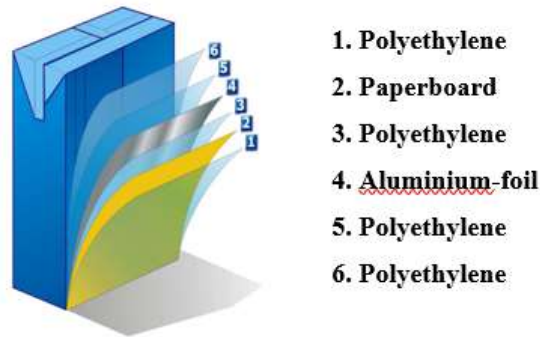


Figure 3: Packaging Material Structure

The packaging material has a multilayer structure, where each element has a specific task for achieving the required performances: the Polyethylene (1) protects against the environmental moisture, the Paperboard (2) is needed for ensuring the mechanical stability and strength of the package, the second layer of Polyethylene (3) operates as bonding element, the Aluminium-foil preserves the flavour of the product, acting as oxygen and light barrier, the third (5) and the fourth (6) layers of Polyethylene are needed for sealing the product and bonding the Aluminium-foil.

The packages can have a wide variety of shapes and dimensions, but they are all characterized by three regions that are indispensable for their production: the top and the bottom sealing, along the transversal direction of the package and the front sealing along the longitudinal one.

1.3 Filling Machine

The *Filling Machine* is a part of the production line and its function is to shape the package and fill it with the product, which has already been blended in the previous phases of the process.



Figure 4: Filling Machine

The *Filling Machine* operates with flat reels of packaging material that are loaded from the back of the equipment. The first operation in the *Filling Machine* is unrolling the reel and sealing a strip that is needed for bonding the two edges of the packaging material in the further operation, when needed, part of the cap is applied when needed, by indexing the packaging material and injecting the polyethylene through the Aluminium-foil. The upper part of the *Filling Machine* is assigned to the cleaning and sterilization of both the packaging material and the environment into the *Filling Machine*, in order to ensure the sterility of the product. In this environment the packaging material is rounded along the longitudinal direction, shaping a tube and sealing the edges by the strip previously applied, in order to obtain the tightness of tube; once the sealed area is cooled down, the product is filled into the packaging material tube, that is pulled by the mechanism “*Jaw System*” that is placed in the lower part of the *Filling Machine*. Aside the aseptic system at the upper level, there is a module that supplies all the utilities needed for operating, sterilizing and cleaning the equipment.

The *Jaw System* has multiple tasks beyond pulling the tube: it seals and separates the top and the bottom of two subsequent packages, preventing any contamination from the external environment, and forms the side panels of the package.

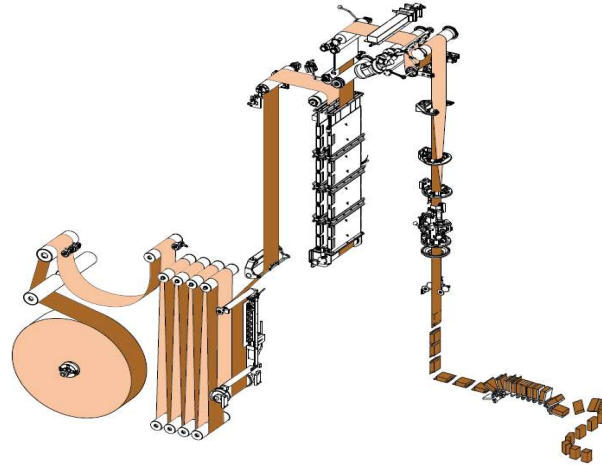


Figure 5: Package Forming Process

The package realised by the *Jaw System* is completely sealed and the product is totally isolated by the external environment, but it has not the final shape yet. The last sub-system of the *Filling Machine* bend the corners of the package and it bonds them to the lateral panels, so that the package is completed and ready for the further phases of the line, like applying the cap, grouping and wrapping multiple packages and palettizing the boxes.

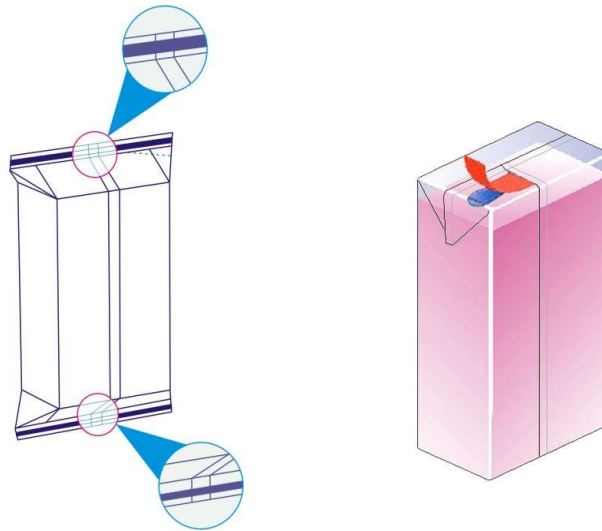


Figure 6: Package released from the *Jaw System* (left) and final package (right)

2 Dynamic Model

2.1 *Jaw System Unit*

The *Jaw System Unit* is the sub-system investigated in this work due to the criticality of the unit for the overall functionality of the *Filling Machine*.

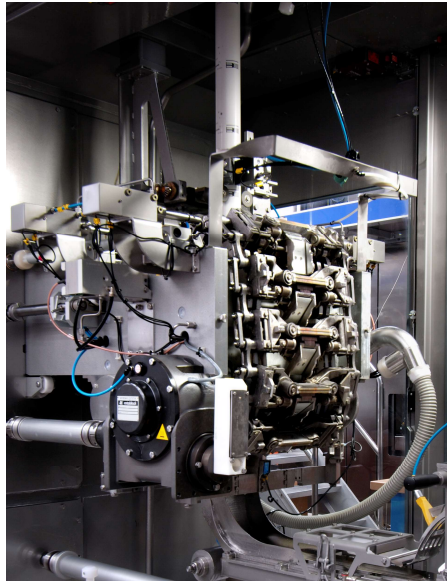


Figure 7: Jaw System

The *Jaw System* consists in two paired *Chains* that are carrying multiple mechanisms on the transversal elements for completing several operations on the package.

The system has in input a tube of packaging material with the product inside and delivers sealed and filled bags, shaped on the lateral panels.

The phases covered by the transversal links of the chain in one complete turn of the chains are:

- Clamping of packaging material
- Pulling and forming the flaps
- Forming the lateral panels
- Sealing
- Cutting
- Releasing

The *Jaw System* was modelled with the commercial multibody software MSC ADAMS®.

The *Chains* are identified as *Sealing Chain* and *Pressure Chain*, since the first one houses the components for executing the transversal sealing and the other the mechanism for clamping and cutting the paper tube.

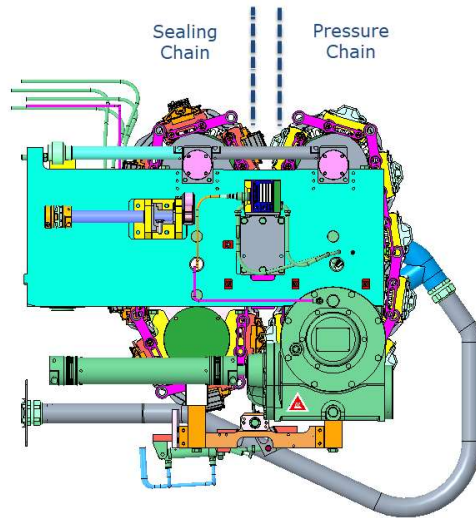


Figure 8: Sealing and Pressure Chains

2.2 Preliminary considerations

The creation of the model started in the PTC Creo[®] environment, where after the assignation of the material properties to all components, they were merged in equivalent bodies having the resulting geometrical and inertial characteristics of the assembled elements, which were then imported in the MSC ADAMS[®] environment in *Parasolid* format.

The software MSC ADAMS[®] was selected for the creation of the virtual modelling of the *Jaw System* due to its suitability for the dynamic analysis of complex mechanical systems mainly composed of rigid bodies.

The multibody code supports the design and the verification of the mechanisms by solving the dynamic equations that govern the motion of the system [15]. The fundamental assumption of the multibody analysis concerns the interactions among the bodies, which are considered to be rigid bodies, hence their deformation is not computed in the gross displacements of the elements.

The bodies of the system are connected by the definition of the joints and contact interactions [10], that limit the degree of freedom that are assigned by default assigned to each body, satisfying the Kutzbach Criterion for the calculation of the degree of freedom of the complete mechanism.

The joints are mathematically defined as set of equations that inhibit specific degree of freedom and they are considered ideal connections, thus any phenomena related to deformation, clearance, lubrication, wear, etc. is excluded. Although, the MSC ADAMS® software allows the possibility of implementing the friction contribution [13]. Three models of friction can be implemented, depending on the magnitude of the relative speed between the bodies connected by that joint. A user defined *Stiction Transition Velocity* is the variable adopted for selecting the friction model among: *Dynamic friction*, if the magnitude of the joint velocity exceeds 1.5 times the *Stiction Transition Velocity*, and in this case the equation adopts the dynamic coefficient of friction for the computation of the frictional forces. The *Static Friction model* is applied when the velocity of the joint is below the *Stiction Transition Velocity*, in this case the static friction coefficient is used for the calculations. The last model is a transitional one, that is adopted when the ratio between the velocity of the joint and the *Stiction Transition* one is in the range [1,1.5]; in this case the model applies a *STEP* function between the static and dynamic states.

More sophisticated models available in literature approached the problems related to the clearance and the nonlinearities of the joints with different strategies, such as either adding a degree of freedom in the ideal massless joint, or assuming a connection between the jointed bodies type spring-damper, which however required the definition of the stiffness and damping coefficient, that increase the complexity and the robustness of the model, or defining contact forces between the connected bodies.

The contacts between the parts can be modelled in MSC ADAMS® by means of two functions, the *IMPACT* and the *RESTITUTION* methods, which are penalty algorithms, defined as a force applied to a unilateral constraint [5],[12].

The contact force is activated when the distance between the bodies becomes lower than the no-penetration distance, characteristic of the rigid bodies, and the magnitude of the forces is calculated through the gradient of the constraint violation [9].

The method adopted in the dynamic model is the *IMPACT* one, which requires for its definition the parameters: stiffness, force exponent, damping coefficient and penetration depth.

The stiffness is a function of the penetration of the two bodies and opposes to that, the force exponent describes the evolution of the contact force in relation to the penetration depth, and the damping coefficient is related to the viscous response of the contact.

The graphics in Figure 9 show the correlation between those parameters and the penetration depth.

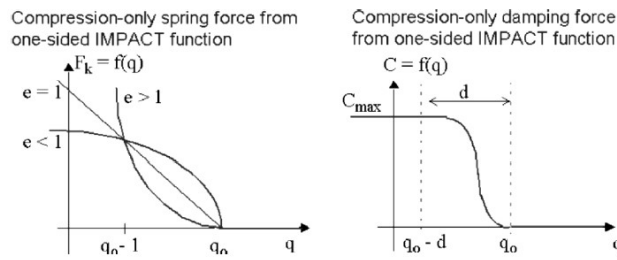


Figure 9: Force Exponent and Damping parameter

The integrator allows the possibility of modelling the friction effect also in the contacts, this element usually contributes to reducing the spikes calculated during the evaluation of the contact forces.

The friction model is calculated on the base of the Coulomb law, hence it is assumed independent from the contact area and correlated to the slip velocity between the parts.

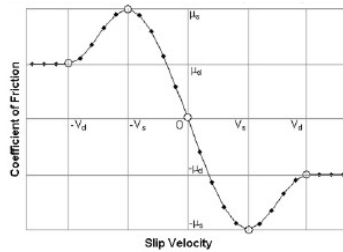


Figure 10: Friction Coefficient definition

The last theoretical aspect that should be recalled is the polygon effect that characterizes the mechanisms with sprockets and chains, as the *Jaw System*.

Depending on the number of teeth of the driving sprocket, the elements of the chain are affected by oscillations of the speed that are related to the polygon that the chain describes when is wrapped to the wheel.

The difference of the speed between the rollers of the chain and the sprocket influence the intensity of the impacts between the bodies [7],[8],[11].

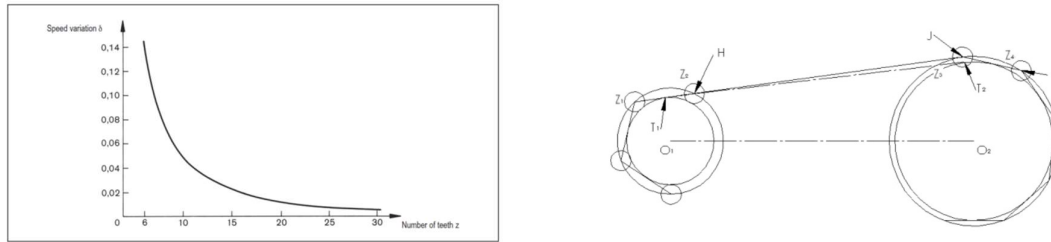


Figure 11: Polygon Effect

2.3 Virtual Model

The system was modelled focusing on the main functions described above, by simplifying all the features that do not directly compete to the operations on the packages.

The following paragraphs provide an accurate description of the system elements and the modelling details.

2.3.1 Frame

The *Frame* is made by four thick aluminium plates, overhung to the body of the *Filling Machine*, eight *Main Cams* (green and grey – Figure 12) made in hardened stainless steel are installed on the transversal plates and they have the function of guiding the displacement of transversal links of the chains.

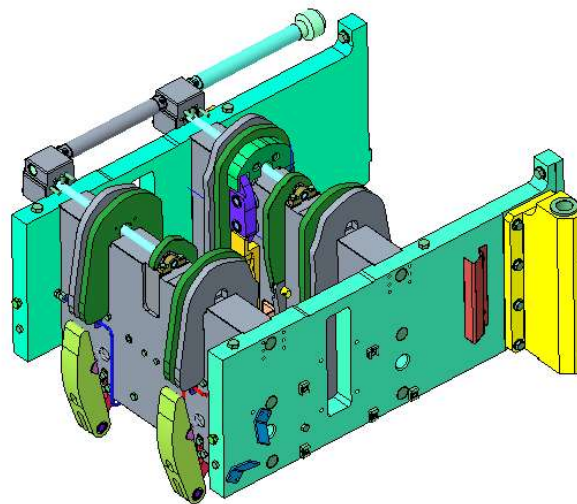


Figure 12: Frame

The *Main Cams* define the trajectory of the *Transversal Links* and during the working cycle are constantly in contact with their cam follower.

The design profiles of the *Sealing* and *Pressure Chains* are symmetric, but the internal (green) and the external (grey) ones on the same side differs each other on the top side, in order to force the rotation of the *Transversal Link* around its own axis (see Figure 13), during the rotation of the *Chains*.

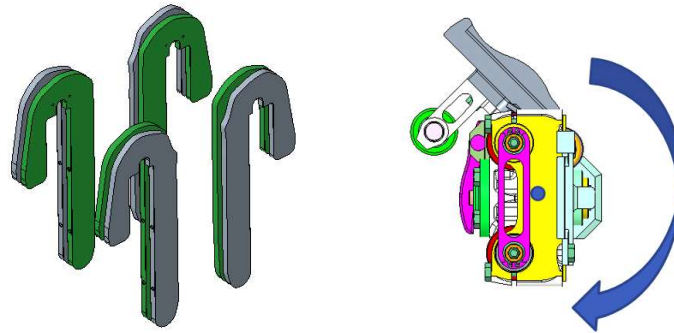


Figure 13: Sealing and Pressure Cam (left), Transversal Link (right)

The *Volume Cams* are installed in the middle section of the frame and their function is to impose the rotation of the *Volume Box* (see Figure 14), during the forming phase of the package, transforming the cylindrical shape of the paper tube into a squared one.

The *Volume Cams* are connected to an eccentric shaft that can regulate their positioning and adjusting the shape of the package. This degree of freedom was not included in the model and a fixed position considered in the simulations.

The *Volume Cams* are manufactured in PA66 reinforced with glass fibres, since they have to withstand to the reaction forces applied by the deforming tube filled with the product and resist the wear applied by the passage of the roller installed in the back of the *Volume Box*.

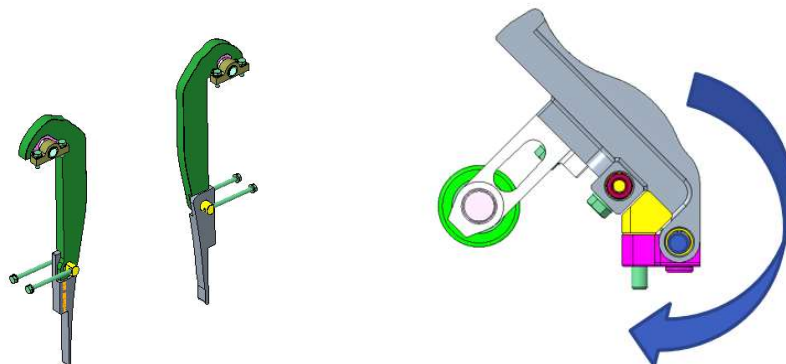


Figure 14: Volume Cams (left) and Volume Box (right)

The *Design Correction Cams* are installed only in one side of the *Frame* and interact with a mechanism installed in each *Transversal Link* of the *Sealing Chain* (see Figure 15). During the

operating cycle the mechanism move two eccentric shafts that pull and press the corners of the package while the *Volume Boxes* are completing their approaching displacement.

The *Design Correction Cams* are connected to an eccentric shaft driven by a servomotor, which control the actual closing angle of the mechanism, as for the *Volume Cams*, this degree of freedom was not included in the dynamic model.

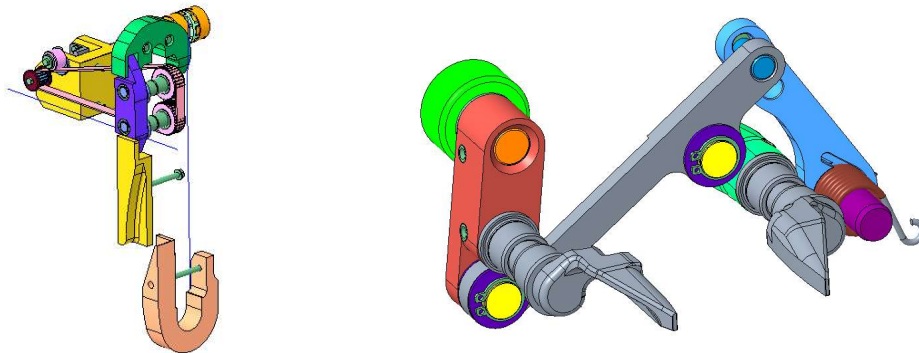


Figure 15: *Main Cams* (left), *Volume Cams* (middle), *Folding Flap Cam* (right)

The *Design Correction Cams* are manufactured in POM, which is an acetal polymer that ensures high resistance both to the mechanical and the environmental stresses, as well as low friction values.

The frame was modelled as a fixed element connected to the ground in the MSC ADAMS® dynamic model.

2.3.2 Tensioner

Four identical *Tensioners* are installed along the trajectory of the cam followers of the *Transversal Links*, for recovering the fluctuations of the loosen branch. The tensioner is loaded with a compression spring, that in the model was reproduced as an elastic force between the frame and the tensioner.

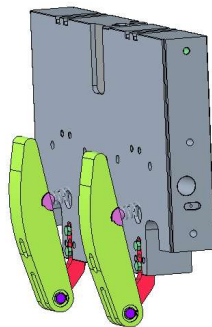


Figure 16: *Tensioner*

The *Tensioner* is manufactured in Ultra-High Molecular Weight Polyethylene plastic, which should ensure mechanical resistance to the passage of the cam followers installed in the *Transversal Links*.

In the dynamic model, the *Tensioners* were connected to the ground, as well as the frame, and the elastic effect of the spring was obtained by replicating the characteristics of the real components adopting a *Spring Element* that is pre-defined feature in the MSC ADAMS® environment.

The *Spring Element* is a massless element acting between two bodies and it is defined between two *Markes* belonging to each of those. The *Markers* define direction for the application of the force, hence a functional prerequisite for the usage of this feature is that they are never overlapped during the execution of the simulations. The force exchanged between the two bodies has a positive value when it repels the parts and a negative value when those are attracted.

The formulation for assigning of the magnitude to the *Spring Element* is:

$$F_{sp} = -k(q-q_0) -c q_0' + F_0$$

That is based on the combination of the parameters: F_0 , that refers to the preload applied in the reference distance q_0 , in the assembling configuration of the bodies; k , that represents the stiffness of the spring; c , that is the viscous damping coefficient, which define the proportionality with the relative speed of the *Markes* along their connecting direction, q_0' .

The real component is characterized by a stiffness $k= 4.88$ N/mm and the preload achieved in the installed configuration is 122.5 N. The damping coefficient is not a parameter provided by the manufacturer's datasheet, hence it was assumed a value of $c= 5e-3$ Ns/m, according with the best practices adopted in the MSC ADAMS® modelling environment, which suggest damping values in the range of [1e-3, 1e-2].

2.3.3 Wheel

The driving system is constituted by four sprockets coupled two by two on the same shaft, that simultaneously engage the two extremities of the transversal links of the chain. The motion is provided by a servomotor connected to the *Pressure Chain* trough the worm gear box installed in the left side of the *Jaw System*. The motion is transferred to the *Sealing Chain* by means of male/female connectors that are installed in the front side of the *Transversal Link*, which ensured the synchronization of the two *Chains*.

The *Wheels* are manufactured in POM, since during the operating cycle should get in contact with hardened stainless steel element and drive the *Chains*.

The operating speed of the equipment is defined by the hourly production rate of the *Filling Machine* and the nominal operating speed of the equipment investigated herein is 24'000 package per hour.

The production speed is kept stable by a closed loop on the position of the chain, which ensures negligible fluctuations of the rotating speed of the *Wheel* and the repeatable cyclic period of the *Jaw System*.

The operating speed of the *Wheel* adopted in the dynamic model is $\omega=533\text{deg/s}$.

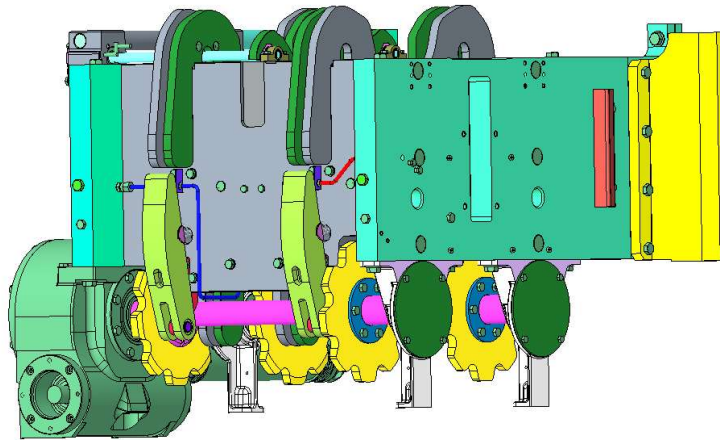


Figure 17: Driving Wheels

2.3.4 Transversal Link Pressure Chain

The *Transversal Link* of the *Pressure Chain* is a rigid element with a “dog-bone” shape, optimized for increasing the ratio stiffness/weight and minimising the deformations in the normal direction in reference to the displacement. In the extremities of this element there are the seats for the shaft that carry the cam followers (red elements – Figure 18), which are rolling on the *Main Cams* and on the *Tensioner* [14].

In the dynamic model the interaction between the cam followers and the cams have been modelled as *Solid-to-Solid* contacts, in order to ensure properly emulate the dynamic evolution of the system. The parameters adopted for the definition of the contact are listed in the Chapter 3.

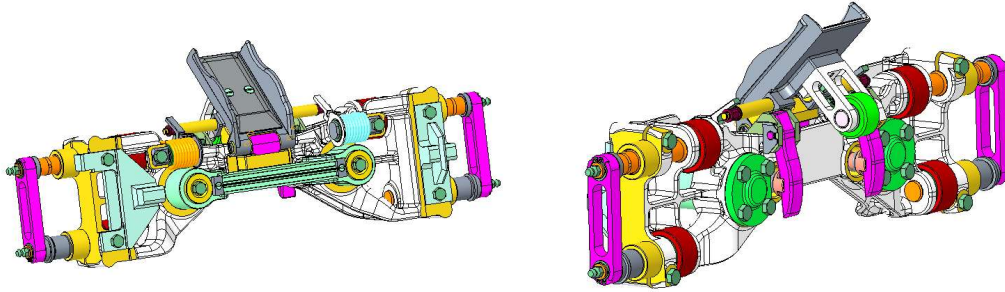


Figure 18: Transversal Link - Pressure Chain

The *Volume Box* (grey box – Figure 18) is installed on the top of the transversal link by means of a hinge, it has the shape of half of parallelepiped and carries on the back a ball bearing that is rolling on the Volume Cams, driving the approaching displacement to the packaging material [1], [2].

The load applied on the mechanism and the *Volume Cam* is mainly influenced by the resistance of the paper tube to the imposed deformation and the hydrostatic load of the column of product embedded into the paper tube.

The model included the contact between the roller on the back of the *Volume Box* and the *Volume Cam* as *Solid-to-Solid* contact, in order to capture the dynamic of the assembly during the all the phases of the cycle.

The *Volume Box* is kept in the backward position by two torsional springs installed on the grey levers and acting on the yellow shafts that are installed on the sides of its body. The springs were modelled as *Spring Elements*, which as in the former case of the *Tensioner* were defined adopting the design data provided by the manufacturer datasheet. In order to simplify the model, due to the symmetricity of the system, the spring and the grey levers were replaced with a single equivalent spring, that ensured the same torque on the *Volume Box* [3], [4].

The stiffness of the spring is $k=14.5$ N/deg the preload in the equilibrium configuration $F_0=955$ Nmm and the damping coefficient was assumed to be the same that the spring of the *Tensioner* $c= 5e-3$ Nmms/deg.

In the equilibrium configuration, the *Volume Box* leans on a damping element made in Polyurethane, which has a critical function for arresting the opening stroke of the *Volume Box* at the end of the forming phase and limit the stresses applied on the joint section, since highly intense hurts might determine critical stresses and produce fatigue failures.

The contact between the *Volume Box* and the damper was modelled as a *Point-to-Plane* contact, the main reason for selecting this type of contact was related the effect that the low value of stiffness of the polyurethane produces on the equilibrium position of the system under the load of the springs.

In order to properly identify the relative position between the *Volume Box* and the damper in the equilibrium configuration, the sub-system was preliminary analysed with a Finite Element Analysis. The graphics in the Figure 19 show the Stress (MPa) and Deformation (mm) fields calculated for the damper constrained on the bottom as in the final installation position and loaded with a uniform force on the sloped plane that is the interaction surface with the *Volume Box*.

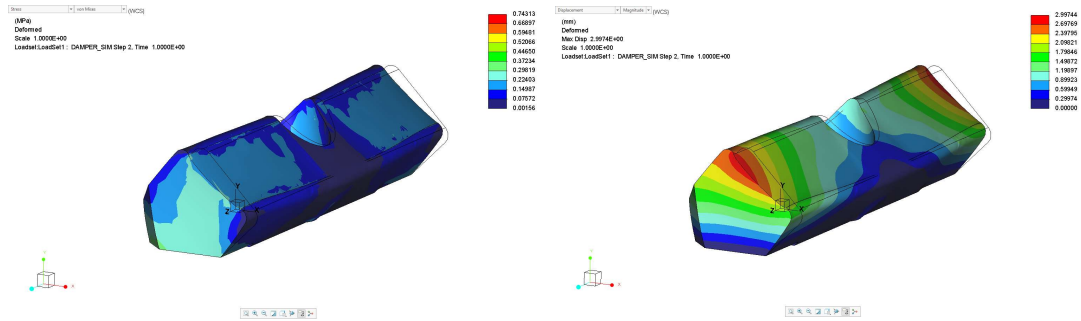


Figure 19: Damper: Stress and Deformation Fields

The contact with the paper tube was modelled as the combination of an impulsive force, representing the first contact between the tube, and a growing force associated to the tube deformation and the hydrostatic load deriving from the column of the product.

The formulation of the IMPACT Force is defined by the variables:

$$\text{IMPACT}(q, \dot{q}, q_0, k, e, c_{\max}, d)$$

The impulsive force was creating as acting between the *Volume Box* and a fixed position of on the ground and a *Point-to-Point* measure was adopted as variable for activating the function. The reference kinematic parameter considered was the relative speed between the *Marker* on the approaching *Volume Box* and the fixed one.

The other contribute to the forming process, was modelled with a step function, which is defined with the variables:

$$\text{STEP}(q, q_1, f_1, q_2, f_2)$$

The function variable was the again the relative position between the *Volume Box* and the fixed marker, and the activation distance corresponded to the position of the *Volume Box* where the damping effect of the impact function was elapsing.

The values adopted for the definition of the forming forces were based on database data collected on the physical system during former activities.

The lower part of the *Transversal Link* carries the *Cutting Rail*, a sliding element (light green component – Figure 20) that has the function of transferring to the paired *Transversal Link* of the *Sealing Chain* the proper force for pressing the paper tube, ensuring the evacuation of the product from the clamped region, which is crucial for sealing the internal layers of polyethylene of the tube.

The load is granted by the action of two springs, for which the manufacturer's datasheet report a stiffness $k=705$ N/m, and the preload in the installation position is $F_0=2113$ N.

The connection between the *Cutting Rail* and the *Transversal Link* is ensured by two rubber bushings (orange component – Figure 20) , whose effect is crucial for compensating wearing effect and misalignment between the links of the *Sealing* and *Pressure Chains*, however those undesired effect are not included among the degree of freedom of the modelled system, hence the connection of the *Cutting Rail* was modelled with a sliding joint. As for the *Volume Box*, due to the symmetry of the assembly and the selected type of joint, the two springs were replaced with an equivalent one and the assumed damping coefficient $c= 2e-2$ Ns/m.

The loading effect of this spring is transferred to the *Transversal Link* of the *Sealing Chain* as an internal force of the *Jaw System*.

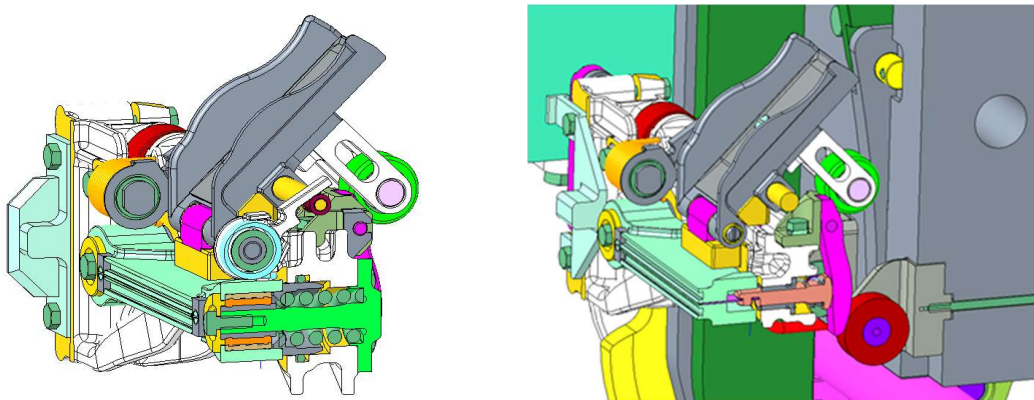


Figure 20: Cross Sections: Pressure System (left) and Cutting System (right)

The *Cutting Rail* guides the displacement of the *Knife* that has the function of cutting the paper tube and separating to subsequent packages. The motion of the *Knife* is driven by the displacement of the two shafts (light orange – Figure 20) moved by the *Cutting Cams* (pink element – Figure 20), when in contact with the ball bearing (red component – Figure 20) that is installed on the frame.

The connection between the *Knife* and the shafts ensures the required backlash for allowing to the *Knife* the possibility of following the movement of the *Cutting Rail*, when aligning with the paired *Transversal Link*.

The position of the *Cutting Cams* is ensured in the backward position by the action of two springs, which were modelled as *Spring Elements* with the characteristics are: $k=7.6$ N/mm, the preload $F_0=45.6$ N and the assumed damping coefficient $c= 5e-3$ Ns/m.

The degree of freedom between the *Knife* and the shaft was not included in the total dynamic model, due to the assumption accepted for the modelling of *Cutting Rail*. Hence the *Knife* was replaced with the effect of the force that exchange with the *Cutting Cam*, adopting a *Spline* defined function, that was shaped on the results of the experimental measurements described in the Chapter 4.

2.3.5 Transversal Link Sealing Chain

The main element of the *Sealing Chain* is similar to the one on the *Pressure Chain*, it rolls on the cam lying on four cam followers, that are symmetrically installed in both *Chains* and the *Volume Box* elements are the same than the ones in the *Pressure Chain*.

The main differences concern the element that is paired with the *Cutting Rail*, that in this side is the *Inductor*, a rigid body which carries the electronic components required for performing the sealing of the top and the bottom of the package. The *Inductor* receives and transfers to the *Transversal Link* the load applied by the springs installed into the *Cutting Rail*.

The other difference concerns the *Folding Flap* mechanism (see Figure 21 and 22), that consists in 4 levels installed in the back of the *Transversal Link* that are connected to 2 eccentric shafts acting on the front against the paper tube.

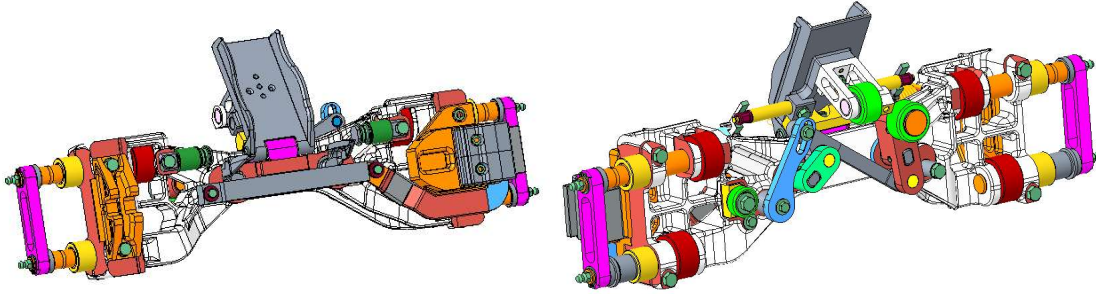


Figure 21: Transversal Link - Sealing Chain

The mechanism is kept in its open position under the effect of a torsional spring, that applies the opening torque on the blue lever and the opening displacement is limited by a mechanical stop that acts on the red lever. The stopping element is made in stainless steel.

In the model the load is replicated with a *Spring Element*, characterized by the values of stiffness $k= 7.15 \text{ N/deg}$, damping coefficient $c= 5e-3 \text{ Nmms/deg}$ and preload in the equilibrium configuration $F_0= 433 \text{ Nmm}$.

The contact between the red lever and the stopping element has been modelled as *Solid-to-Solid* contact.

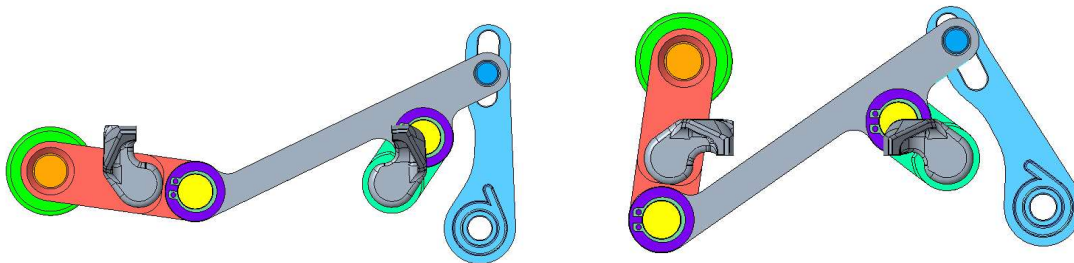


Figure 22: Folding Flap Mechanism in Open (left) and Closed (Right) positions

During the operative cycle, the *Folding Flaps* acts on the paper tube, pulling and pressing the edges of the package; this action was emulated adopting a step function, whose variable were: the angle measurement between the *Folding Flap* and the horizontal plane of the *Inductor*, the ramp duration was set as function of the angle measurement and the magnitude of the force was selected from database data.

2.3.6 Chain Link

The *Transversal Links* are connected each other with the *Chain Links* (see pink element – Figure 23), whose extremities carry a couple of metallic lubricated bushings. The connections

between those bodies were modelled as ideal revolute joints, modelling the frictional contribute with the Coulomb method and adopting the parameters $\mu_s = 0.08$ and $\mu_d = 0.05$.

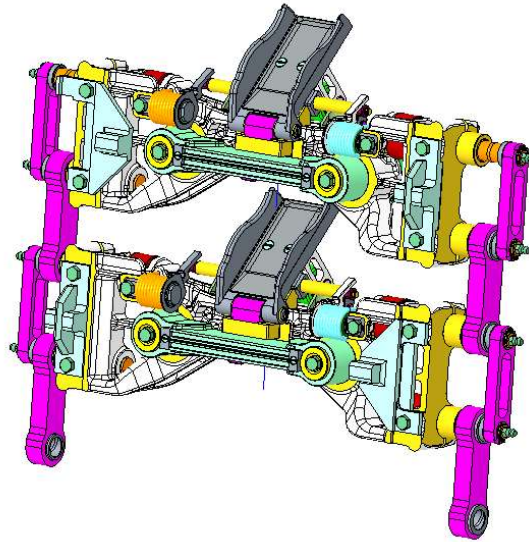


Figure 23: Two Transversal Links and the Chain Links

The Table 1 summarized the parameters adopted for the in the defined cotacts.

Body 1	Body 2	Stiff. [$\frac{kN}{mm}$]	Damp. [$\frac{Ns}{mm}$]	Exp.	Pen. Depth [mm]	μ_s	μ_d
Ball Bearing	Main Cam	85	55	1.50	0.1	0.3	0.05
Ball Bearing	Vol. Cam	4	13	1.9	0.1	0.15	0.08
Ball Bearing	Tensioner	3.7	20	1.8	0.1	0.13	0.08
Shaft	Wheel	5	50	1.55	0.1	0.13	0.09
Roller	F.F. Cam	5	50	1.55	0.1	0.13	0.09
Ball Bearing	Cut. Cam	90	55	1.50	0.1	0.3	0.05
Folding Flap	Pin	85	55	1.50	0.1	-	-
Volume Box	Damper	2.5	90	1.05	0.1	-	-

Table 1: Model Contact Parameters

3 Dynamic Model Analysis and Results

The main purpose for creating the dynamic model of the *Jaw System* was due to the need of understanding the dynamic behavior of the various sub-systems competing to forming process of the package, identifying the eventual criticalities, providing data and specifications for testing the components and mechanisms, for investigating the overall response in case of operative conditions out of the nominal range.

In order to properly tune the response of the dynamic model, the sub-assemblies were firstly analyzed separately, by deactivating in each trial the features and the mechanisms that were not under investigation.

The baseline of the model was considered the *Chain* and its interactions with the elements of the frame that define the trajectories of the *Transversal Links*.

In this configuration of the model, the parameters that should be tuned were the coefficients required for the definition of the contacts.

The parameters adopted in the starting configuration were the one suggested by the MSC ADAMS® Users Best Practices and Guidelines, for the investigating the effects of the variations of those parameters on the dynamic of the system [6].

The contribute of the coefficient of the Stiffness, Damping and Force Exponent were investigated separately by varying the in the range of about $\pm 20\%$ from the starting configuration. The penetration depth was kept to the fixed value of 0.1, that is a commonly used value suggested both in the User best Practices and in literature.

3.1 Main Cams

The matrix of the trials executed for investigating the contacts between the cam followers of the *Transversal Links* and the *Main Cams* on the frame.

Test	Stiffness [N/mm]	Damping [Ns/mm]	Force Exponent
Ref	1 e5	1.5	50
1	1.15 e5	1.5	50
2	8.5 e4	1.5	50
3	1 e5	1.7	50
4	1 e5	1.3	50
5	1 e5	1.5	60
6	1 e5	1.5	40

Table 2: Contact Parameters

The graphics in the Figures 24, 25 and 26 shows the trends of the magnitude of the contact force calculated in the contact between the *Main Cam* and the cam follower installed in the *Transversal Link #10*. The absolute value of the force should be divided by two, since in the dynamic model the contacts were defined for only the *Main Cams* in the left side, in order to reduce the amount of constrains and the computational time.

The graphics in Figure 24 compares the data calculated for the Reference configuration and the Tests #2 and #3, hence varying the stiffness coefficient. The analysis shows the trend of the contact forces computed when the *Transversal Link* is loaded with the clamping force: there are not significant differences among the overall response, whilst the different values of stiffness affects the impulsive accelerations during the sudden variation of direction on the top of the frame (e.g. Time abscissa 0.22s, 0.44s, 0.51s) and in the discontinuities between the elements encountered along the trajectory.

Lowering the value of the stiffness in reference to the one recommended in the User Best Practices Guideline, minimized number of computational spikes.

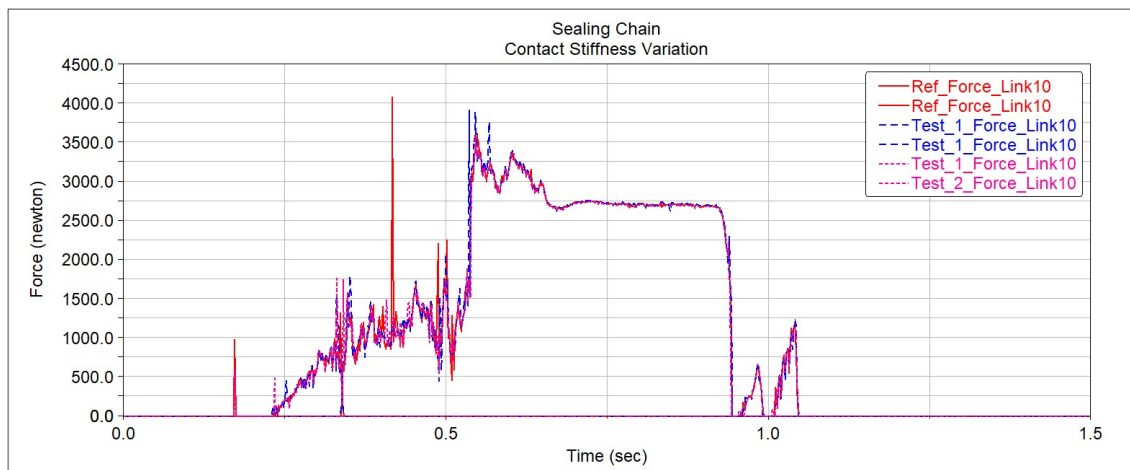


Figure 24: Force Variation with Contact Stiffness

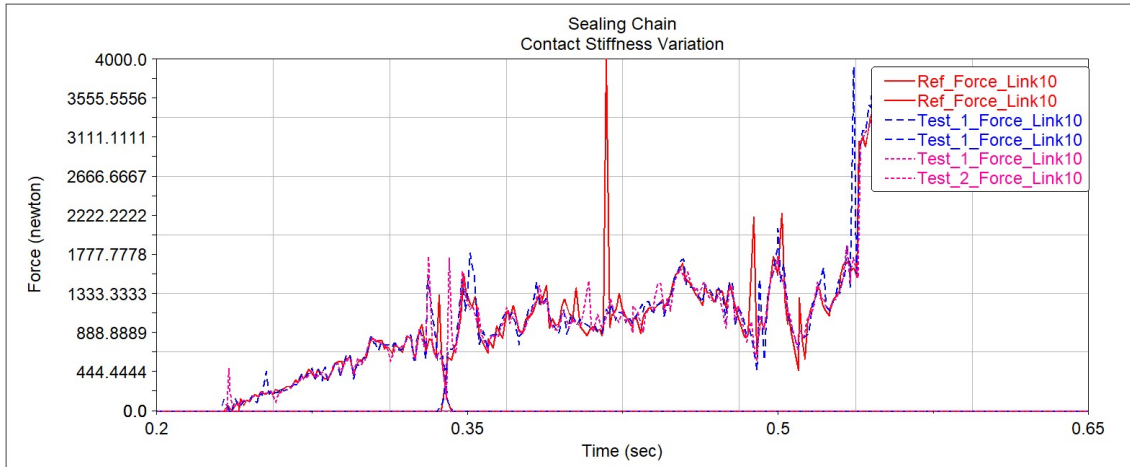


Figure 25: Force Variation with Contact Stiffness - Top of Jaw System

The graphic in the Figure 26 reports the force computed in the contact between the *Transversal Link#10* and the *Main Cams* when varying the value of the coefficient of the Force Exponent. As in the previous case, some differences can be highlighted in the phases where the contact between the parts is driven only by dynamic forces and no additional loads are applied. The trends show that increasing the Force Exponent increases the amount numerical spikes, that are reflected in the plot as sudden accelerations of the examined bodies. The reduction of the value Force Exponent smooths the intensity of some numerical spikes at the first contact between the bodies, while in the residual motion is almost aligned with the Reference trend.

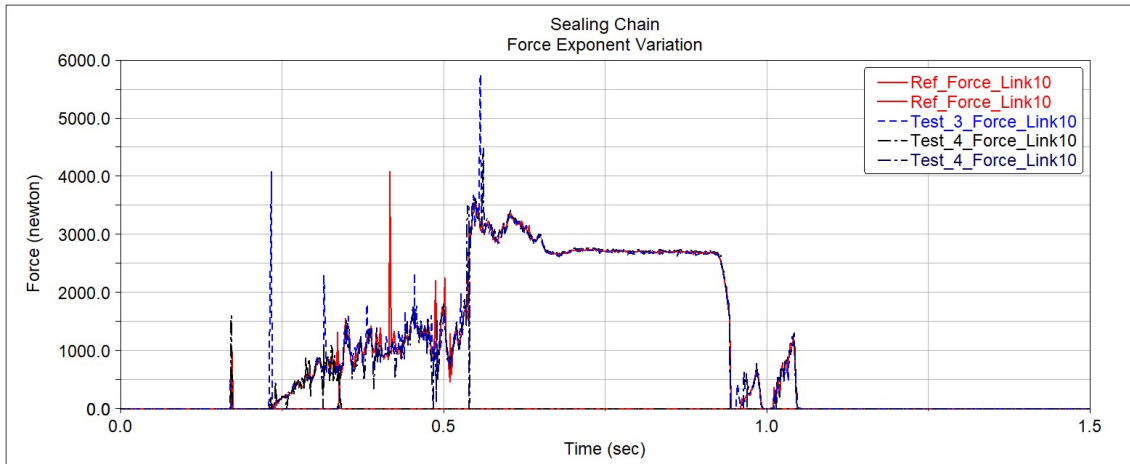


Figure 26: Force Variation with Force Exponent

The last graphic (Figure 27) concerns the values computed when varying the value of the damping coefficient. Some differences can be highlighted both in the region without the clamping load and in the transition zones; the higher value of damping reduces the spikes that are occurring in the transition between the unloaded and the loaded sections, but since in this

section of the trajectory the contact with the paper tube was modelled as an impulsive force, the magnitude of the damping cannot be increased to much, in order to avoid the risk of nullifying the contribution of this load. When reducing the value of the damping coefficient additional spikes can be noticed in the first phase of the contact with the *Main Cam*.

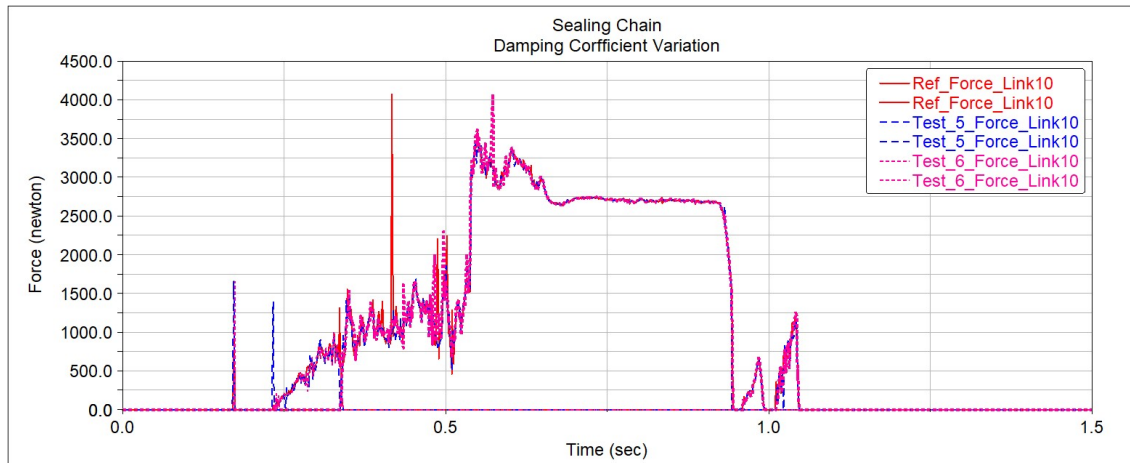


Figure 27: Force Variation with Damping Coefficient

The optimal combination of coefficients was found with the stiffness value $k=85$ N/mm, the force exponent value $e=1.50$ and the damping coefficient $d=55$ Ns/mm, which was validated by means of the experimental data collected by means of a sensing shaft carrying the cam follower, as described in the Chapter 4 .

3.2 Tensioner

The optimization of the contact parameters between the cam follower of the *Transversal Link* and the *Tensioner* element was carried out with the same approach adopted for the *Main Cams*, thus by modifying and combining the characteristic coefficient that best match the forces measured by the sensing shaft of the cam follower. In addition to the force value, the dynamic of the *Tensioner* was monitored by measuring the displacement of the connecting joint of the spring. More details about the experimental procedure are provided in the Chapter 4.

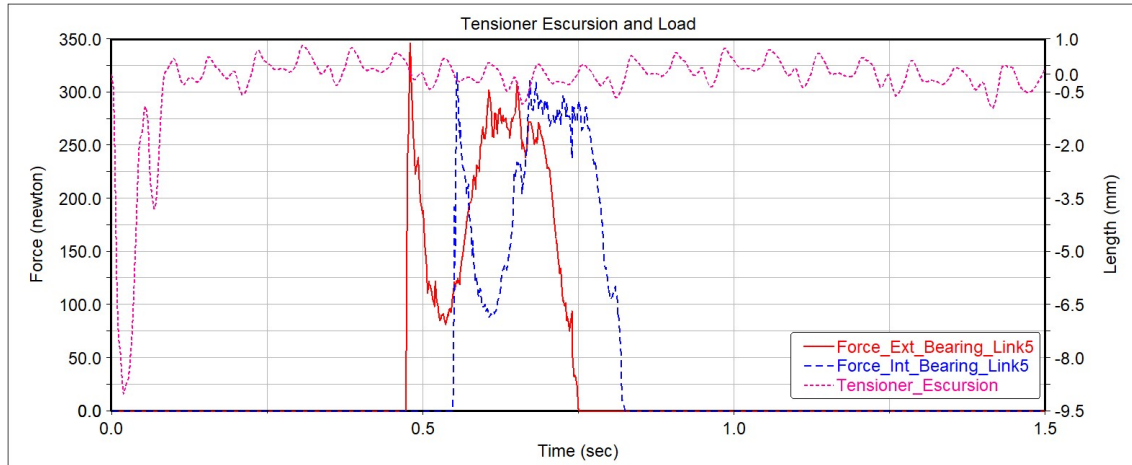


Figure 28: Tensioner fluctuation

The observation of the contact forces calculated for the cam followers belonging to the same *Transversal Link*, shown in the Figure 28, highlights that the trajectory described by the cam followers ensures a smooth contact with the *Tensioner*, since the peak force computed has the same magnitude of the one during the stable contact. A sudden drop of the value of the force of the External Bearing can be noticed after the first contact, which is caused by the contact between the approaching Internal Bearing and the *Tensioner*: the contact between those two elements determines a further rotation of the *Tensioner* towards the frame, that produces the reduction of the contact force on the External Bearing. The analysis of the fluctuation of *Tensioner* position and the correlation with the frequency of the transition of the cam followers and with the drop of force, confirms the interpretation above.

3.3 Volume Box

The contact between the roller of the *Volume Box* and the *Volume Cam* was modelled adopting the contact coefficients which are suggested in the MSC ADAMS® User Best Practice Guidelines, since previous experiences confirmed that they would provide a good representation of the real system. The coherence and the quality of the computed values will be anyhow investigated by means of the sensors described in the Chapter 4.

The trends collected in the Figure 29 describe the value of the contact force calculated on the roller of the *Volume Box* and the angle measured between the back of the volume box and the horizontal plane of the *Transversal Link* (see Figure 30)

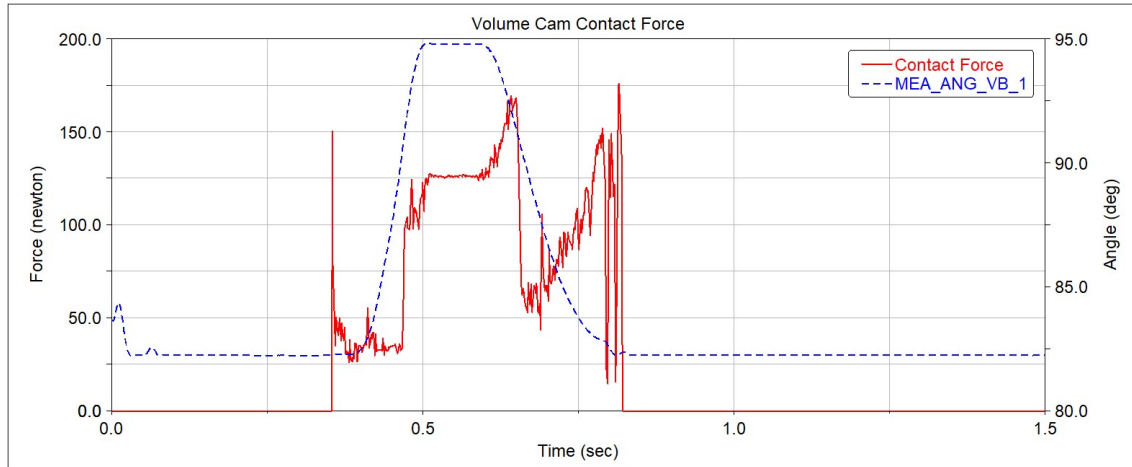


Figure 29: Volume Box Contact Force

The trend of the measured angle demonstrates a stable behavior of the *Volume Box*, that during the rotation of the *Chains* properly follows the profile of the cam, whilst when it is not subjected to any imposed displacement it keeps the position in contact with the stopping damper.

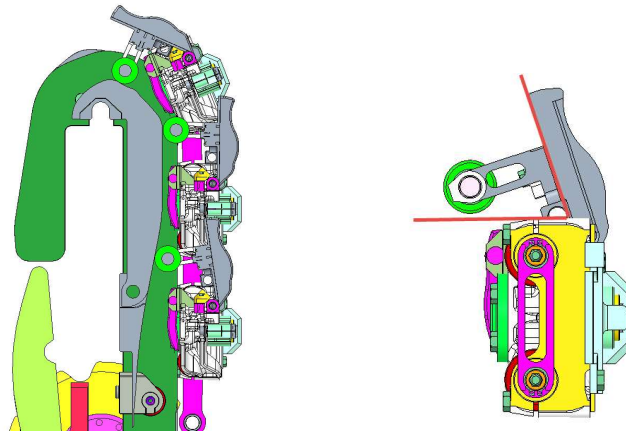


Figure 30: Volume Box Contact Position (left) and reference angle (right)

The peaks identified in the force curve correspond to the first contact between the roller and the cam, that then is stable and generated by the action of the torsional spring, till the *Volume Box* overpass the knee of the cam and starts the contact with the paper tube, the step of the curve was caused by the action of the loading function defined for the forming process. After the plateau, when the *Transversal Link* approaches the change of curvature of the cam a new increasing trend is highlighted, which is likely generated by inertial effects. The subsequent growing rate is then caused by the passage between the two elements of the cam, which although smoothed is still a discontinuity of the profile.

3.4 Folding Flap

The contact parameters adopted for modelling the contact between the *Folding Flap* mechanism and the *Design Correction Cams* were selected among the database data validated in former modelling activities.

The evolution of the force of the contact along the operating trajectory did not show significant stresses applied on the mechanism, with the exception of the first contact with the cam, where an impulsive load is detected by the model.

The stresses generated during this contact did not cause historical issues and the experimental investigation of this area was postponed to future activities, but it has been evaluated as a potential critical section to be investigated in the vibrational analysis described in the Chapter 8.

Over the first impact, the dynamic model highlighted some force spikes, which are generated during the transition between the adjacent cams, but they were not considered critical for the integrity of the mechanism due to the low intensity.

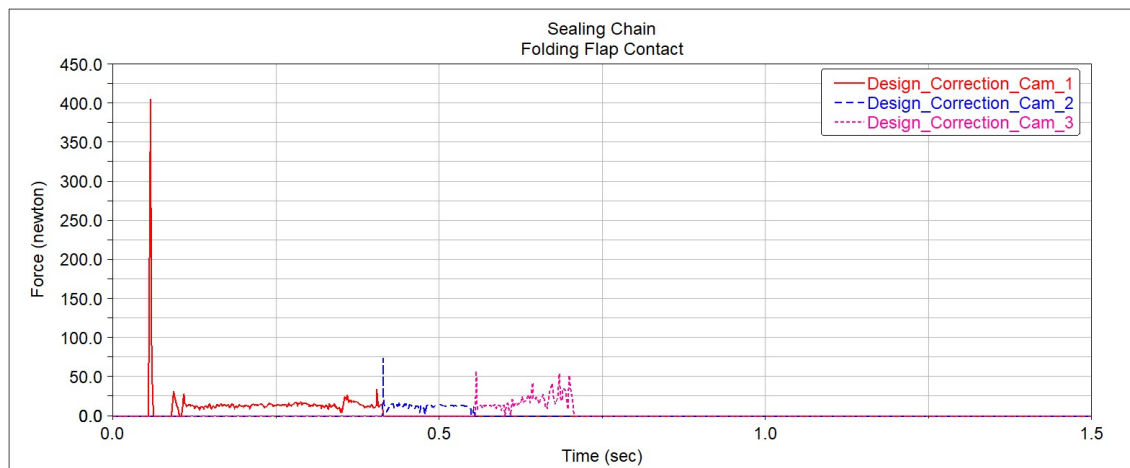


Figure 31: Folding Flap Contact Force

The last observation is related to the results obtained for the contact with the *Design Correction Cam 4*, the one installed in the bottom section of the *Frame*: its function is to ensure that the *Folding Flap* mechanism is properly reopened before releasing the package, and, as confirmed by the simulation, if all the parts of such mechanism are properly working there is not any contact between this cam and the roller of the mechanism, hence it is loaded only in case of failure of other elements of the mechanism.

3.5 Wheel

The analysis of the stresses applied between the wheel and the bushings installed on the *Transversal Link* showed interesting results about the loading cycle of both the bushing and the *Wheel*, that were used for specific activities related to the optimization of the wear resistance those components. As for previous cases, the magnitude of the force should be considered half of the calculated values, under the hypothesis of linearity and perfect symmetry of the *Jaw System*, since for reducing the amount of contacts calculated by the model, only one *Wheel* was modelled.

The graphic in Figure 32 reports the data of only two *Transversal Links* for enhancing its readability, it shows the forces applied on the bushings, which are labelled as A and B according with their position into the *Transversal Link*, and the velocity of the center of mass of the *Link 1*.

The trend of the contact force is characteristic for the sprockets, which follows the frequency the teeth of the *Wheel*, splitting the contact forces between three elements of the *Wheel*.

The bushing B is installed in the rear position of the *Transversal Link* (according with the direction of the motion) and it is subjected to a slightly higher force.

The high magnitude of this contact is correlated with the polygonal behavior of the *Chain*, that is clearly detectable in the fluctuations of the speed of the center of mass of the *Link*, whose highest fluctuation in the first part of the curve is caused by the inversion of the motion occurring in the bottom section of the *Jaw System*.

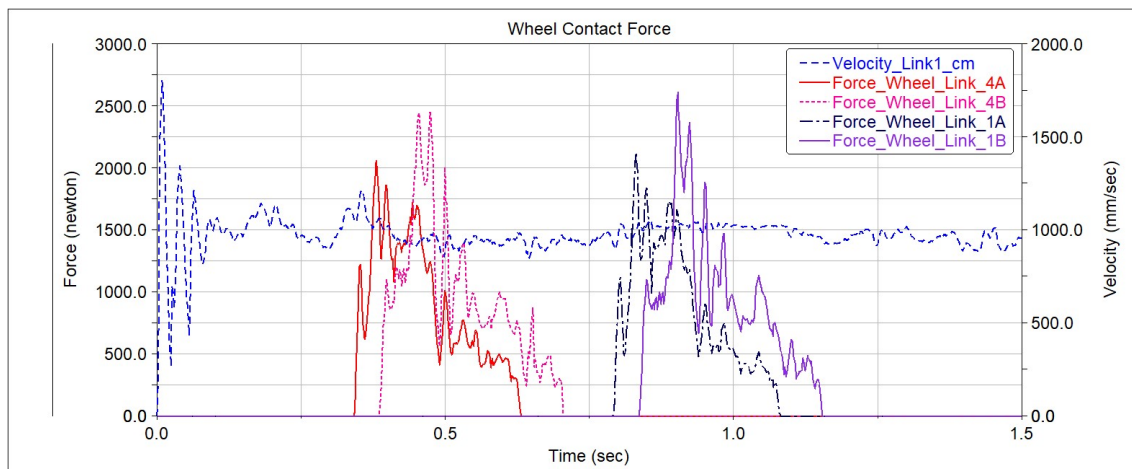


Figure 32: Wheel Contact Force and Link velocity fluctuation

4 Experimental Result and Model Validation

4.1 Instrumental set-up

The validation of the virtual model was executed measuring and monitoring the forces exchanged among some of the components investigated in the dynamic model.

The components of the *Jaw System* detaining the major interest for the collection of experimental data, either for being the ones loaded during the interactions with the packaging material and the product, or the element associated to modelled contact in the virtual environment, are often the most difficult to access.

The limitations are mainly related to three aspects: firstly, the compact layout of the *Jaw System* and the multitude of functions actuated by means of mechanisms, dramatically reduces the availability of space for the installation of standard sensors. The second element is related to the need of collecting data from components of the mechanisms that are installed in the *Transversal Links*, hence it is indispensable to provide both sensors and logging systems that should fulfil in the same time the dimensional and technical requirements for sampling and transmitting the data set at the proper frequencies. The last aspect is related to impossibility of capturing the information related to the interactions with the packages, with the desired level of accuracy, out of the complete systems.

The measurement of the stresses applied among the components of the *Jaw System* required the development of customized sensors that would be able fit the available spaces in the *Sealing* and *Pressure Chains*, since in many cases the available commercial product did not match the requirements.

The priority for developing such kind of sensors was assigned to the sub-systems that would both ensure the highest likelihood of success and allow the possibility of collecting information that could be correlated with the behaviour of the equipment installed in the Customers' plant or with the issues occurring on the field.

The stresses analyzed were:

- Forces applied on the ball bearing that are moving along the *Main Cams*;
- Forces applied on the *Knife* and the connected components during the cutting phase;
- Forces acting on the *Volume Box* during the forming phase;
- Forces applied on the *Folding Flap* during the forming phase;

The criterion adopted for the development of the customized sensors was the modification of the standard components, in order to increasing their deformation under the load deriving from the operating cycle and the application of strain gauges in the modified sections.

Since the sensing elements were the same components of the *Jaw System*, the available space would have been used for installing the logging systems and the power supply.

4.2 Ball Bearing Load

The sensors for measuring the load applied on the ball bearing were developed starting from the design of the shafts that are carrying them.

The *Transversal Link* is characterized by a symmetrical shape and two types of shafts of different length are installed into the assembly: one carries the ball bearing rolling on the *Internal Main Cam* and the other the one on the *External Main Cam*. The expected loads were not significantly different, but both shafts were developed in order to draft a complete picture of the dynamic of the *Transversal Link*.

The shape and the geometry of the shafts were modelled in order to create a localized section with lower resistance to the shear stresses, in order to locally enhance the strain an increase the sensitivity of the measurement (Figure 33).

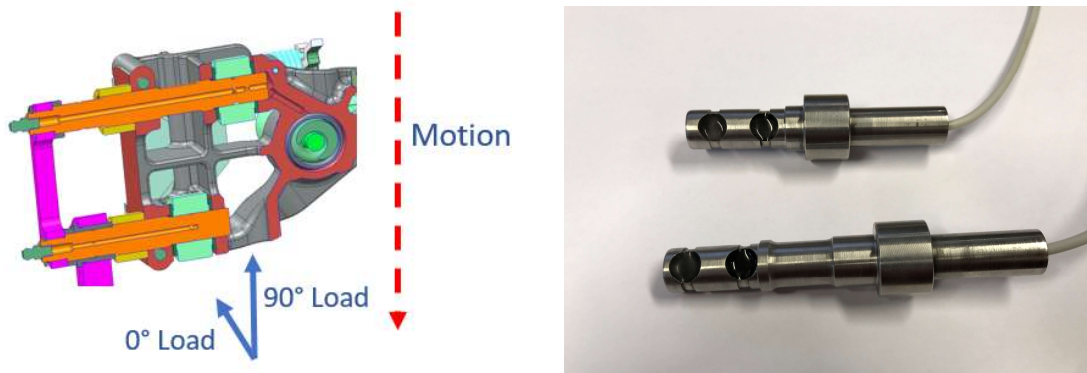


Figure 33: Sensorized Shaft

The geometry of the sensor was studied for optimizing its sensitivity in the normal direction in reference to the trajectory vector (0° Load – Figure 33), but a design constrain was to ensure the mechanical resistance against the estimated load even if rotated 90° into the seat of the transversal element (90° Load – Figure 33). The rationale of this constrain was related to the need of measuring also the load applied along the trajectory direction, that might be present in the physical equipment due to misalignments, assembling tolerances, wear, etc, although any relevant stress was computed by the simulation along his direction.

The application of the strain gauges was assigned to an external company whose core business is the creation of customized sensors.

The Figures 34 and 35 show the stress (MPa) and deformation (mm) fields calculated for the sensors, when constrained in the cantilever configuration, as in the final application, and loaded in the direction normal trajectory (0° Load – Figure 33/34 left) and tangential to the motion trajectory (90° Load – Figure 33/34 right).

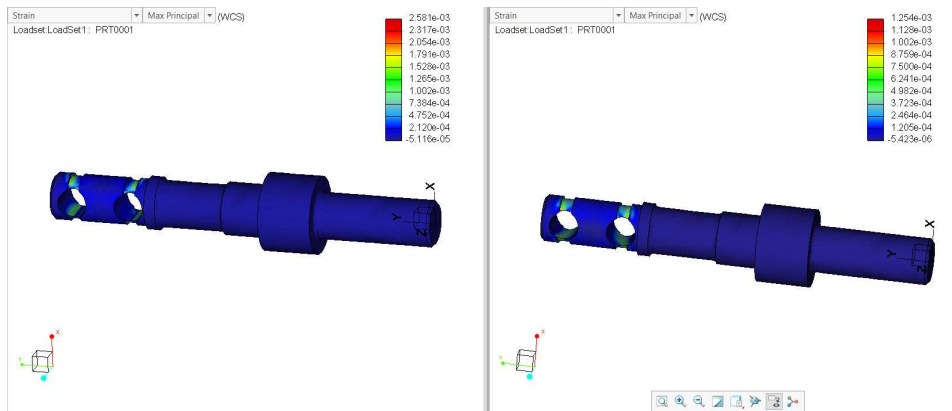


Figure 34: Strain field for of the shaft with the loading orientation at 0° (Left) and 90° (Right)

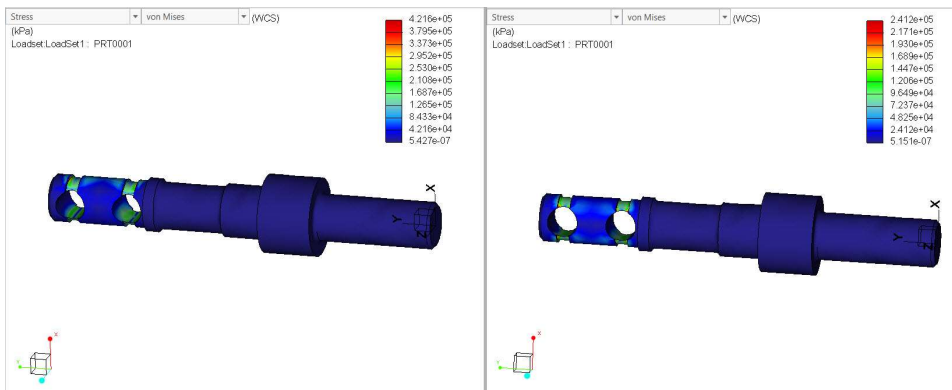


Figure 35: Stress field for of the shaft with the loading orientation at 0° and 90°

The estimated load applied on the bearing was about 1'500N, hence it was dimensioned and verified for resisting to the static load of 3'000N in the two normal directions.

The surfaces that were coupled with the ball bearing and the sections installed into the supports of the transversal element were not modified in order to preserve the configuration of the system and preventing the introduction of noise effects.

The material selected for the sensor was the AISI 630, which was differed from the one used for the standard shafts, but it allowed a smaller cross section and a wider availability of space in the area of application of the sensors, because it has a higher yield strength. Due to the short

duration of the measuring campaign and the reduced amount of stressing cycles that the sensors should withstand, the risk of fatigue breakage was considered negligible.

The calibration of the sensors was executed keeping the shaft installed into the transversal link (Figure 36), in order to compensate the effects of potential preloads generated while assembling the sensors.

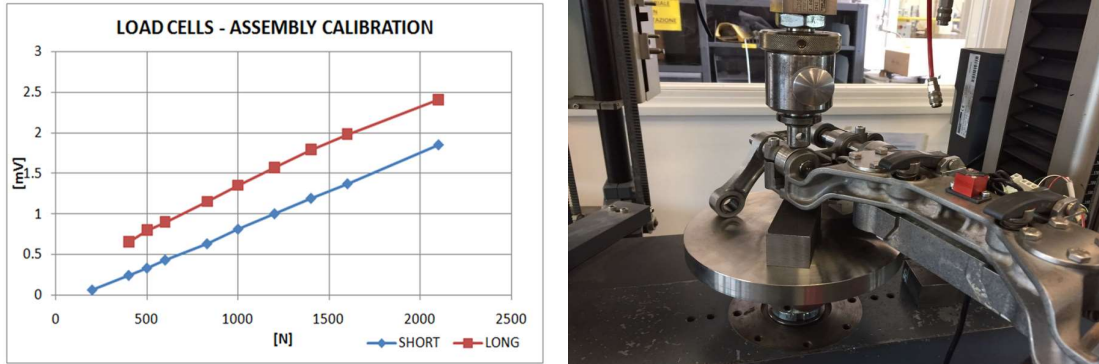


Figure 36: Sensor Calibration curve (left) and equipment (right)

The selection of the data acquisition system was strongly limited by the set up of the trial, since it was required a wireless device that was small enough for being installed on board of the link without interfering with any of the other mechanisms, cams and elements of the frame.

The identified logger was the BeanDevice® DAQ and because of its compact size (58x47x31 mm) it was installed on the forming box of the mechanism A (Figure 36 – left), the power supply was installed on the following *Transversal Link* of the *Chain*, since there was not more available space on the same element. The data were buffered in the BeanDevice® DAQ and transmitted to the with BeanGateway® for the download and the processing. Due to the reduced dimensions of the acquisition system only four channels are available for the input signals, working at the maximum sampling rate of 2 kHz.

An inductive sensor was installed on the transversal link (Figure 37 – right) that was able to detect the passage in front of a bracket fixed on the frame (Figure 38) in order to obtain an accurate correlation of the measurements with the position of the *Chain* during the loading cycle.

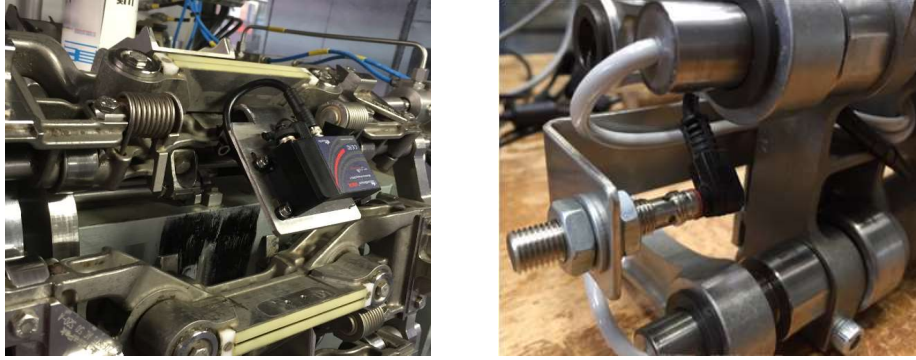


Figure 37: onboard installation of DAQ (left) and inductive sensor (right)

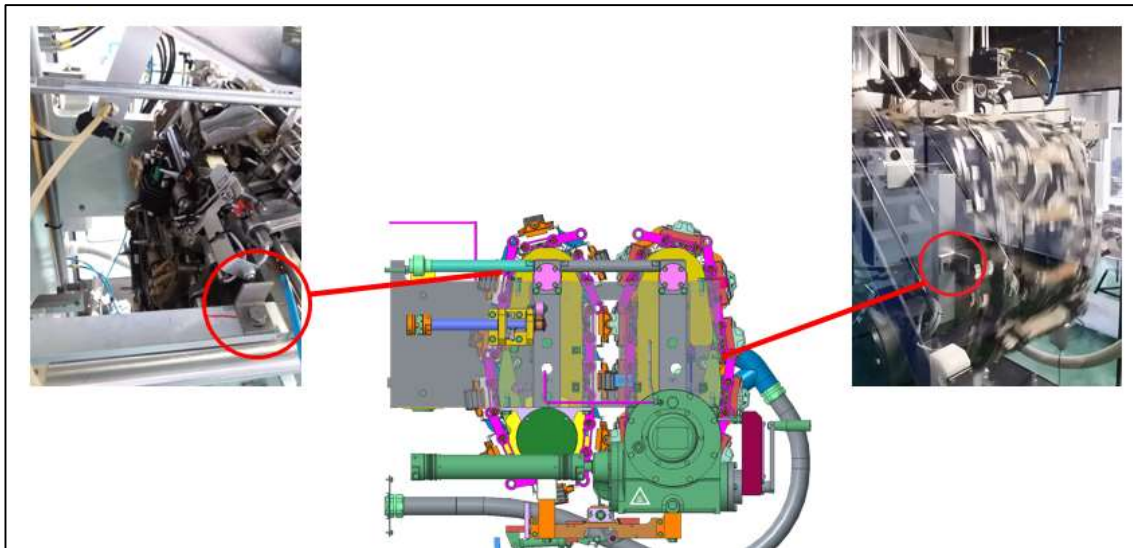


Figure 38: Position of bracket references for the inductive sensor

4.3 Results

The results provided by the virtual model that are presented in this work focused on the load that was applied on the four ball bearings of the *Transversal Link* during the interaction with the *Main Cams* and the paired *Transversal Link*.

The graphic in the Figure 39 shows the calculated reaction force that is applied on the ball bearing during a complete production cycle. Correlating the data with the position of the *Transversal Link*, the phases of the production process that link is subjected to can be clearly identified.

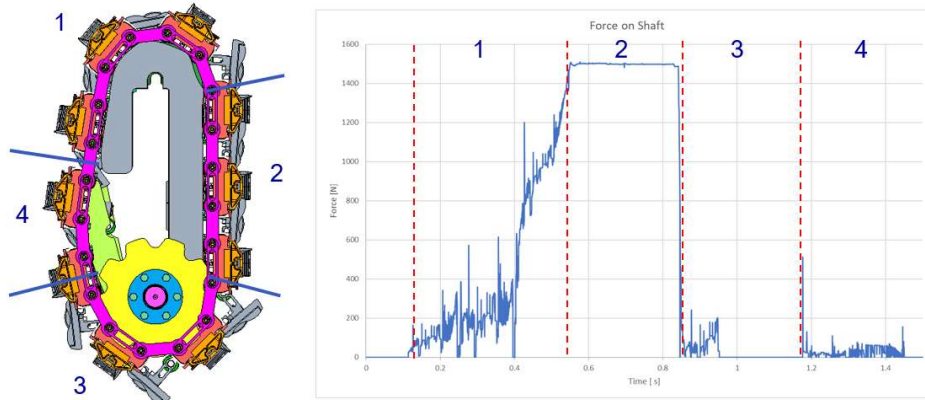


Figure 39: Simulated loading cycle on the ball bearing

The *Transversal Link* analysed was the one that at the beginning of the simulation was located in the external branch of the chain, in the section where the contact with the cam starts. The magnitude of the load is very low since the *Transversal Link* is almost parallel to the cam along the vertical direction and only a minor component resultant of the weight and the tension was balanced by the cam. The following growing trend till the highest plateau is related to the weight of the entire chain, that was hanged up to the cams, whilst the highest values refer to the contact with the paired *Transversal Link* of the other *Chain*, which are compressed in order to clamp and pull the paper tube.

The sudden drop of the force describes the release of the contact between the paired *Transversal Link* and the end of the forming phase of the package, some fluctuations are generated in the last part of the *Cam* and the passage to the *Driving Wheel*, where the ball bearing are not loaded anymore.

The last peak of the graphic represents the passage between the *Tensioner* and the *Cam*, where the bouncing effect of the *Tensioner* induces a speed component that is not tangential to the profile of the *Cam* at the beginning of the contact section.

The plot in the Figure 40 represents the values of the tangential speed of the ball bearing, it shows a repeatable and periodical trend that reflects the pitch of the chain and the driving wheel, exalting the polygonal effect caused by the mechanism. The peak value visible at about 0.4s is a combined effect of the kinematic of the *Chain* and of the profile of the four *Cams*, which adopting different profiles in the top curve determine an additional rotation of the *Transversal Link* around its longitudinal axis.

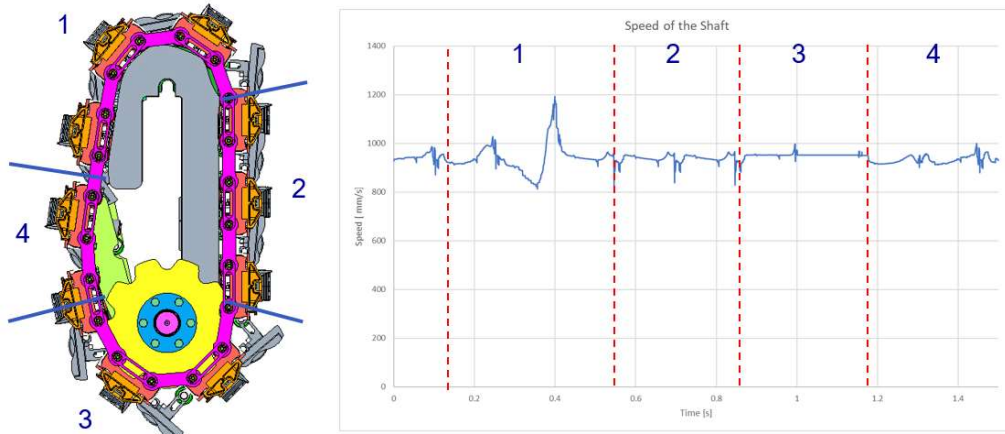


Figure 40: Simulated linear speed of the ball bearing

The curves in the Figure 41 compare the dataset sampled at 1kHz and 2 kHz. The difference did not appear substantial; hence it was possible to set 1kHz as sampling frequency of each channel and to measure the load applied on the both on the long and short shafts at the same time.

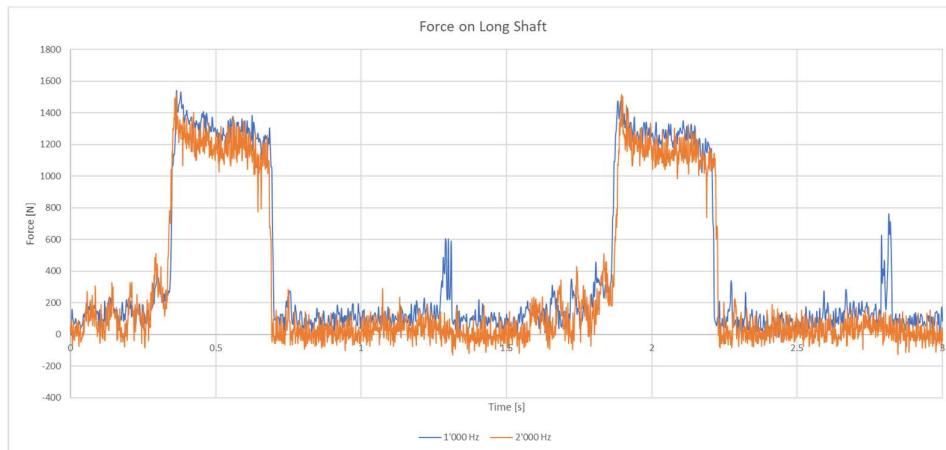


Figure 41: Measured load sampled at 1'000 Hz and 2'000Hz

The data collected during the measuring campaign highlighted a good matching with the calculated values and some deviations, that were assumed to be influenced by the peculiarities of the physical equipment used for the measurements. Even if the nominal range, the tolerance of the components, the wear out of the part, misalignments and assembling deviations can affect the magnitude as well as the loading path of the ball bearings.



Figure 42: Overlapped curves of calculated and measured load

The data collected by rotating the shafts of 90° confirmed the absence of either punctual excitation or loading path that were stressing the transversal link along the direction of the displacement, according with the simulation results.

4.4 Cutting Force

The data about the force reached during the cutting process is a relevant information required both as input for the dynamic model described in the Chapter 3 and for the investigation of the lifetime performances reached by the *Knife*.

The most suitable component to be redesigned for this measurement was the shaft of the *Cutting Bearing*: since it is installed on the frame, the usage of a wired sensor was possible, ensuring higher sampling frequency and adopting bench dataloggers, which was crucial since the duration of the cutting process is in the range of $[0.010, 0.020]$ ms.

The sampling frequency defined for the trial was 20 kHz.

The stresses applied on the shaft of the *Cutting Bearing* were expected to be with a variable direction: an impact when starting the contact between the *Cutting Cam* and the bearing (green direction – Figure 43), a lower and growing load caused by the compression of the spring installed on the shaft and the friction between the *Knife* and the *Cutting Rail* and then an higher impulse caused by the impact against the packaging material, the penetration of the blade and the separation of the layers.

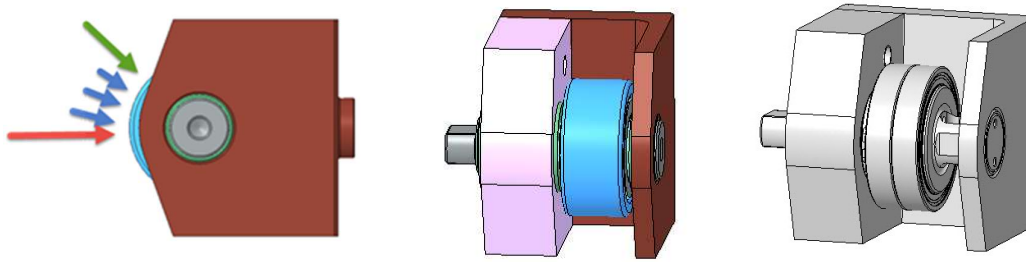


Figure 43: Loading Direction (left), Standard (middle) and Modified (right) Supports

Due to the supposed evolution of the cutting force, a sensor with two independent measurement direction was required, in order to combine analytically the measurements afterwards. The new design of the shaft should ensure both a higher sensitivity to the shear stresses in two defined cross-sections and the mechanical resistance in both installation positions (0° - red arrow of the Figure 43- and 90° in reference to the cutting direction).

The sensitive cross-section should be placed between the region covered by the internal race of the ball bearing and seats of the shaft into the supports, hence the support was redesigned as well in order to create the minimum axial space for installing the strain gauges.

The sensor was axially constrained into the support by means of three screws, which also guaranteed the correct orientation during the trials.

The material selected for the sensor was AISI 630 and its design was optimized by the support of FEA analysis.

The Figure 44 shows the stress and strain results obtained during a static simulation executed on the modified geometry of the sensor. The body was constrained as in the installation configuration, blocking the displacements and the rotations of the coupled surfaces and applying the theoretical maximum cutting load of 1'500N along the horizontal direction (red arrow of the Figure 43 – left)

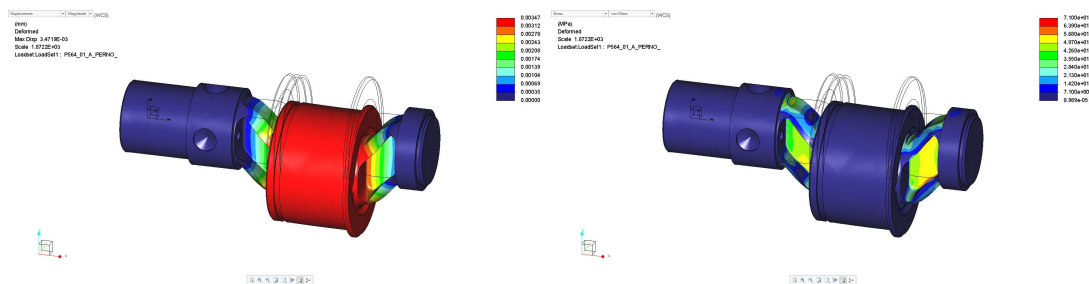


Figure 44: Stress (MPa) and Deformation (mm) Fields of the Sensor

The calculation showed that the obtained geometry was robust enough to withstand to the cutting load and the consequent deformation sufficient for obtaining accurate measurements. In order to achieve the highest accuracy of the sensor, the calibration was performed in the final assembled configuration: during this phase it was noticed a marginal influence of the tightening torque applied on the screw, thus it was indispensable to add the requirement about the tightening torque and the sequence of the screws.

Two sensors were manufactured in order to sample both shafts in the same time and obtain the total value of the cutting force.

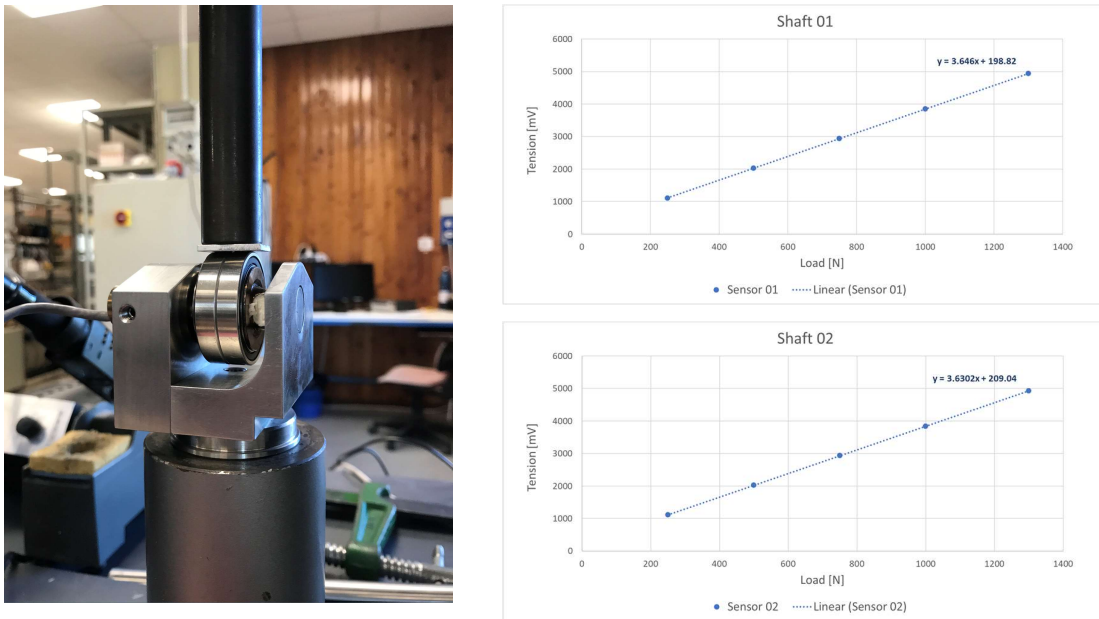


Figure 45: Sensor Calibration Set-Up and Curves

The data collection was arranged in two steps, targeting the two assembling configurations (0° and 90°) and during each phases several testes were executed, in order to highlight the different elements combined during the cutting event, according with the possible operative conditions of the *Filling Machine*.

The sequence of the trial was:

- Manual displacement of the Chain without packaging material
 - The purpose of the trial was to identify peculiarities of the *Jaw System* and associated them to the correct *Transversal Link*
- Slow Rotation at 4'000 pack/h without packaging material
 - The purpose of the trial is to investigate the response of the *Jaw System* during the steady rotation of the Chains
- Production at 20'000 pack/h with packaging material

The purpose of the trial is to analyse the stresses produced during the cutting event, due to the presence of the packaging material and the product. The production rate adopted during this test is one of the nominal operative condition of the *Filling Machine*, but not the most common.

- Production at 24'000 pack/h with packaging material

The purpose of the test is to investigate the response of the system operating at the full nominal capacity and highlighting the inertial contribution to the loading history of the *Cutting Bearing*.

4.5 Cutting Direction (0°)

The test executed with the manual movement of the *Jaw System* was indispensable for identifying the correct response of each *Transversal Link*. The graphic in the Figure 46 captures the loading curve of the springs, which appears to be repeatable among the different elements of the *Chain*, but in some links: *Link#1*, *Link#2*, *Link#3*, *Link#8* a significant peak is reached before the cutting stroke was completed, position corresponding to the maximum compression of the spring.

This specific behaviour might be generated by several possible causes, such as a misalignment between the *Sealing* and *Pressure Chains*, that is not recovered by the rubber bushing installed in the *Cutting Rail*; an increased backlash of the coupling between the shaft and the *Knife*, causing the stack of the blade; the increased backlash between the bushings and the shaft, causing the stack of the shaft.

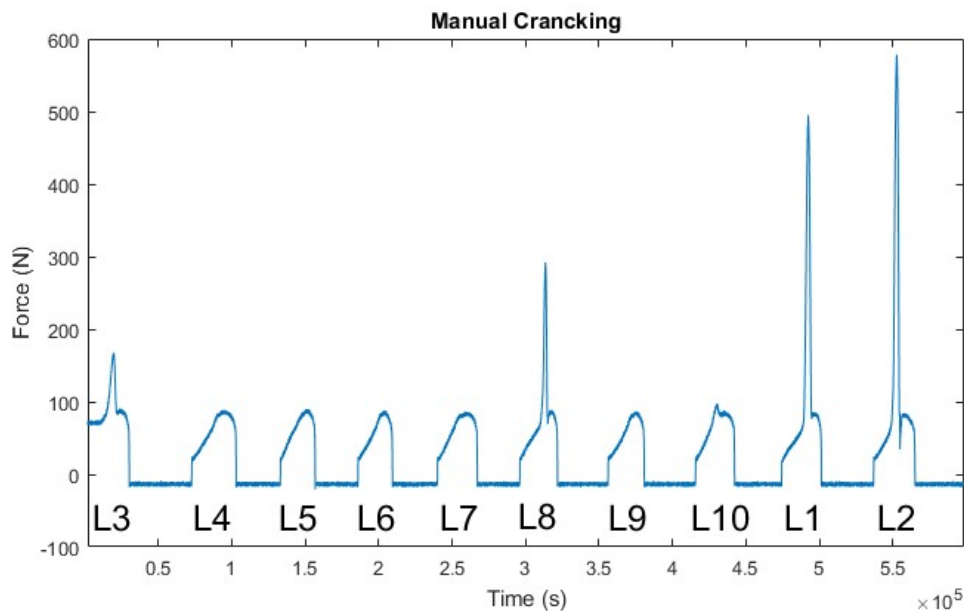


Figure 46: Force Acquisition - Manual Cranking

The trial at slow speed (4'000 pack/h) without the packaging material (Slow Inching), confirmed the trends detected in the previous step, highlighting that the presence of the peaks is repeatable and it is affected by the rotation speed of the *Jaw System* (Figure 47).

The signals provided by the two load cells are completely overlapped, in the region corresponding to the compression of the springs, whilst there is a gap of about 100 N in the unexpected peaks of the *Link#2*.

The repeatability of the unexpected peaks in the highlighted *Links* and their presence in both sensors, suggested that the issue would be related to something happening on the *Knife*, hence the misalignment of the *Cutting Rail* and the stack of the *Knife* was the most probable explanation.

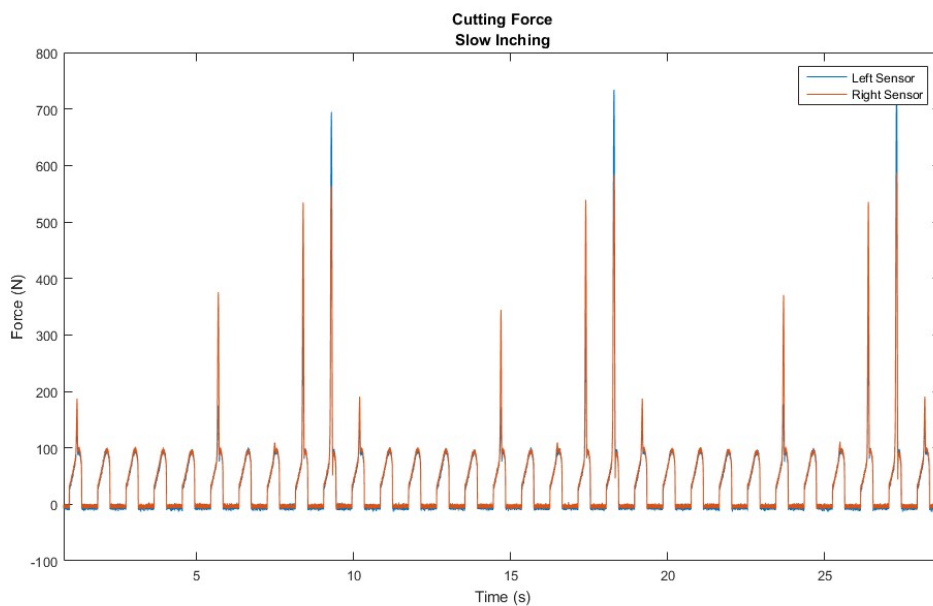


Figure 47: Force Acquisition - 4'000 pack/h

The graphic in Figure 48 provided an enlarged plot of the *Links* #10,#1,#2:

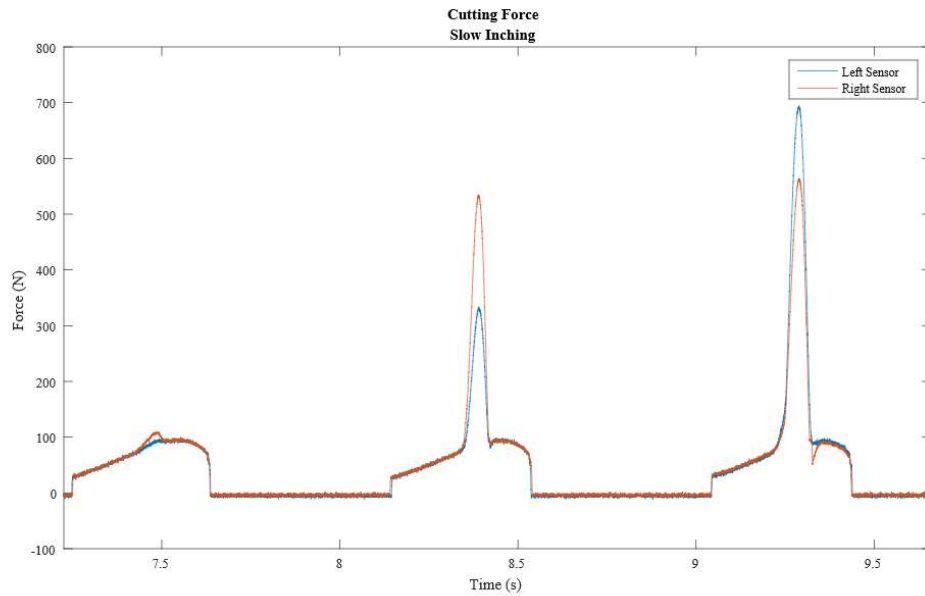


Figure 48: Force Acquisition - 4'000 pack/h – Single Cut detail

The test executed at the nominal production rate of 24'000 with the packaging material provided information about the magnitude of the cutting force in a standard cycle, the trend of the data showed that the peaks identified during the trial without the packages were still clearly visible and their intensity was even higher than the force required for separating the layers of the packaging material.

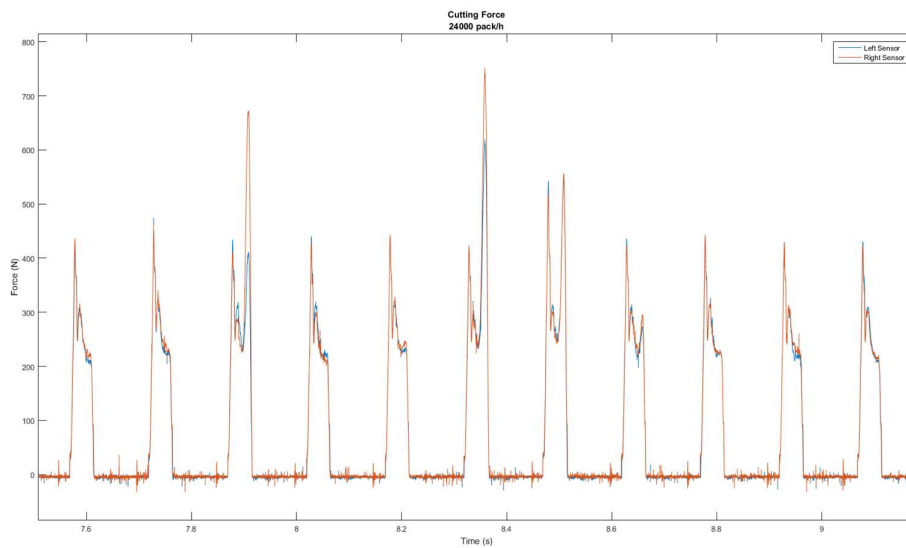


Figure 49: Force Acquisition - 24'000 pack/h

The graphic in the Figure 50 represents the magnification of one cutting cycle of the *Link#5*, which is not affected by any unexpected effect. The profile of the force shows a first growing

step, corresponding to the contact between the *Cutting Cam* and the *Cutting Bearing* and the initial compression of the spring. The section with the high growing rate of the force corresponds to the forward stroke of the *Knife*, that encounters the packaging material and deforms it into the cavity of the *Inductor*. The peak force represents the maximum resistance opposed by the packaging material before the penetration of the tip of the *Knife* teeth, the force then drops during the laceration of the packaging material. The knee after the peak force, represents the contact against the valleys of the teeth, where happens the complete separation of the packaging material above and below the *Knife*. The next phase is characterized by the decreasing value of the force, since the friction between the packaging material and the *Knife* is the only reaction the is opposing to its displacement. The last section, where the force increases again, is caused by the compression of the upper and lower edged of packaging material between the *Knife* and the cavity of the *Inductor*, since the clearance between the two components is smaller than the packaging material width.

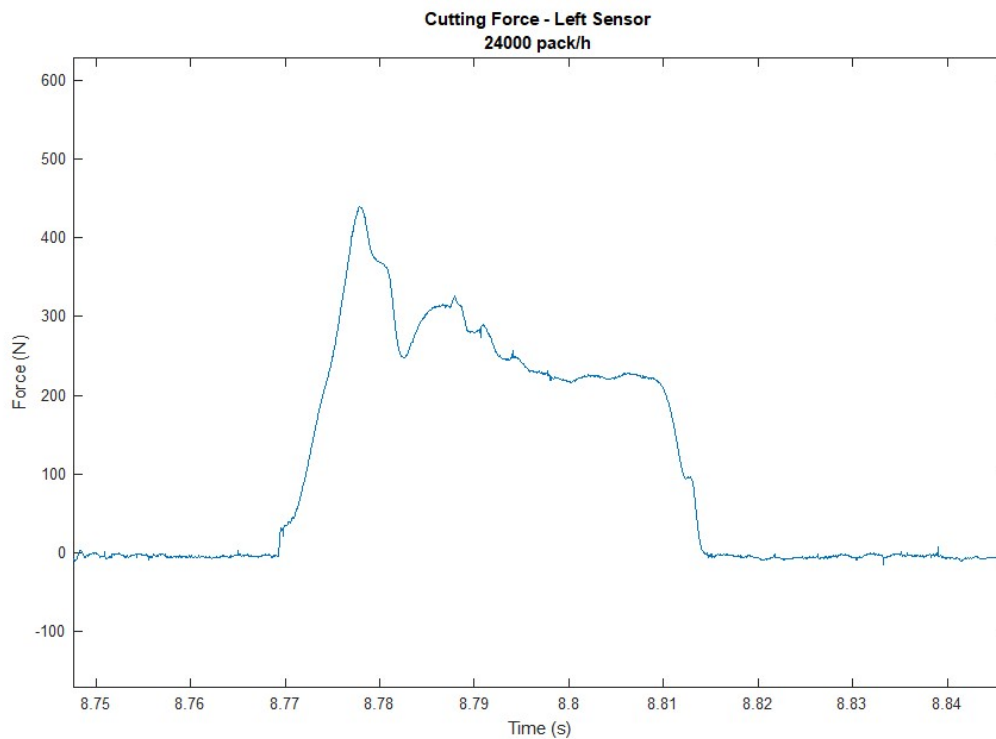


Figure 50: Force Acquisition 24'000 pack/h - Single Cut Detail

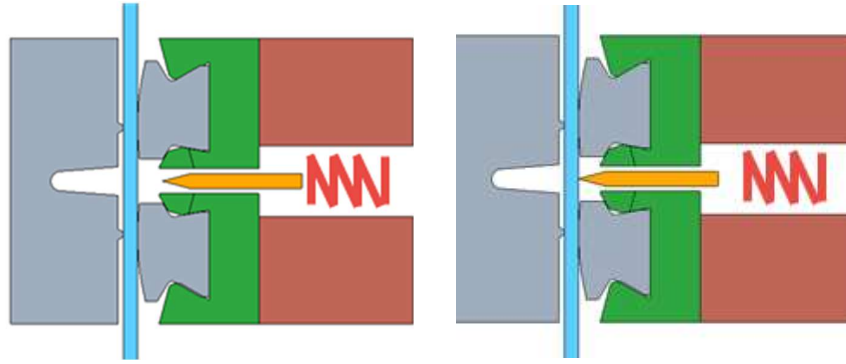


Figure 51: Cutting Phases: Starting (left) & Approaching (right)

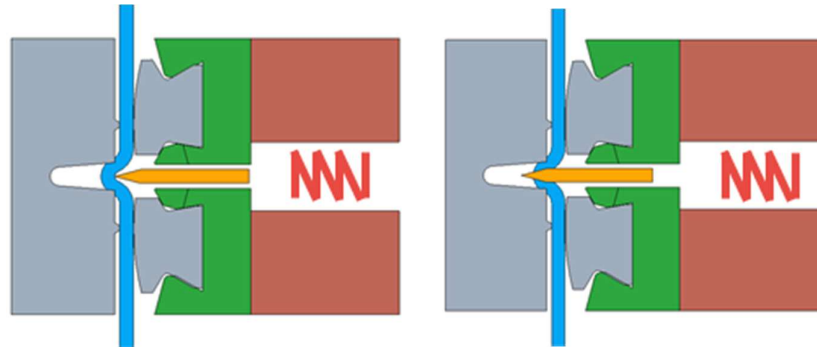


Figure 52: Cutting Phases: Packaging Material Deformation (left) & Separation (right)

The comparison of the curves obtained at the different production rates of 20'000 and 24'000 pack/h, did not highlight relevant differences of the peaks measured, this would be related to a contained difference between the linear speeds of the *Transversal Links*, which passes from 0.96 m/s to 1.16 m/s. The variation of the cycle duration and a slight variation of the slope of the cutting profile can be noticed.

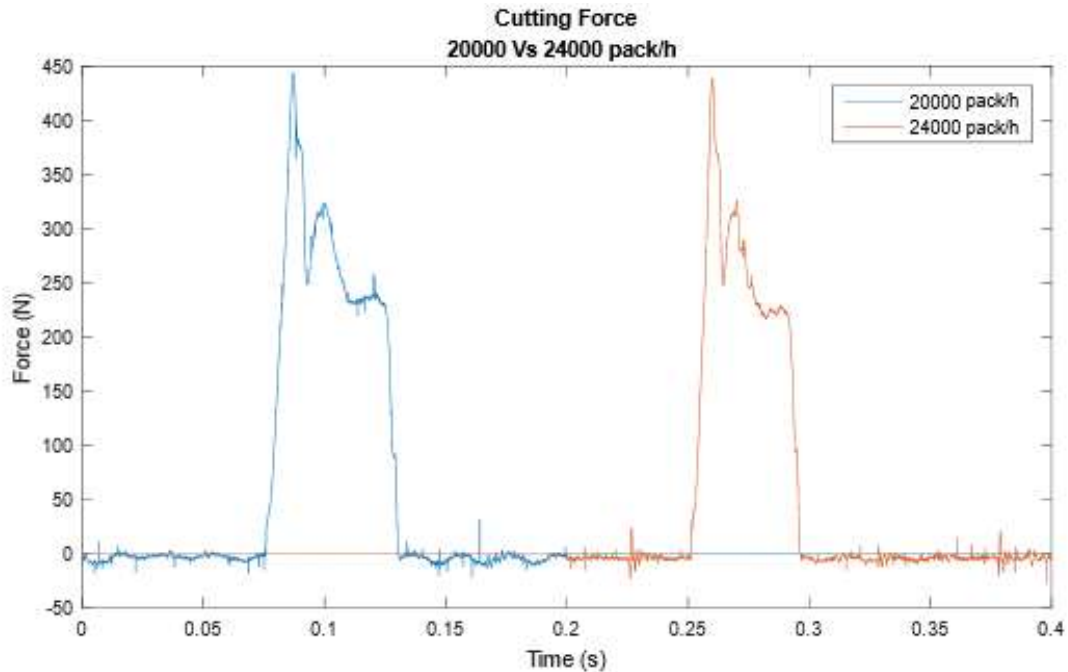


Figure 53: Cutting Force Comparison: 20'000 and 24'000 pack/h

The measurements were executed sampling 100 cutting cycles and repeating the sequence three times, in order to verify the repeatability of the results.

The plots shown in the Figures 54 and 55 represent the distribution of the peak forces captured from each *Transversal Link*, filtering out the unexpected effects detected in some of the *Transversal Links*.

The datasets appeared repeatable within the different trials, the behaviour of the Left and Right sensors was comparable, and the cutting force captured in the different *Transversal Links* was coherent and normally distributed. An exception was represented by the *Transversal Link #2*, that showed an higher force, in reference to the average one measured on the other *Links*, the deviation would be justified by the same causes highlighted during the analysis of the trial at low speed; the reason why those effects are visible only in this case might be related to the magnitude of the deviation occurring in this position (highest unexpected peak), that likely has not impact in the cutting forces of the *Links #1* and *#10*.

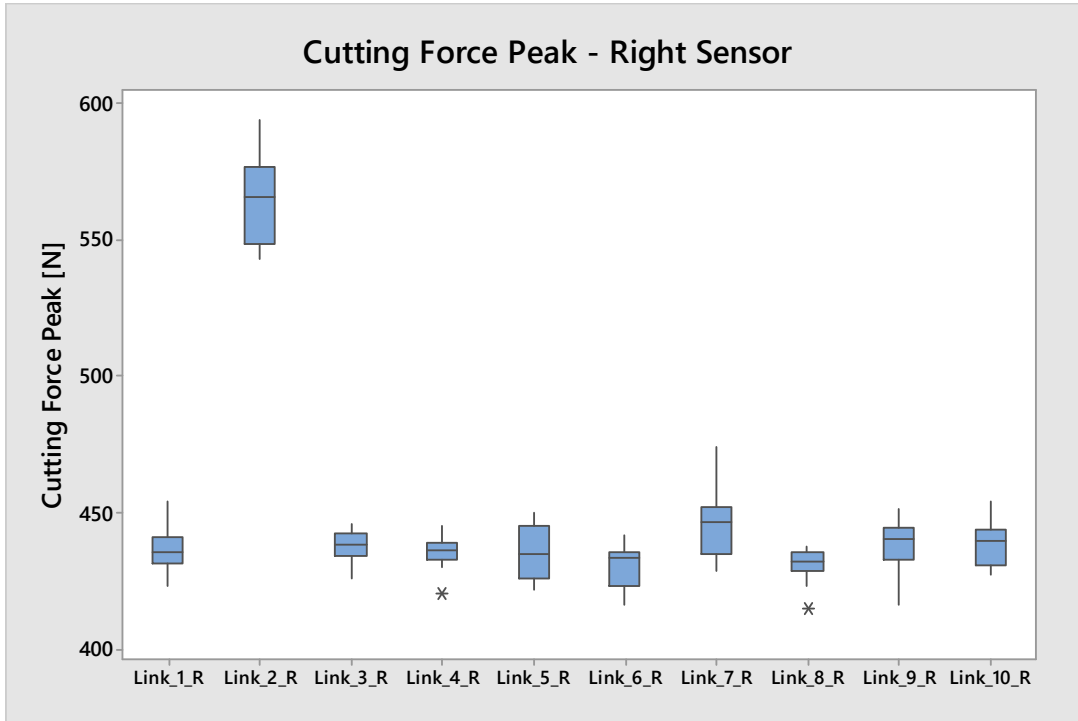


Figure 54: Cutting Force Peak distribution – Right Sensor

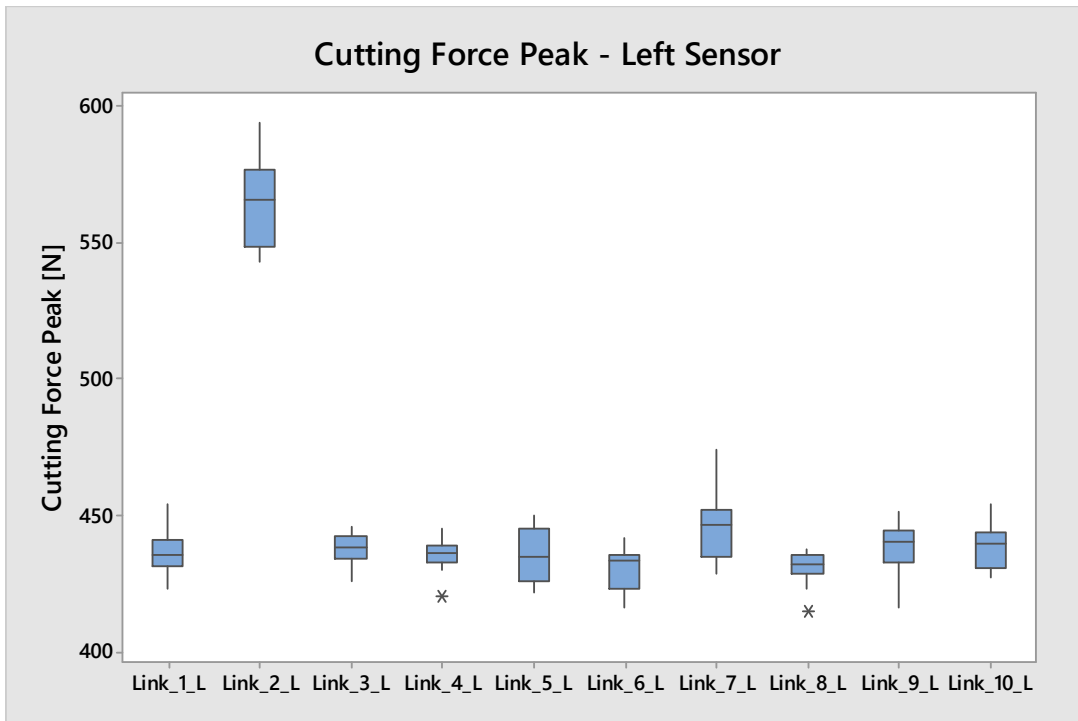


Figure 55: Cutting Force Peak distribution – Left Sensor

Transversal Link direction (90°)

The installation configuration of the sensors in these trials was oriented with the measuring direction long the vertical one, corresponding to the speed direction of the speed of the *Transversal Link*.

The test executed by manually rotating the *Chains* (Figure 56) highlighted that the unexpected peaks detected in the former test can be noticed also in along this direction, and the reason is related to the position of the contact point between the *Cutting Cam* and the *Cutting Bearing* (Figure 57).

The graphic shows also a negative force at the end of the cutting cycle, that describes a load oriented from the bottom to the top, it describes the initial phase of the return stroke of the *Cutting Cam*, that is driven by the reaction force of the spring.

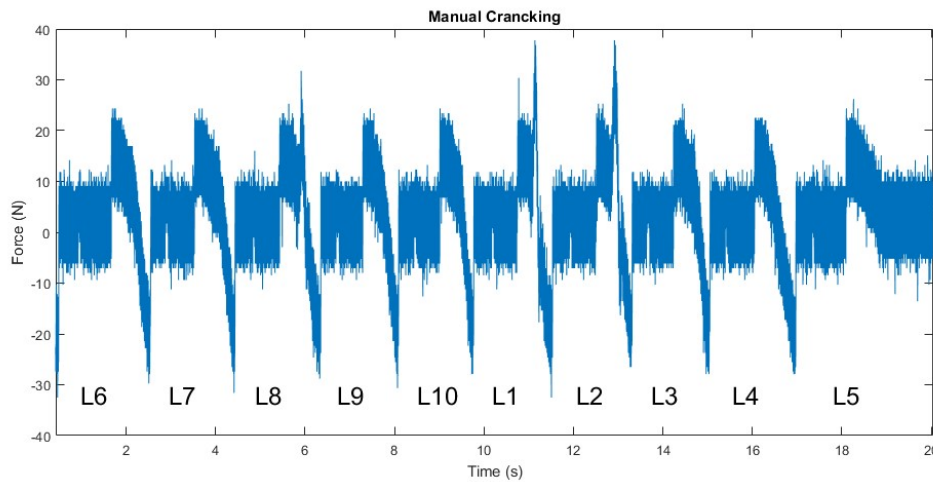


Figure 56: Cutting Force Acquisition - Manual Cranking

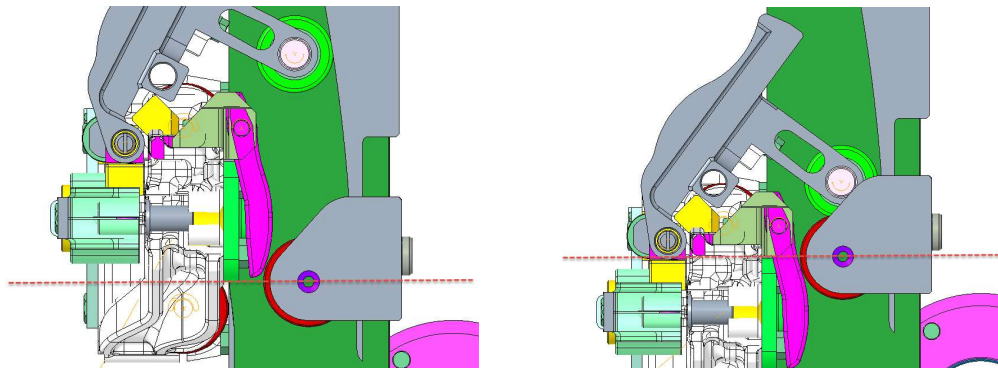


Figure 57: Cutting Cam reference positions

The trial executed at production rate of 4'000 pack/h confirmed the results achieved with the manual movement of the *Chains*, showed that the response of the sensors was comparable also in this configuration and did not highlight relevant differences neither in the peak forces not in

the minimum once, since the translational speed of the *Transversal Link* was not significantly different. The graphic in the Figure 64 is a magnification of the cutting forces measured for the *Transversal Links #1* and #2.

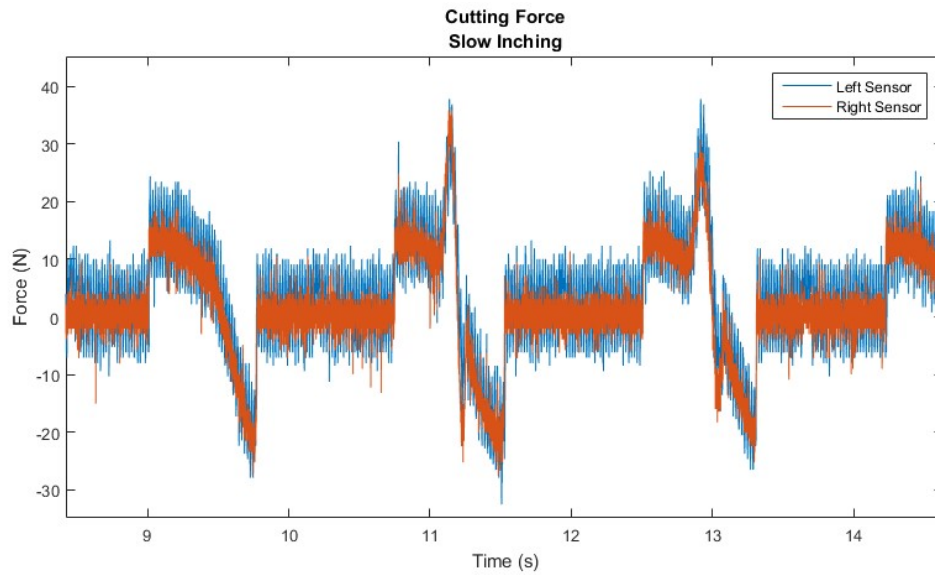


Figure 58: Cutting Force Acquisition - 4'000 pack/h

The trends sampled during the test executed at the production rate of 24'000 pack/h (Figure 59) showed a relevant difference in the peak forces, which were related to the energy of the impact between the *Cutting Cam* and the *Cutting Bearing* and the effect of the unexpected peaks noticed during the manual movement were hidden into the contribute of the impact.

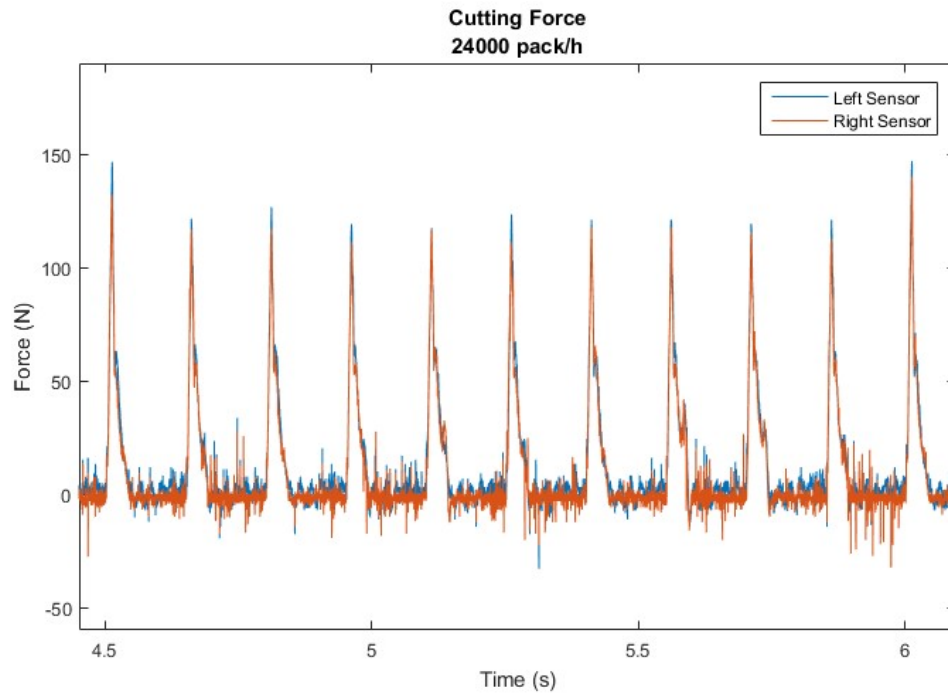


Figure 59: Cutting Force Acquisition - 24'000 pack/h

The negative forces measured during the return stroke of the *Cutting Cam* did not change significantly their magnitude, which is mainly related to the potential energy stored in the compressed configuration of the spring, but randomly appeared on the different *Transversal Links*, since at the nominal production speed the *Chain* moves faster than the backward stroke of the *Cutting Cam*.

As in the data sets acquired in the horizontal configuration (0°), there was not a significant variation of the forces measured at the two nominal production rates of 20'000 and 24'000 pack/h (Figure 60), due to the small difference of the linear speed of the *Transversal Link*; the difference is instead significant between the low speed test at 4'000 pack/h and the one at full production speed.

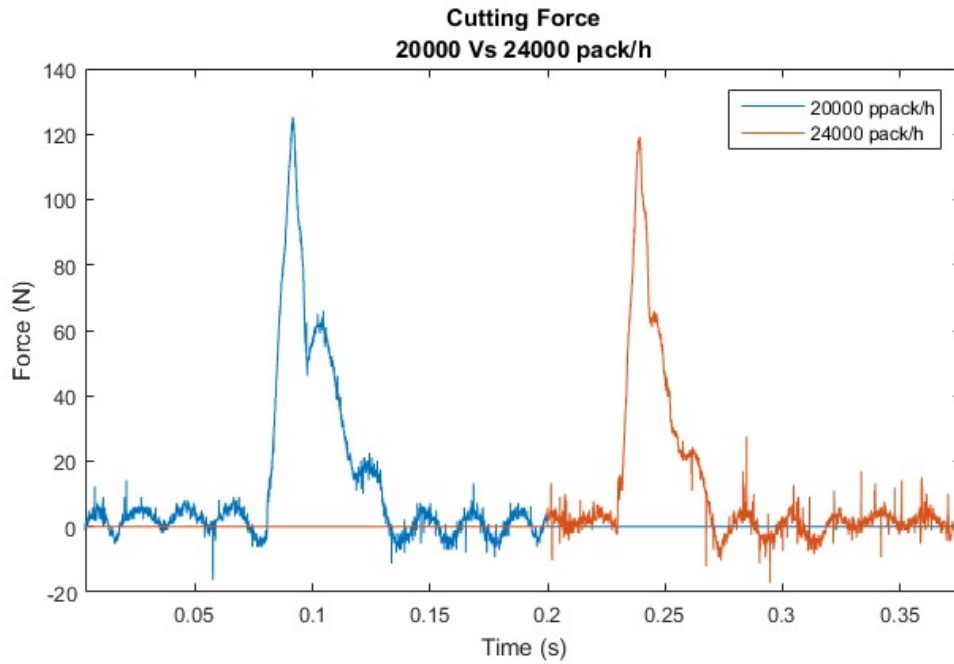


Figure 60: Cutting Force Acquisition - 20'000 VS 24'000 pack/h

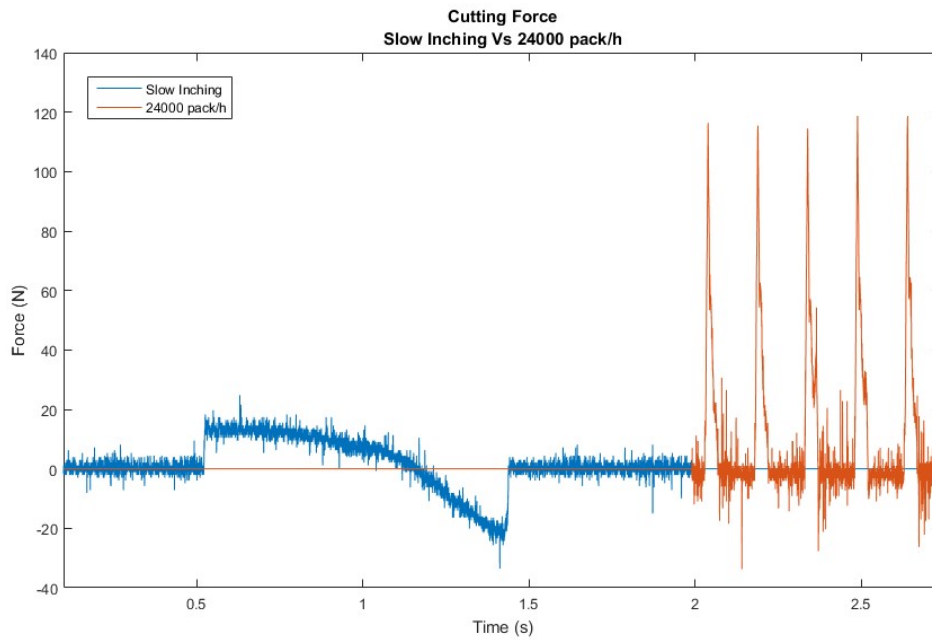


Figure 61 Cutting Force Acquisition - Manual Crancking VS 24'000 pack/h

In order to verify the repeatability of the measurements, the tests were repeated three times, sampling 100 cutting cycles, the graphics in the Figures 62 and 63 shows the distribution of the peak forces detected:

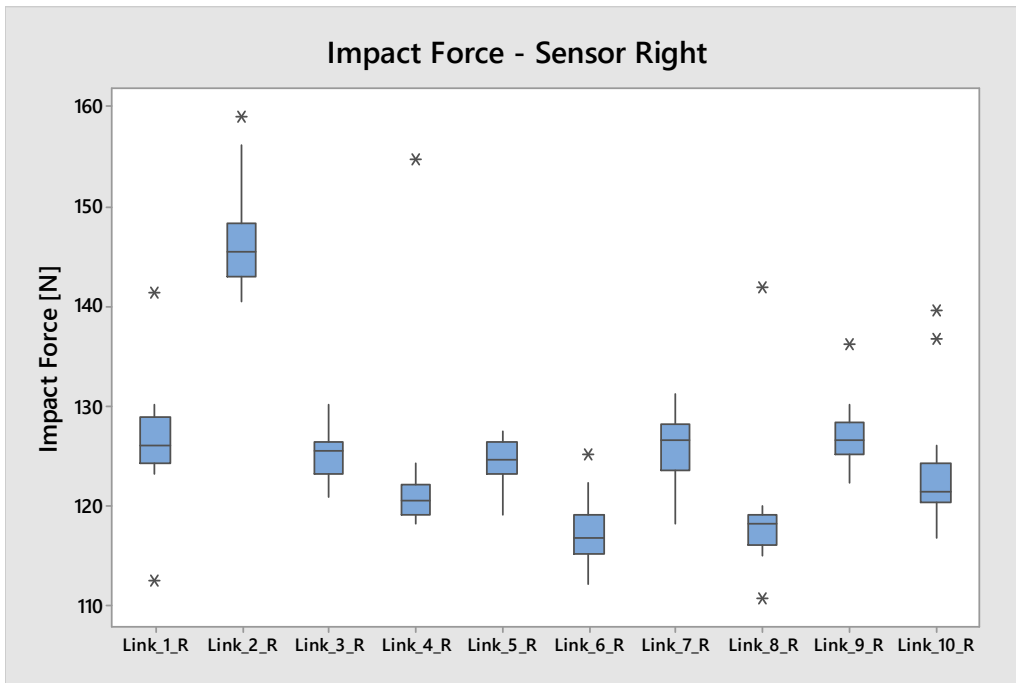


Figure 62: Impact Force Distribution – Right Sensor

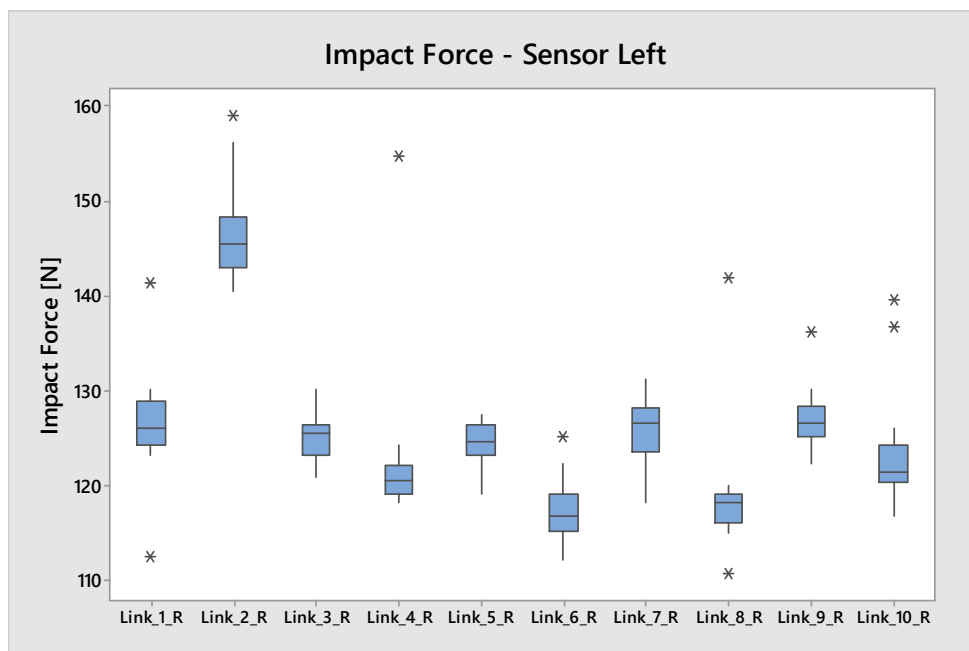


Figure 63: Impact Force Distribution – Left Sensor

The results are repeatable and with a contained variation within the data referred to the same *Transversal Link*, whilst showed a higher fluctuation among them, which might be related to the specific status of the *Transversal Link*, such as wear level, manufacturing tolerances and assembling clearances.

The Figure 64 shows the cutting curves measured for the *Link #8* during the trials at the full production rate and the magnitude of the resulting force.

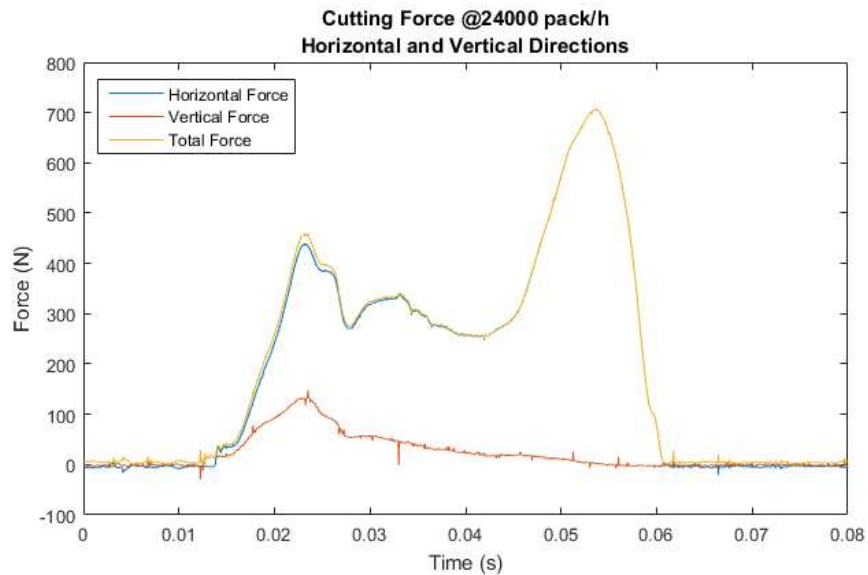


Figure 64: Cutting Force: Horizontal and Vertical curves

4.6 Volume Box and Folding Flap load

The two main interactions between the components of the *Transversal Link* and the package during the forming process that would be investigated are related to the load applied on the *Volume Box* and the one on acting on the *Folding Flap* shaft.

The measurement of this forces requires a wireless sensor, which should be installed on the *Transversal Link* for the entire production cycle.

Even in this case, the sensors are a customized product, which was obtained by adapting the design of the standards components, for creating sensitive sections to be instrumented with strain gauges.

The dynamic analysis of the motion of the *Volume Box* highlighted that in nominal conditions the main direction of the applied forces is normal to the panel acting on the package, hence the sensor was obtained by modifying the geometry of the *Fork* that sustains the shaft carrying the roller.

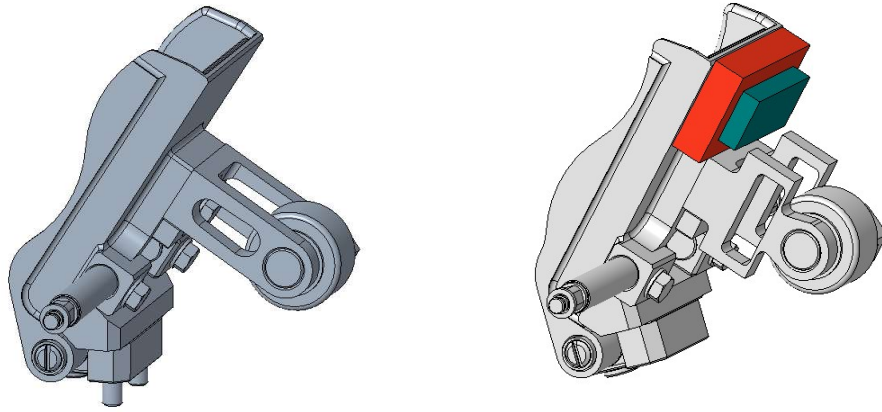


Figure 65: Reference and sensorized Volume Box

The sensors were manufactured in AISI 630 and their geometry was optimized by means of FEA.

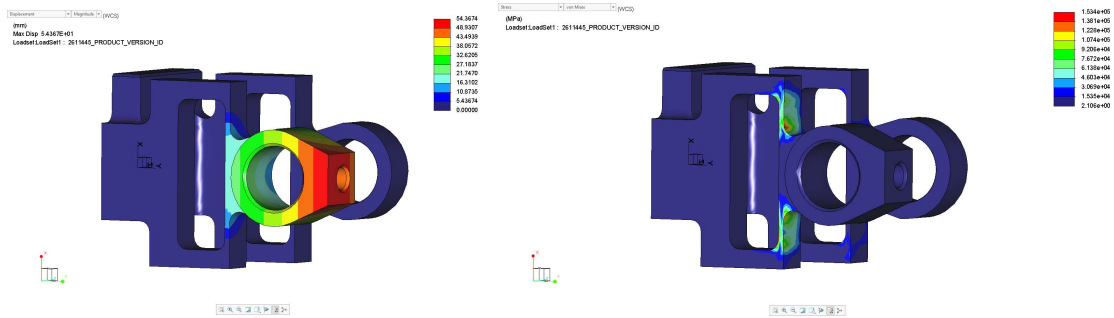


Figure 66: Stress (MPa) and Deformation (mm) Fields of the Sensor

The Figure 66 shows the Stress (MPa) and Strain (mm) calculated on the modified geometry of the sensors, when loaded with the maximum force calculated in dynamic simulation, applied along the normal direction of the *Volume Box* forming panel and considering the *Volume Box* displacement constrained as in the forming phase. The purpose of the calculation was to confirm that the obtained geometry would resist to the operating load and to ensure a deformation that would be detectable by the strain gauges.

The red and green bodies drafted in the customized configuration in Figure 65 represent the amplifier and the power supply of the sensor, that would ensure the wireless transmission of the data. The weight of those elements was less than 50g, hence it was considered a negligible contribution to the dynamic of the operating system.

As for the measurements executed on the shafts of the ball bearing, the maximum sampling frequency allowed is 2'000Hz.

An analogous concept was used for the development of the sensor that should measure the load applied on the *Folding Flap*, but in this case the sensors was sensitive to the torque applied at its extremity by the package.

The design of the shaft was changed by the implementation of a shaped eyelet on the body of the shaft (Figure 67), which would maximise de deformation produce by the torque being insensitive to the any interaction with the installation interfaces.

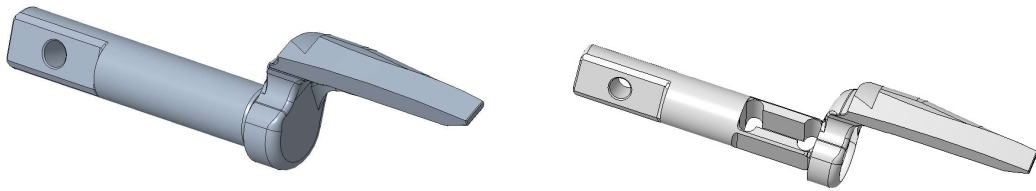


Figure 67: Reference and sensorized Folding Flap

The material of the sensor was AISI 630 and the electrical connection with the amplifier and the power supply was obtained with a wire coming out from the front of the shaft.

The Figure 68 shows the Stress (MPa) and Deformation (mm) fields calculated for the sensors in the theoretical operative conditions. The reference configuration was the forming process, hence the rotation of the shaft in the connecting section with the lever (see Figures 15 and 22) and its displacements were constrained, and the load was considered localized on the Flap surface in contact with the package. As for the other sensors, the modified geometry of the sensor ensured resistance to the operative conditions and enough deformation for ensuring an accurate measurement.

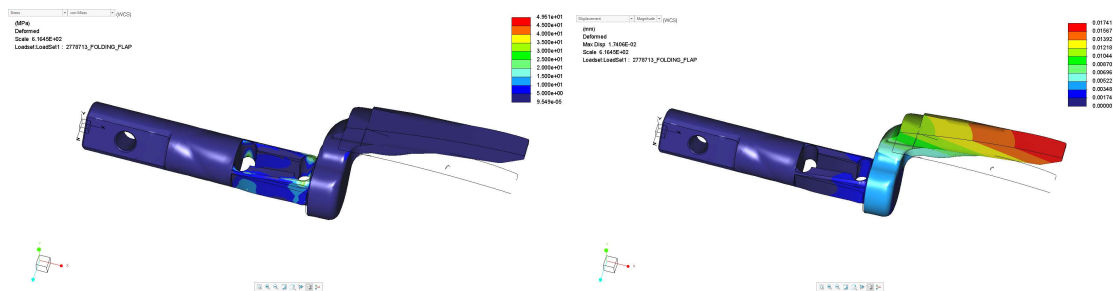


Figure 68: Stress (MPa) and Deformation (mm) Fields of the Sensor

The experimental data from those last two sensors are not available yet due to the forced closure of the plant caused by the pandemic COVID-19.

4.7 Tensioner

The tuning of the coefficients adopted for modelling the contact between the *Tensioner* and the cam follower of the *Transversal Links*, was done cross-checking both the load measured by the shaft previously discussed and verifying its displacement during the working cycle.

The measurement was executed by means a commercial optical sensor, that was installed between the *Tensioner* and *Frame* (Figure 69).

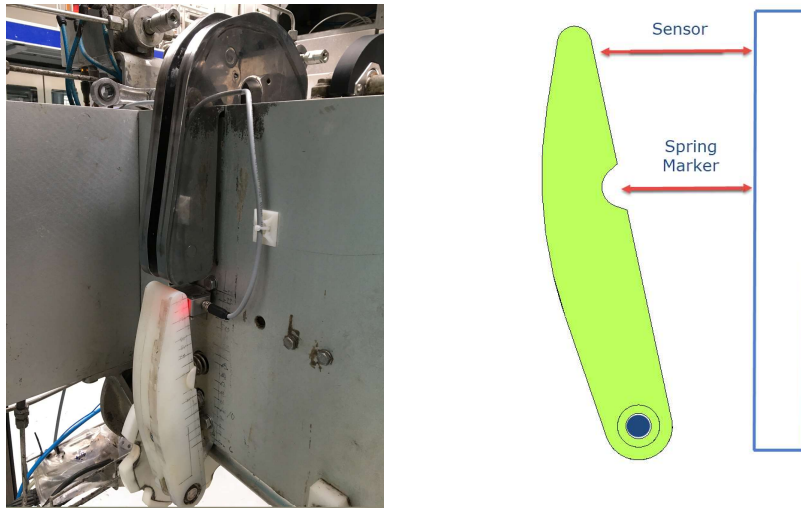


Figure 69: Measurement Set-Up

The data sampled by the sensor showed a fluctuation having the main frequency correlated with the passage of the *Transversal Links*, as shown by the simulations.

The Figures 70 and 71 show the calculated displacement and the measured one, that once recalculated for the distance between the marker and the joint, was perfectly aligned with the calculations.

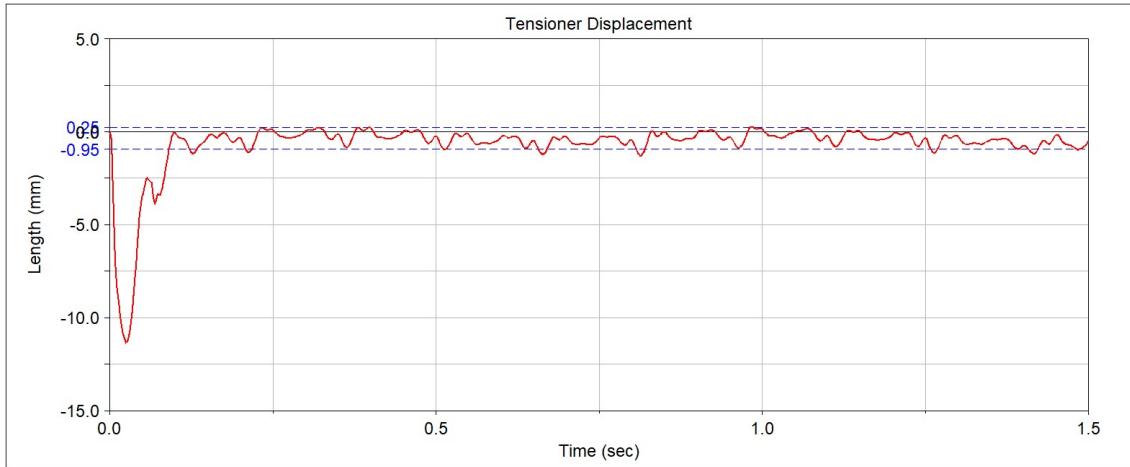


Figure 70: Tensioner computed fluctuation (Marker Position)

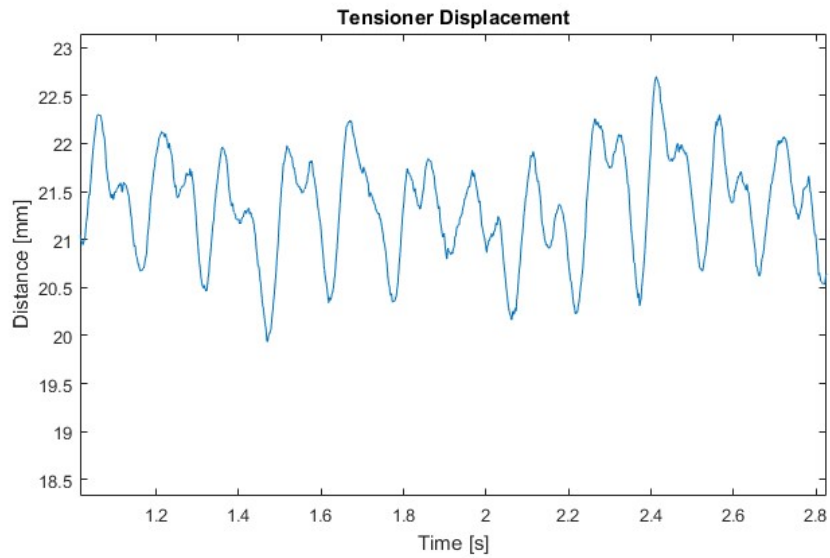


Figure 71: Tensioner measured fluctuation (Sensor Position)

The plot of the FFT (Figure 72) clearly shows that the oscillations of the *Tensioner* are directly correlated to the frequency of the *Transversal Links*.

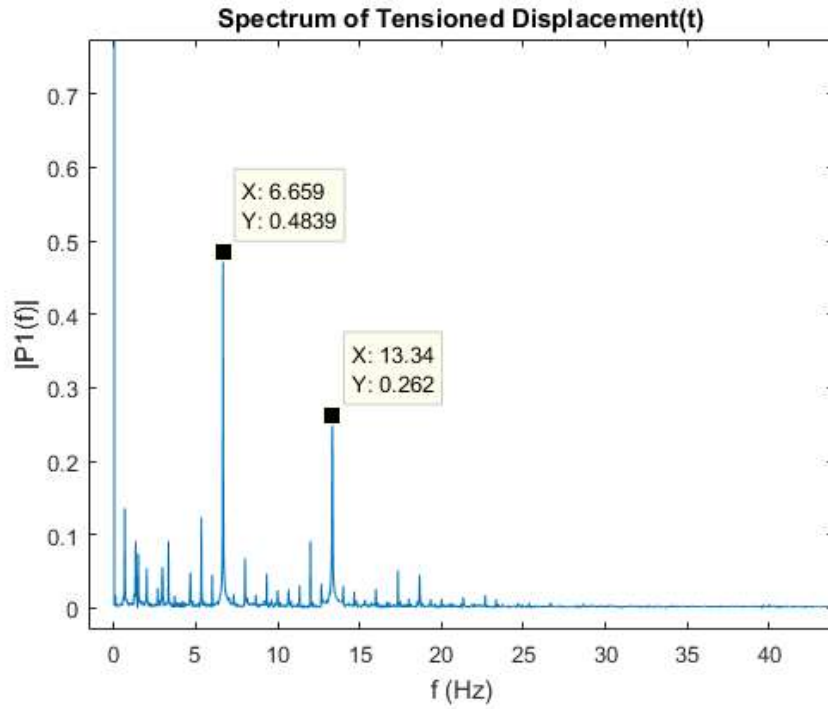


Figure 72: Measurement signal frequencies

5 Operations out of the nominal conditions

The dynamic model was used for investigating the behavior of the *Jaw System* in case of some components would operate out of the nominal working conditions, due to the degradation of the performances of the mechanisms caused by wear, wrong assembly of the components, human errors, lack of maintenance on the equipment.

Three cases have been investigated, since those might be connected to issues detected on the field: the breakage of one of the springs installed on the *Tensioner*, the breakage of one of the springs installed on the *Volume Box*, the ageing of the damper that arrests the displacement of the *Volume Box* and the breakage of the stopping element acting during the opening phase of the *Folding Flap* mechanism.

5.1 Tensioner Spring

This analysis was justified by the occurrence of claims related to cam follower of the *Transversal Links*, hence it would investigate if the status of the *Tensioner* out of the nominal working conditions would generate too high stresses on the cam followers.

The graphic below contains the trend of the contact forces calculated in reference to three operative conditions: the nominal configuration one of the *Jaw System*, the case of breakage of one of the two springs and the case of the absence of the action of both *Tensioners*, which is a limit conditions but it is possible after ordinary maintenance operations on the components of the *Jaw System*, since the *Tensioner* should be locked in a deactivated position in this case.

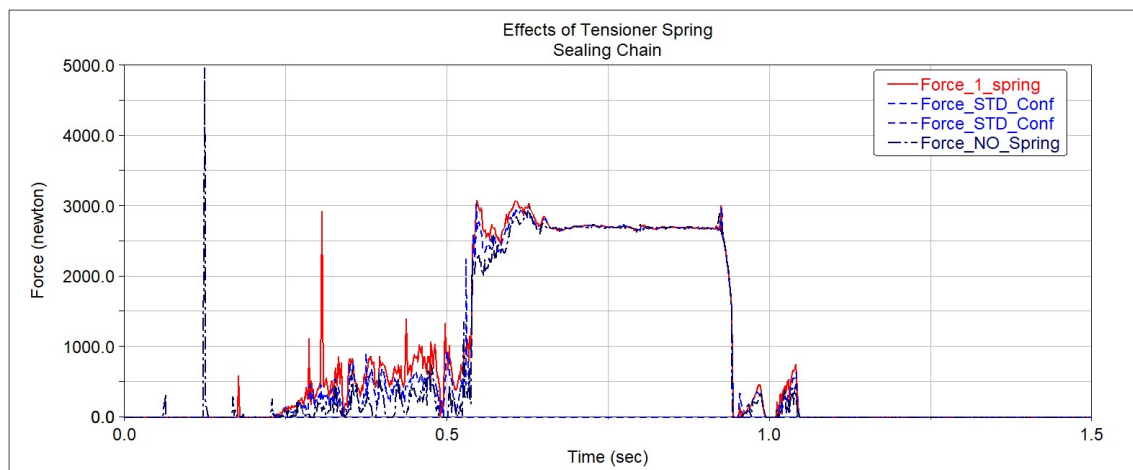


Figure 73: Effects of the Tensioner Spring Preload

The analysis demonstrated that the dynamic behavior of the *Jaw System* is robust respect the action of the springs of the *Tensioner* and in case one of those would be broken, the equipment would be more stressed, but sudden failures would not be expected in the short term period, since no highly intense load are added, but since one additional peak force was detected, this might impact the resistance of the component to fatigue.

The extreme case of the absence of both *Tensioners*, instead, represents a critical operative condition of the *Jaw System*, whose cam follower can easily fail due to the high intensity of the impact with the *Main Cam*.

5.2 Volume Box Spring

The trial relays to the investigation of the robustness of the behavior of the *Volume Box*, which operating without of one of the retaining springs, in order to verify if vibrations and bouncing occurs during the motion of the *Chains*, since those might be critical for the forming of the package.

The data reported in Figure 74 shows that the absence one of the springs is not critical for the functioning of the system, since any bouncing effect was detected along the trajectory. The maximum value of the force calculated is obviously lower in absence of one spring.

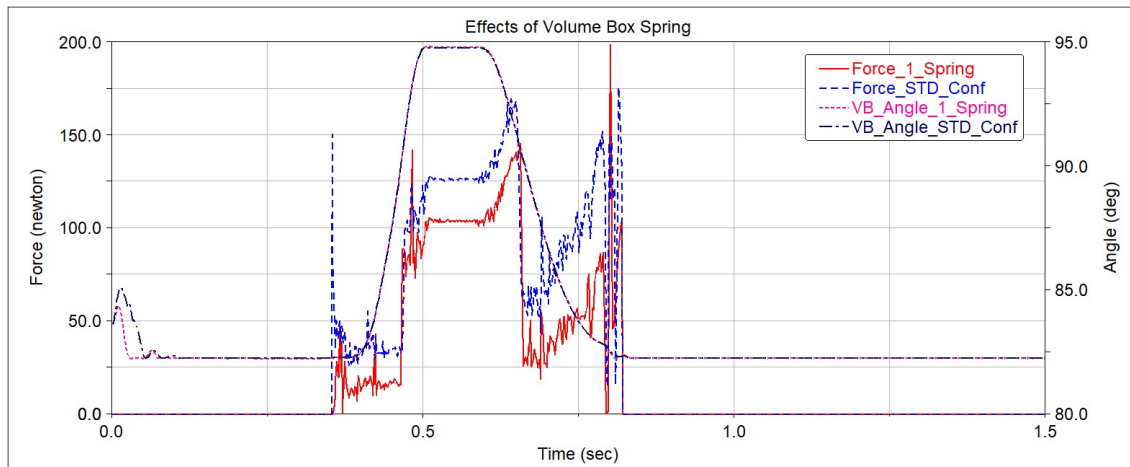


Figure 74: Effects of the Volume Box Spring Preload

5.3 Volume Box damper

The damper installed in the back section of the *Transversal Link* is constantly compressed by the action of the spring that ensure the correct equilibrium position of the *Volume Box*.

Although the compound adopted for manufacturing of the damper ensures a good resistance to the environmental stresses, the part works in an aggressive environment: the operating

temperature can vary in the range of [50,60]°C, with thermal cycles during the alternation of operation and down time of the *Filling Machine*, thermal shock generated by the washing cycles executed with tap water, the Relative Humidity contend is in the range RH [90-100]%, it might be exposed to H₂O₂ both in the vapour and in the liquid phase and it is invested by an alkali solution contained into the cleaning detergents.

All those conditions, combined with the mechanical stresses applied to the rubber, both cyclic during the operations and static during the down time of the equipment, can cause the acceleration of ageing phenomena and enhance creep effects.

In case of failure of the damper, two major aspect can create deleterious consequences on the *Volume Box*: the reduction of the damping effect would create higher impact cycles of the *Volume Box*, that depending on the intensity of the stresses can determine fatigue issues; plastic deformations, that caused a different equilibrium position of the *Volume Box* and consequent variation of the angle of contact against the *Volume Cam*, cracking e completely deterioration of the component, that would completely loose the damping function. In the last two cases, the increasing of the stresses generated at the impact with the *Volume Cam* might generate failure issues.

The plot in the Figure 75 describes the contact force in case of permanent plastic deformation of the damper height of -3 mm. In this configuration the equilibrium position of the *Volume Box* would be achieved with a smaller angle between its back and the horizontal plane, which would modify the approaching angle of to the *Volume Cam*, anticipating the point of contact and increasing the magnitude of the hurt. As purely investigative case, it was considered the permanent deformation of the damper of 6mm, and this case would produce the same effects described above, but with higher intensity.

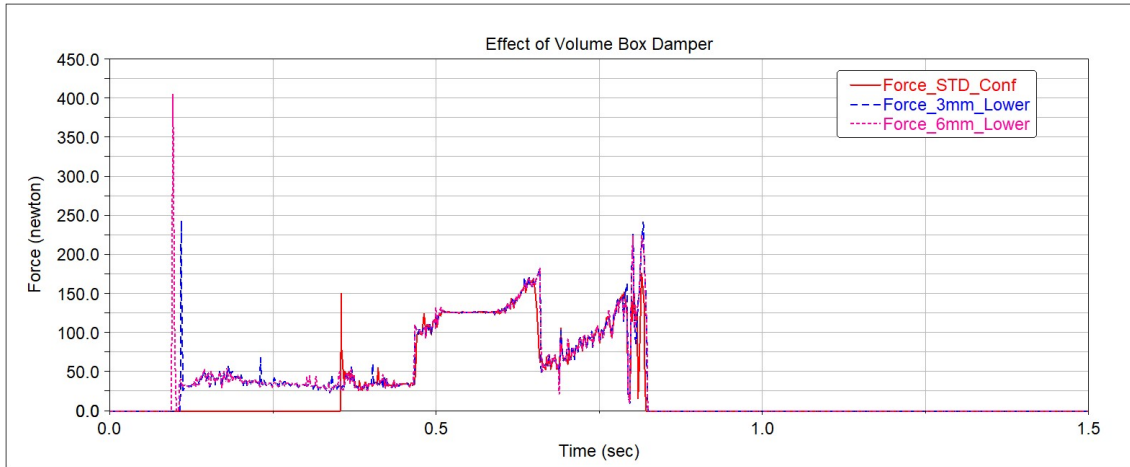


Figure 75: Effects of the ageing of the Volume Box damper

The occurrence of such failure of the damper, would generate higher stresses on the lower section of the *Volume Box*, close to connection of the joint, representing one of the causes of the failure due to fatigue. The Figure 76 shows the typical fatigue failure detected on the components installed in the Customers' premises.



Figure 76: Volume Box broken on in operation

The Figure 77 shows the distribution of the stresses in the *Volume Boxes*, highlighting that highest values are localized in the connecting sections, which correspond the failing points of the component. The stress distributions were calculated with a dynamic analysis executed with the values of impulsive forces calculated during the dynamic simulation, with the intention of underling that the increasing of the impact force might enhance the likelihood of fatigue failures.

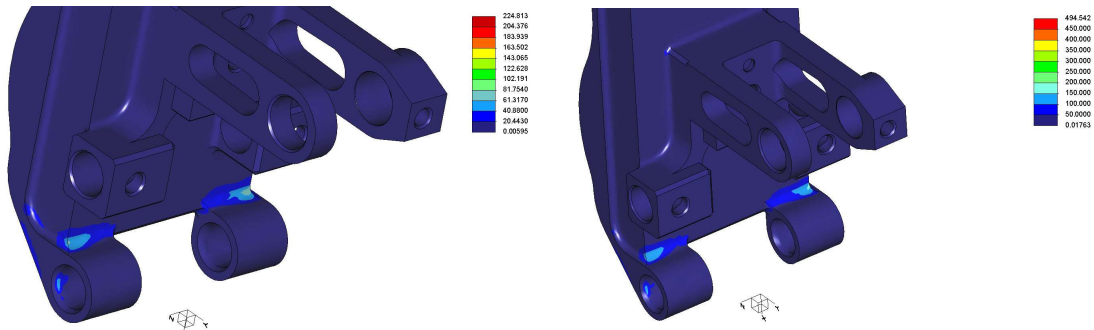


Figure 77: Volume Box Stress Field (MPa)

5.4 Folding Flap Pin

The analysis was carried out for verifying the stresses that are applied on the *Folding Flap* mechanism, if the stop pin (see Figure 78) that limits the maximum opening of the lever is broken:

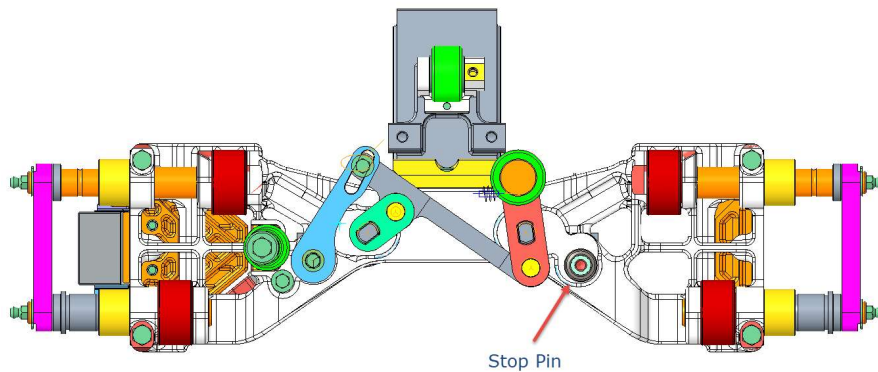


Figure 78: Folding Flap Stop Pin

The curves overlapped in the graphics in Figure 79 focus on the consequence of type of damage: the impulsive force calculated during the first contact impulse between the *Design Correction Cam* and the roller is increased of about 150N, no differences can be highlighted along the trajectory on the cams, but in case of the absence of the Stop Pin the roller of the mechanism gets in contact with the cam in the bottom of the frame, generating an highly intense force, which would be critical for the shaft of the roller in the short term period of operation of the *Jaw System*.

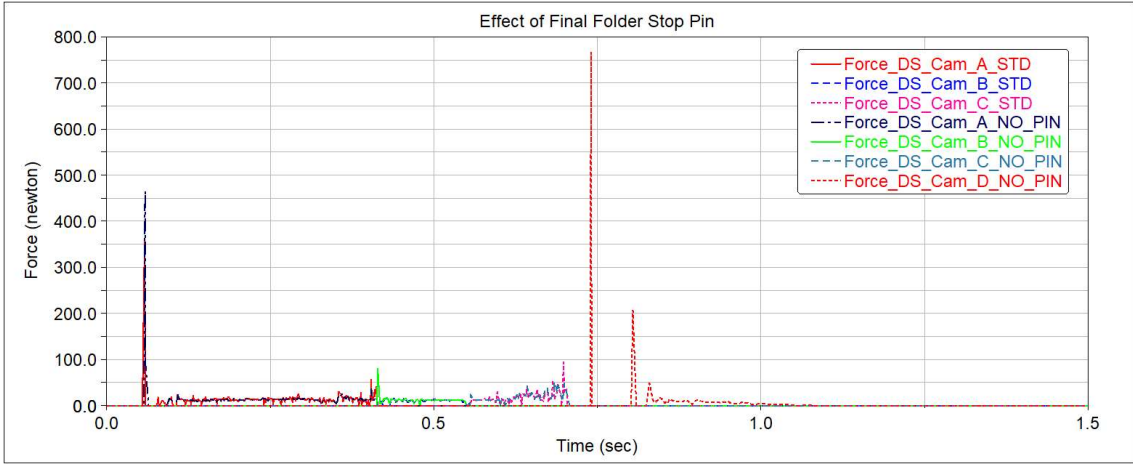


Figure 79: Effects of the breakage of the Stop Pin

6 Cutting Knife

The *Knife* is one of the most critical components of the *Jaw System*, since it is the only element ensuring the proper separation of the packages and its efficiency can also affect the quality and the safety of the final package.

Many versions of the knives exist for the different versions of the equipment and they differ for shape of the teeth, shape of the blade, raw materials, activation principle; the evolutions of the design of this critical component have been related to the peculiar characteristics of the final application.

The different types of *Filling Machine* can alternatively adopt two actuation principles: driving the displacement *Knife* with a cam, as in the model of the *Jaw System* described herein, or moving the *Knife* by means of the application of the hydraulic pressure.

The variety of shapes adopted derived from a continuous optimization process of the design, which was led by the needs appeared during the years and the experiences gained by the designers belonging to the various R&D department around the world.

The materials adopted for manufacturing the knives are influenced by the type of product that the Customers are filling into the package, which influences both the environment where the component should operate, more or less aggressive from the chemical point of view (e.g. high salt content like tomato sauce, or low aggressivity as milk) and the type of packaging material selected, which can have variable stiffness, content of elements in the constitutive layers, resistance to the cutting, abrasive effect on the blade.

The reliability of the *Knife* might be impacted by issues related to wear and corrosion, depending on their final application. At the end of its lifetime, the blade of the *Knife* usually presents a not homogeneous wear along the cutting profile, that is mainly caused by the different stiffness of the packaging material along the transversal direction: at the extremities of the package its higher, since the material bend and clamped, and on the middle has the thickness of three layers, since there is the conjunction of the edges for creating the sealed tube.

The images below show the magnitude of the wear that could generate defect on the package. The Region A is usually not involved in the cutting process, since the *Knife* is wider than the packaging material, hence it can be considered representative of a brand-new component. The Regions B and C work against the stiffest sections of the packaging material, that correspond to the edges and the central part, hence those are the most work out areas.

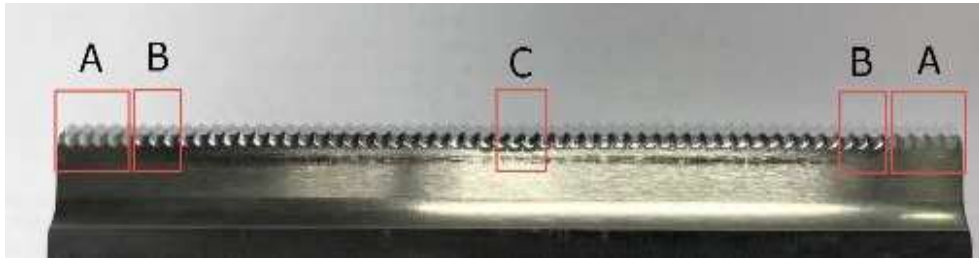


Figure 80: Knife Profile

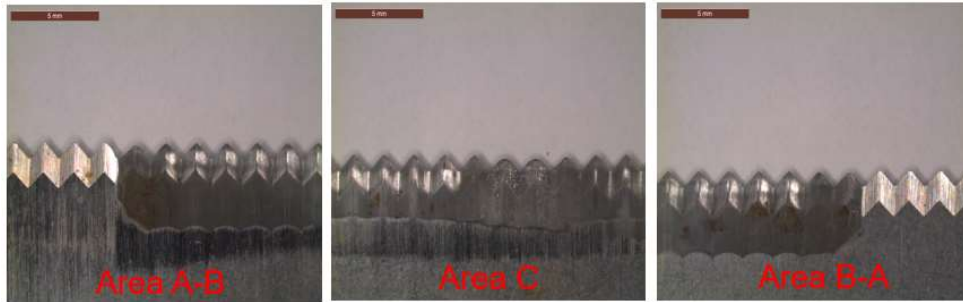


Figure 81: Details of the cutting wedge of the Knife

In order to deeply investigate the performances of the different types of knives and ensure the high reliability of the cutting sub-system, comprehensive activity was defined for better understanding the behaviour of the knives, define the boundary conditions for virtual cutting models and create the degradation model of its performances.

The steps described in this section concerns:

- The investigation of the influence of the parameters competing to the cutting function on the cutting efficiency;
- Experimental collection of data for the creation of the cutting virtual model
- Experimental investigation of the degradation of the *Knife* during its operative life for the definition of the degradation model.

The investigations about the performances of the *Knife* were conducted on a test rig that was designed and manufactured on purpose and equipped with additional sensors in order to provide information about the functionality of the *Knife*.

6.1 Test Rig

The test rig designed for this study was characterized by a different layout in comparison with the cutting mechanism of the *Jaw System* analysed in the first part of this work, selecting the version with the hydraulic actuation instead of the one with the cam.

The reasons of this major difference were related to the flexibility that was required to the testing equipment, which should be able to operate with different sized of components, types of packaging materials, and forces. Moreover, the testing equipment should ensure high repeatability and high working frequency, when it is used for executing the wearing tests.

The layout of the test rig allowed the installation of additional sensors, such as:

- Compression load cell on the rod that is actuating the displacement of the *Knife*. It provides information about the cutting force
- Displacement laser sensor: on the rod connected to the *Knife*. It provides data about the stroke of the *Knife* during the cutting operation.
- Pressure sensors before the actuators that command the clamping of the packaging material and the motion of the *Knife*. They are used as feedback about the response of the hydraulic circuit.

Moreover, the pressure signal during the cutting operation is monitored in other equipment, hence the identification of correlations between the values of this parameter and the status of the *Knife* could improve the performance of the other *Filling Machine*.

The Figure 82 shows the cross section of the cutting station of the test rig.

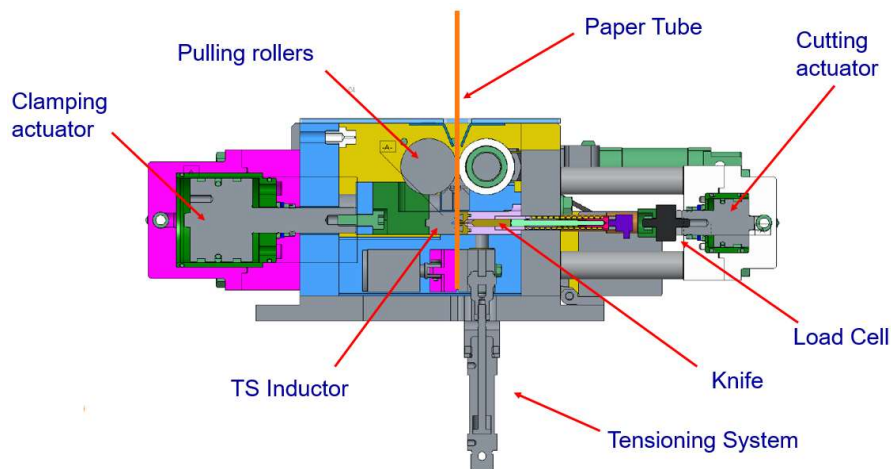


Figure 82: Cross-section of the testing station

The rigid frame (blue and grey component) ensure the resistance and the stiffness of the system to all possible operative conditions, that usually vary with the model of *Filling Machine*.

The actuator on the left side is connected with the *Inductor*, that is responsible of the transversal sealing (top and bottom of the package) of the packaging material. The counterpart (pink element) is fixed to the frame and carries two deformable elements in silicone rubber that press

without damaging the paper tube. The *Knife* slides in the cavity between the elastic elements, moved by the actuator on the right side. The load cell is installed on the rod, between the actuator and the *Knife*.

The displacement sensor is installed just above the load cell and measures the relative displacement between the rod and the frame of the station.

The system allows also the setting of the tension of the packaging material, by means of tensioning system installed below the station that is pneumatically actuated. When the packaging material is between the clamping elements (pink and grey), the Pulling Rollers on the top stop their rotation holding the packaging material, which can be tensioned from the bottom.

The sensors were connected to a National Instrument C-Rio logger and sampled at 20 kHz, a previous measuring campaign demonstrated that there is no loss of information with this sampling rate.

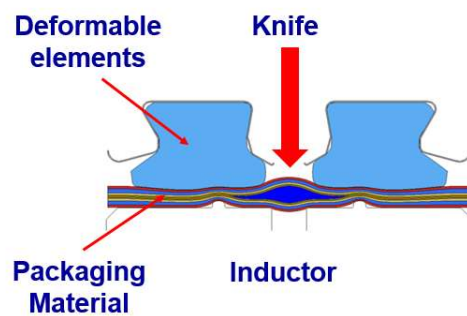


Figure 83: Detail of the interacting element in the cutting process

The cutting process consists in a sequence of phases that can be perfectly reproduced by the testing equipment:

1. Clamping of the packaging material (Deformable elements Vs Inductor)
2. Sealing impulse (Inductor)
3. Cooling of the sealing (Waiting Time)
4. Cutting (*Knife*)
5. Release of the packaging material

The force measured during the cutting operation is plot in the graphic below, it shows some analogies with the cutting curves described in the Chapter 4 and peculiarities can be identified:

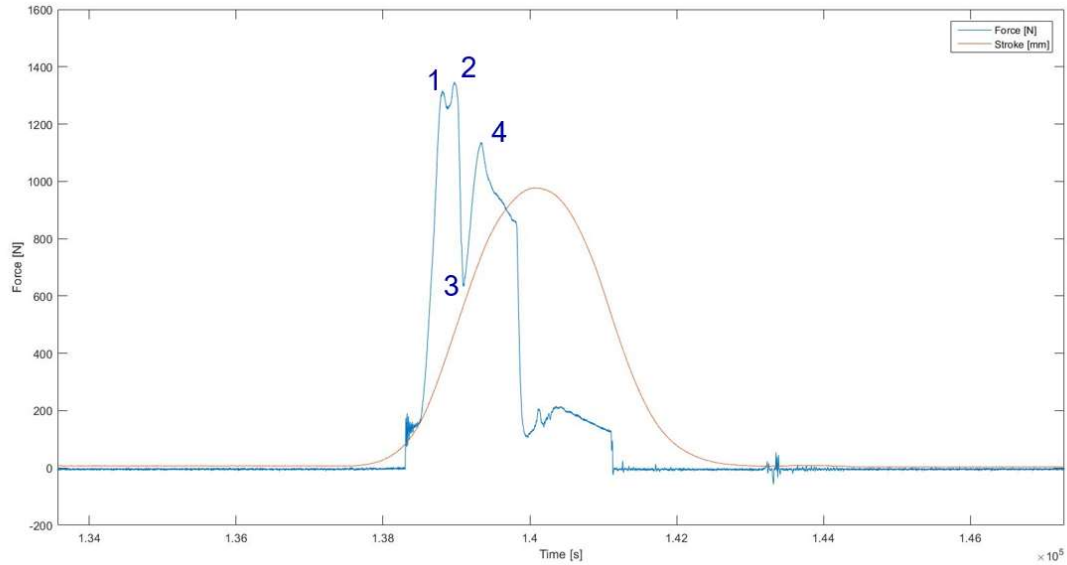


Figure 84: Cutting Force and Knife Position curves

The yellow curve represents the approaching stroke of the *Knife* to the paper tube, in the first part the acceleration is lower due to the inertia of the system and the force value is null since the *Knife* is not in contact with the packaging material yet. The first peak and the fluctuation of the force represents the impact of the *Knife* on the tube and the subsequent stabilization is generated by the first displacement of the packaging material into the groove of the inductor. The sudden growing of the force value up to the peak #1 is caused by the resistance of the packaging material to the deformation imposed by the *Knife*; the valley between the peaks #1 and #2 happens when the tips of the teeth on the *Knife* break and penetrate the packaging material. The peak #2 is occurs when the valleys between the teeth of the *Knife* arrive in contact with the packaging material, facing a wider resistant surface instead of the wedge of the tooth. The valley #3 indicates that the *Knife* has completely separated the two sides of the paper tube and accelerates versus the end of the stroke. The growing of the force up to the peak #4 is determined by the combination of the frictional force between the packaging material and *Knife* and the reaction force generated by the compression and deformation of the two edges of the packaging material into the cavity of the inductor. The next phase is the deceleration of the *Knife* and the conclusion of the displacement, until the backward stroke starts.

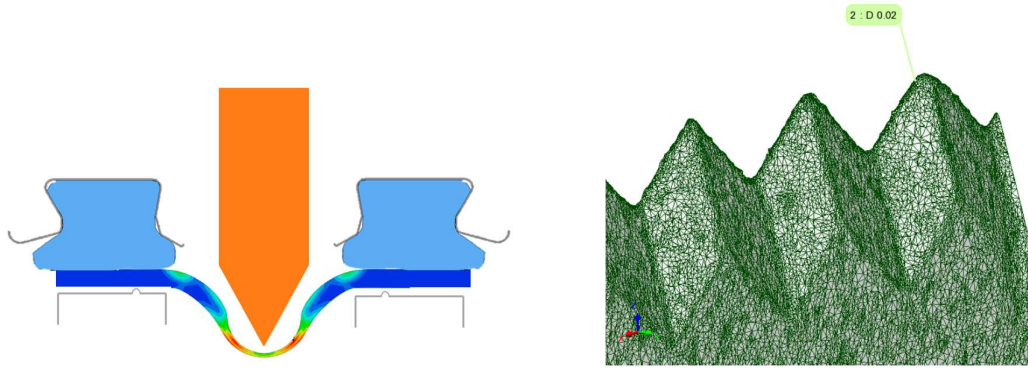


Figure 85: Detail of the cutting process(left) and the Knife teeth (right)

6.2 DoE

The first activity executed on the test rig was finalized to the understanding of the cutting process, aiming to identify the influence of the parameters that participated to the cutting cycle have on the cutting force [28].

The analysis of the cutting system highlighted the following parameters as the most probable contributors to the definition of cutting efficiency:

- a. Magnitude of the clamping force;
- b. Electrical Power of the Sealing Pulse;
- c. Duration of the cooling phase
- d. Tension of the packaging material
- e. Density of the product filled into the tube

The testing campaign was set as a DoE designed according with the Taguchi Method, that is widely adopted for investigating the robustness of the design versus the operating parameters, since it uses a few experimental runs for estimating the main effects.

The DoE was defined on 5 parameters above, which were investigated at 3 stressing levels, generating 27 testing configurations. The same testing structure was replicated on the two types of packaging materials, labelled JL and JLL types, that are characterized by different stiffness, in order to highlight how the different operative conditions on the *Filling Machine* would influence the results.

The set points of the testing variables are listed in the Table 3:

Parameter	Target	Set Point
Clamping force	4'000 N	14.2 bar
	6'100 N	21.6 bar
	7'000 N	24.8 bar
	10'000 N	35.4 bar
Cutting Force	1'900 N	20.0 bar
Cooling Time	-150 ms (from FM standard = 128ms)	Start pulse (100ms) @ 670
	0 ms (from FM standard = 128ms)	Start pulse (100ms) @ 540
	300 ms (from FM standard = 128ms)	Start pulse (100ms) @ 370
Sealing Power	700 W	700 W
	800 W	800 W
	900 W	900 W
Pulling Force	30 N	To be measured
	50 N	To be measured
	70 N	To be measured
Product	No Product	N.A.
	Water	N.A.
	Thicken Water	89% glycerol (CAS 56-81-5)

Table 3: DoE parameters

The trials were executed manually feeding the paper tube to each station, in order to allow the possibility of filling the tube with the product.

In order to have a repeatable hydraulic load on at the inductor height, the tube was filled with 300ml of solution before starting the sampling sequence and then 30 cutting cycles are completed. The consumption of the product during those cutting cycles was considered negligible from the hydraulic load perspective, since the pitch between two consecutive cuts was minimized to about 300 mm.

The setting of the hydraulic parameters was checked with the pressure sensors installed in the circuit, by pressurizing the circuit and checking the value once the system is at the equilibrium (see Figure 86).

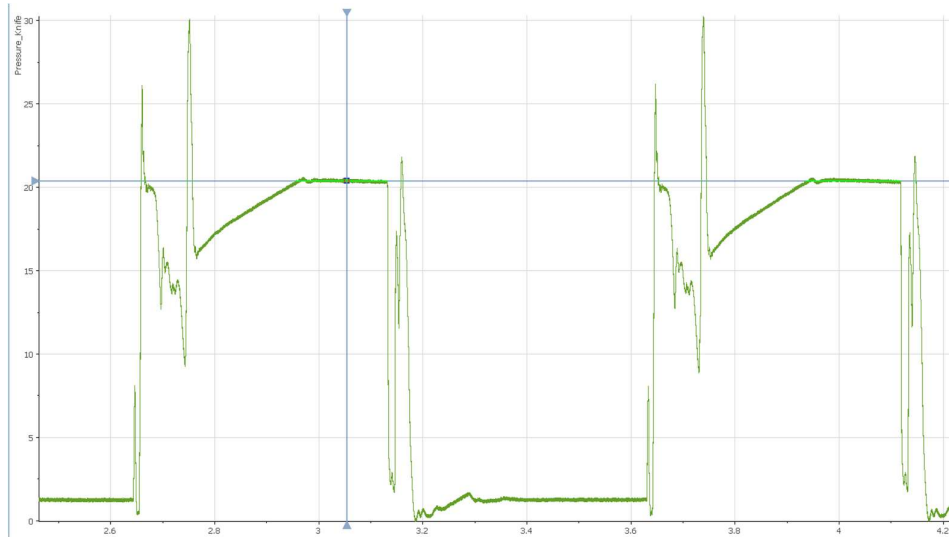


Figure 86: Testing Station Set-Up

The force of the tensioning system was set modulating the pneumatic pressure on the feedback provided by a dynamometer (see Figure 87).



Figure 87: Testing Station Set-Up

The testing sequence of the DoE trials is shown in the Tables 4-6. Although the randomization of the trials by mixing the parameters is the best approach for the DoE, it was decided to organize the tests in order to minimize the amount of changes in the settings of the hydraulic circuit, hence the likelihood of generating differences of the actual values of the pressure, since the settings are manually defined by acting the regulators.

Run	Clamping Force [bar]	Pulling Force [N]	Sealing Power [W]	Start pulse time DoE script	Product	PM
#0	14.2	Check without packaging material				
#1	14.2	30	900	370	No Product	JLL
#2	14.2	30	900	370	No Product	JL
#3	14.2	30	800	540	No Product	JLL
#4	14.2	30	800	540	No Product	JL
#5	14.2	30	700	670	No Product	JLL
#6	14.2	30	700	670	No Product	JL
#7	14.2	50	700	540	Water	JLL
#8	14.2	50	700	540	Water	JL
#9	14.2	50	800	370	Water	JLL
#10	14.2	50	800	370	Water	JL
#11	14.2	50	900	670	Water	JLL
#12	14.2	50	900	670	Water	JL
#13	14.2	70	800	670	Thicken Water	JLL
#14	14.2	70	800	670	Thicken Water	JL
#15	14.2	70	700	370	Thicken Water	JLL
#16	14.2	70	700	370	Thicken Water	JL
#17	14.2	70	900	540	Thicken Water	JLL
#18	14.2	70	900	540	Thicken Water	JL

Table 4: DoE Tests

Run	Clamping Force [bar]	Pulling Force [N]	Sealing Power [W]	Start pulse time DoE script	Product	PM
#19	24.8	30	900	670	Thicken Water	JLL
#20	24.8	30	900	670	Thicken Water	JL
#21	24.8	30	800	370	Thicken Water	JLL
#22	24.8	30	800	370	Thicken Water	JL
#23	24.8	30	700	540	Thicken Water	JLL
#24	24.8	30	700	540	Thicken Water	JL
#25	24.8	50	700	370	No Product	JLL
#26	24.8	50	700	370	No Product	JL
#27	24.8	50	800	670	No Product	JLL
#28	24.8	50	800	670	No Product	JL

#29	24.8	50	900	540	No Product	JLL
#30	24.8	50	900	540	No Product	JL
#31	24.8	70	900	370	Water	JLL
#32	24.8	70	900	370	Water	JL
#33	24.8	70	800	540	Water	JLL
#34	24.8	70	800	540	Water	JL
#35	24.8	70	700	670	Water	JLL
#36	24.8	70	700	670	Water	JL

Table 5: DoE Tests

Run	Clamping Force [bar]	Pulling Force [N]	Sealing Power [W]	Start pulse time DoE script	Product	PM
#37	35.4	30	900	540	Water	JLL
#38	35.4	30	900	540	Water	JL
#39	35.4	30	800	670	Water	JLL
#40	35.4	30	800	670	Water	JL
#41	35.4	30	700	370	Water	JLL
#42	35.4	30	700	370	Water	JL
#43	35.4	70	800	370	No Product	JLL
#44	35.4	70	800	370	No Product	JL
#45	35.4	70	900	670	No Product	JLL
#46	35.4	70	900	670	No Product	JL
#47	35.4	70	700	540	No Product	JLL
#48	35.4	70	700	540	No Product	JL
#49	35.4	50	800	540	Thicken Water	JLL
#50	35.4	50	800	540	Thicken Water	JL
#51	35.4	50	900	370	Thicken Water	JLL
#52	35.4	50	900	370	Thicken Water	JL
#53	35.4	50	700	670	Thicken Water	JLL
#54	35.4	50	700	670	Thicken Water	JL

Table 6: DoE Tests

The results of DoE showed that the force required for cutting the packaging material is strongly influenced by the heating power used for sealing the tube, since this strongly impact the physical status of the polyethylene layer of the packaging material that is in the solidification phase after the sealing.

An important role is also played by the combination of the properties of the product and the clamping force applied to the packaging material, since those affect the amount of product that is trapped into the packaging material and between the deformable elements. Increasing the clamping force, the deformation of the rubber element is wider and the trapped product is more squeezed, increasing the tensions within the packaging material and requiring a lower force of the *Knife* for penetrating the tube.

The Pareto Chart calculated on the response function of the cutting force highlighted that the value of the sealing power has a relevant influence on the results, but the major effects are achieved in combinations with the other parameters (see Figure 88).

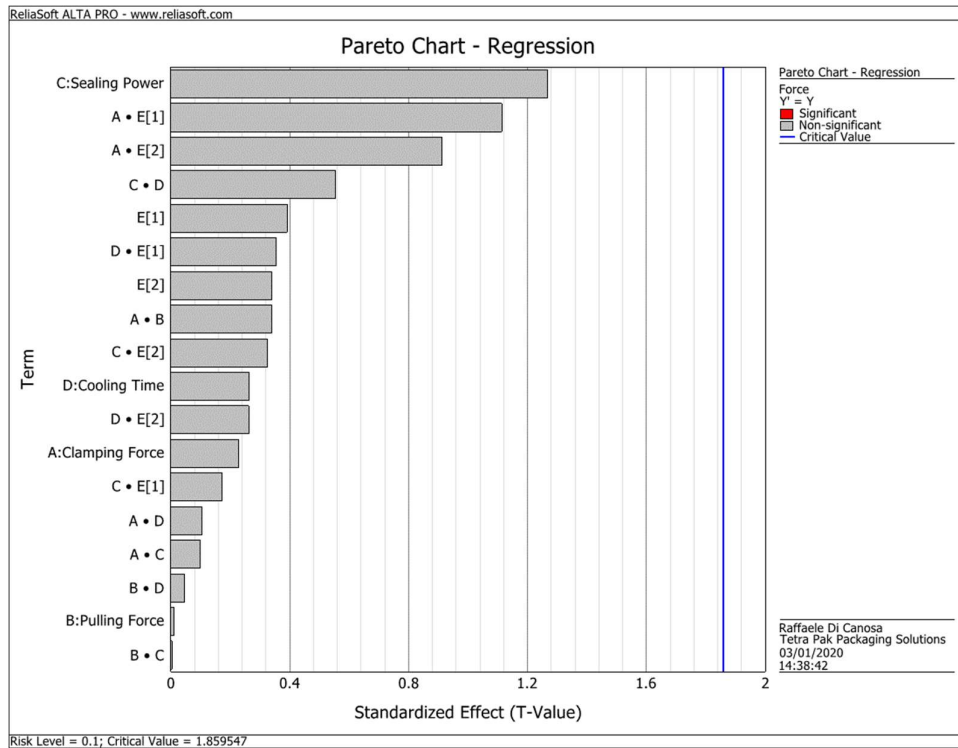


Figure 88: Main Effects Pareto Chart

The analysis of the Main Effects Plots (see Figures 89 and 90) calculated for the for the two datasets, showed that the correlations between the variables are analogous for the two types of packaging material, but the average value of the cutting force achieved differs with the stiffness of the packaging material and it is higher with the most stiff one (JLL Type).

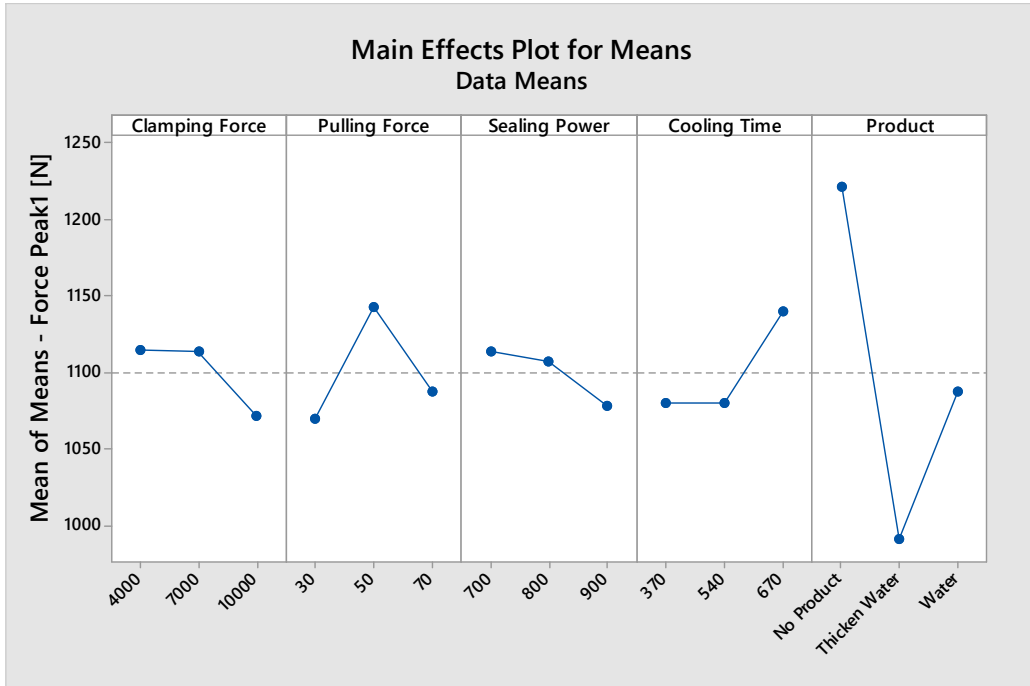


Figure 89: Main Effect Plot of Peak Force - JL Packaging material

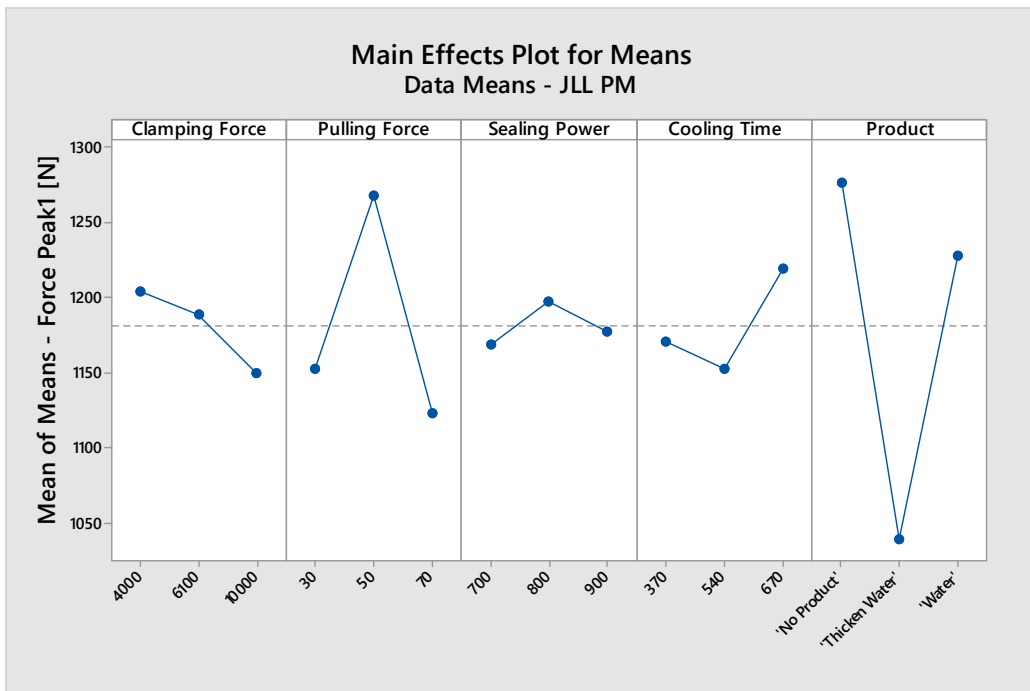


Figure 90: Main Effect Plot of Peak Force - JLL Packaging material

The effect of the Clamping force is connected to the cutting force because of two aspects: the first one is the slipping effect between the *Dolly* (yellow element in the Figure 90), that transfers the tension to the upstream packaging material when the *Knife* is approaching and deforming it; the second contribute is related to the deformed equilibrium achieved by the *Dolly* after that

the clamping load is applied: the higher the clamping load is, the lower the additional deformation occurring during the impact with the *Knife* is.

The correlation between the cutting and the pulling forces is justified by the difference of the tension field of the packaging material before the contact with the *Knife*, thus the energy required for separating the layers is lower. The value in highest value highlighted in the middle level would require a deeper investigation, through further tests and simulations.

The correlation between the sealing power and the cooling time should be analysed in conjunction, since those values influence the status of the polyethylene during the cutting cycle: high sealing powers and short cooling time, make the polyethylene not fully solidified at the passage of the *Knife*, acting as highly deformable body, whilst the cutting conditions with against a fully solidified polyethylene would generate a toughest material to cut, hence highest forces are required.

An interesting achievement was correlated to the influence of the type of the product, since cutting the paper tube without the presence of the product entrapped into the bag (blue elements between the deformable bodies) requires a higher force. The explanation of the phenomenon is related to the pretensions that is applied on the packaging material by the squeezed product, that pressurized the bag, requiring a lower force to the *Knife* for initiating the penetration and propagating the fracture.

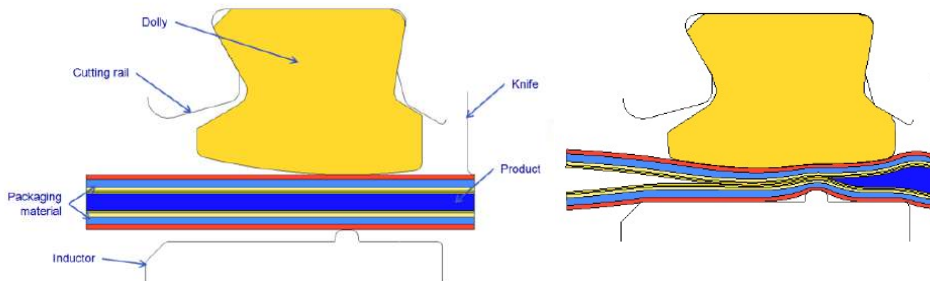


Figure 91: Clamping Phase Detail

The correlation with the tensional field of the packaging material was confirmed by additional tests executed in the same configuration and with the exclusion of the heating phase, so that the nature of this effects was confirmed to be purely mechanic.

6.3 Cutting Model

The virtual analysis of the cutting process is going to be approached by a simplified model that would provide prediction of the behaviour of the *Knife* operating in different conditions, comparable with the ones described in the DoE, [29], [31].

In order to attempt the creation of a reliable model, in addition to the data collected during the DoE phase, some more information would be needed for modelling the interfaces of the components.

The simplified virtual model consists a reduced cross-section of the real components, that are accurately modelled as in the reality.

The component included in the model are:

- The inductor
- The packaging material
- The dolly
- The cutting rail
- The *Knife*

The experimental procedure defined aimed to monitor the tensions applied at the extremities of the packaging material, out of the cutting assembly, when operating with different parameters of the interfaces, in order to understand the magnitude of the slipping effects between the packaging material and the *Dollies* and how their ageing status combined with the magnitude of the clamping influence the cutting.

The specimens involved in the test were:

Component	Note	
<i>Knife</i>	Standard Component	
	Rounded Edge	
	V-Shape Edge	
Dolly	Run 250h degradation test	
	New	
Packaging Material	A Configuration	Single layer of packaging material of width 88 mm
	B Configuration	Double layer of packaging material of width 88 mm
	C Configuration	Flattened Tube (LS Sealed)

Table 7: Testing Configuration

As demonstrated during internal tests, the characteristics of the *Dolly* change over the time, due to ageing phenomena occurring for the combination of thermal cycles, exposure to the aggressive environment with the presence of H₂O₂ vapours.

The graphic in the Figure 92 reports the variations of the average hardness measured along the length of the component, after different working intervals in two different testing equipment, emulating the pure mechanical stress (blue dots) and the both the mechanical and the environmental stresses (red dots).

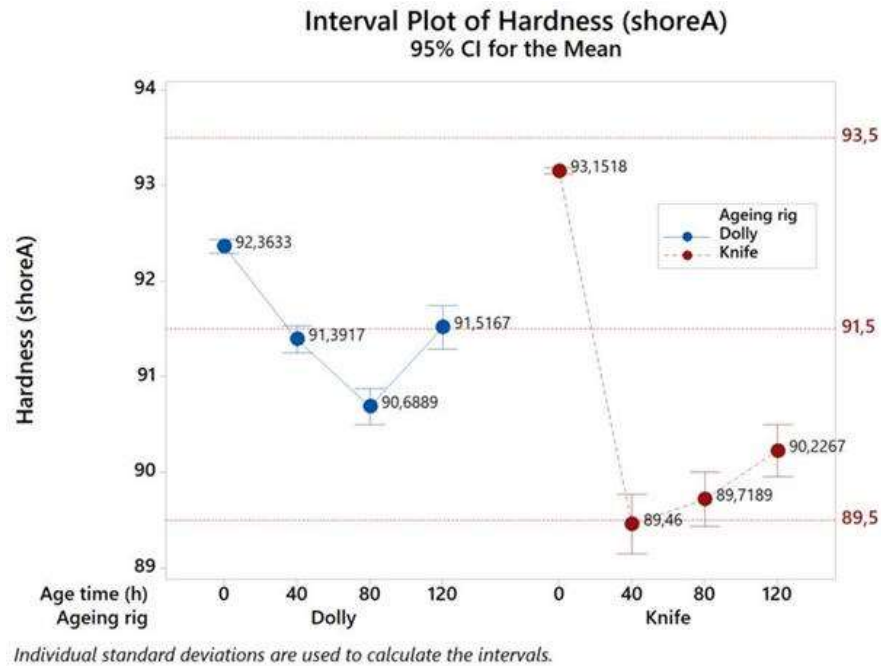


Figure 92: Dolly Ageing & Hardness Test

For this test two types of different prototyping knives were manufactured, they have a continuous profile of the cutting edge, in order to exclude the contribute of teeth penetration in some results and to have a more simple configuration to investigate in the first stages of the creation of the cutting model.

The cross section of the *Knife* prototypes was designed as a sharp wedge with the tip angle of 30°, as for the standard *Knife*, and one with a rounded and continuous profile (see Figure 93).

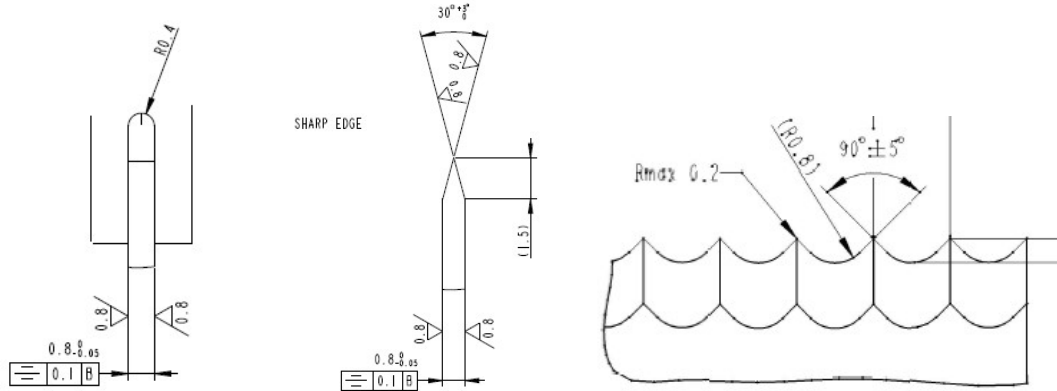


Figure 93:Knives Details

The testing campaign was executed on the same test rig used during the DoE investigation. The testing station was equipped with a tool instrumented with two load cells that were connected to the extremities of the packaging material on the top and the bottom of the cutting station (see Figure 94). The tension of the packaging material was set by manually applying a relative displacement between the two section of the frame, and once the prescribed value was achieved, the cutting cycle was started.

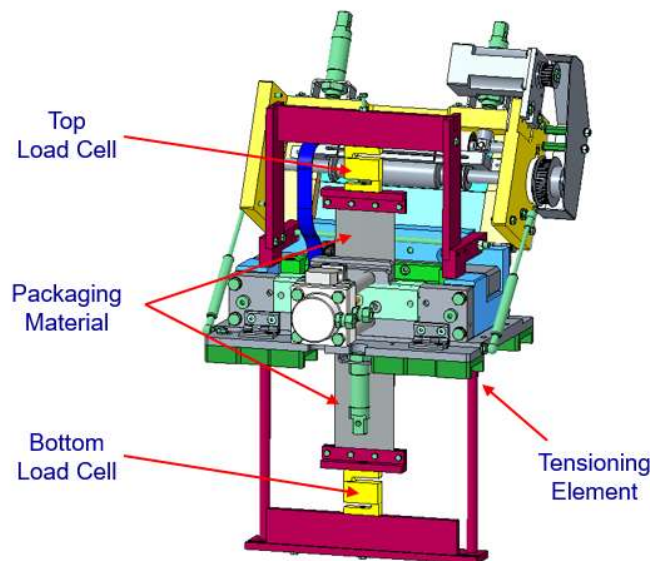


Figure 94: Tension Measuring Tool

The setting parameters adopted for the trials were:

Parameter	Target	Set Point
Cutting Force	1'900 N	20.0 bar
Clamping Force Min	4'000 N	14.2 bar
Clamping Force Max	10'000 N	35.4 bar

Tensioning Force Min	30 N	-
Tensioning Force Max	70 N	-
Cooling Time	Standard	Start pulse @ 540
Cycle time	800 ms	
Pulsing duration	100 ms	

Table 8: Testing Parameters

The cutting testing configurations executed are listed in the Tables 9,10,11 and their quantity was reduced from the one initially defined because the *Knife* with the round edge was not suitable for the required function, hence it would not have been produced useful data.

Trial	Knife	PM Conf.	Water	Tensioning Force	Dolly	Clamping Force	Cutting Force
17	V-Shape Edge	A	Dry	30N	New	14.2 bar	1'900 N
18		B					
19		C					
20		A	Dry	70N			
21		B					
22		C					
23		C	Wet	30 N			
24		C		70N			
25		A	Dry	30N	Old		
26		B					
27		C					
28		A				Dry	70N
29		B					
30		C					
31		C	Wet	30 N			
32		C		70N			

Table 9: Testing Configurations

Trial	Knife	PM Conf.	Water	Tensioning Force	Dolly	Clamping Force	Cutting Force
33	STD	A	Dry	30N	New	14.2 bar	1'900 N
34		B					
35		C					
36		A	Dry	70N			
37		B					
38		C					

39		C	Wet	30 N	Old		
40		C		70N			
41		A	Dry	30N			
42		B					
43		C					
44		A	Dry	70N			
45		B					
46		C					
47		C	Wet	30 N			
48		C		70N			
Trial	<i>Knife</i>	PM Conf.	Water	Tensioning Force	Dolly	Clamping Force	Cutting Force
66	V-Shape Edge	A	Dry	30N	New	35.4 bar	1'900 N
67		B					
68		C					
69		A	Dry	70N			
70		B					
71		C					
72		C	Wet	30 N			
73		C		70N			
74		A	Dry	30N	Old		
75		B					
76		C					
77		A	Dry	70N			
78		B					
79		C					
80		C	Wet	30 N			
81	C	70N					

Table 10: Testing Configurations

Trial	<i>Knife</i>	PM Conf.	Water	Tensioning Force	Dolly	Clamping Force	Cutting Force
82	STD	A	Dry	30N	New	35.4 bar	1'900 N
83		B					
84		C					
85		A	Dry	70N			
86		B					

87		C					
88		C	Wet	30 N			
89		C		70N			
90		A	Dry	30N	Old		
91		B					
92		C					
93		A	Dry	70N			
94		B					
95		C					
96		C	Wet	30 N			
97		C		70N			

Table 11: Testing Configurations

From an analysis of the acquisitions (see Figure 95), 3 macro areas can be distinguished, with different trends of the force read by the upper load cell (**red**, hereinafter called **F_{top}**) and the read force by the lower one (**green**, from here forward called **F_{bot}**):

- a. The initial phase in which both forces have a value equal to the tensioning force
- b. The sealing-cutting phase in which the forces diverge from their initial value and take on different values
- c. The final phase in which both forces tend to 0

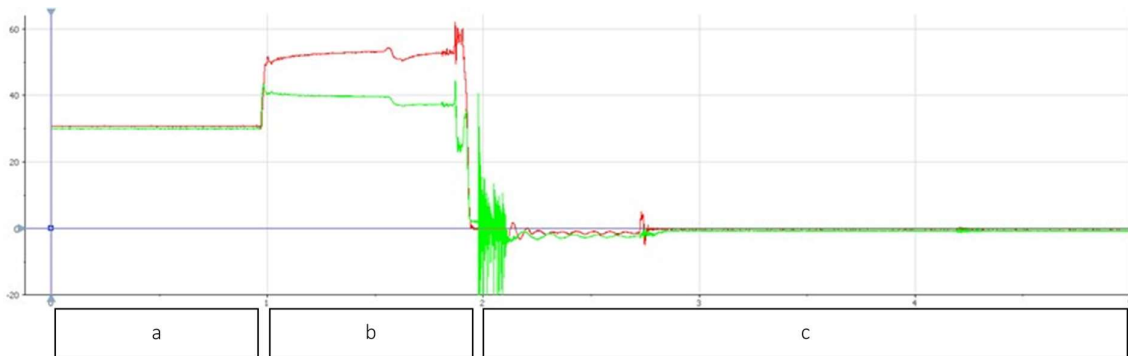


Figure 95: Tension Measurement

The discriminating factor between the initial phase in which both forces have the value equal to the tensioning force (phase A) and the sealing-cutting process in which the forces diverge from their initial value (phase B) is the Jaws closing, as highlighted in the Figure 96.

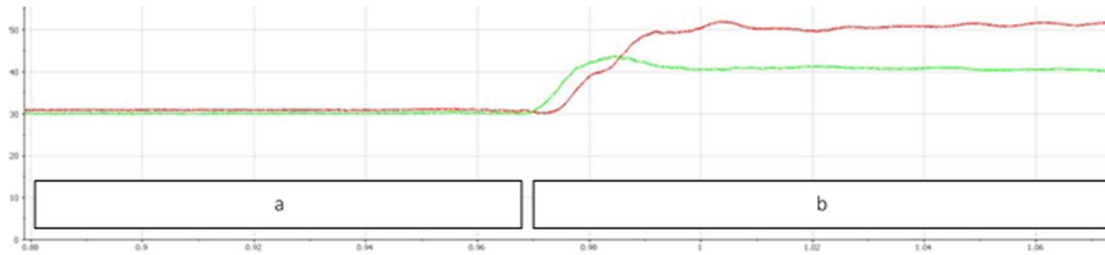


Figure 96: Tension Measurement

The phase on which the analyses are concentrated is that of welding and cutting (phase b). In this phase, the sealing pulse, the cutting force, and *Knife* displacement change their values from the initial 0 (see Figure 97).

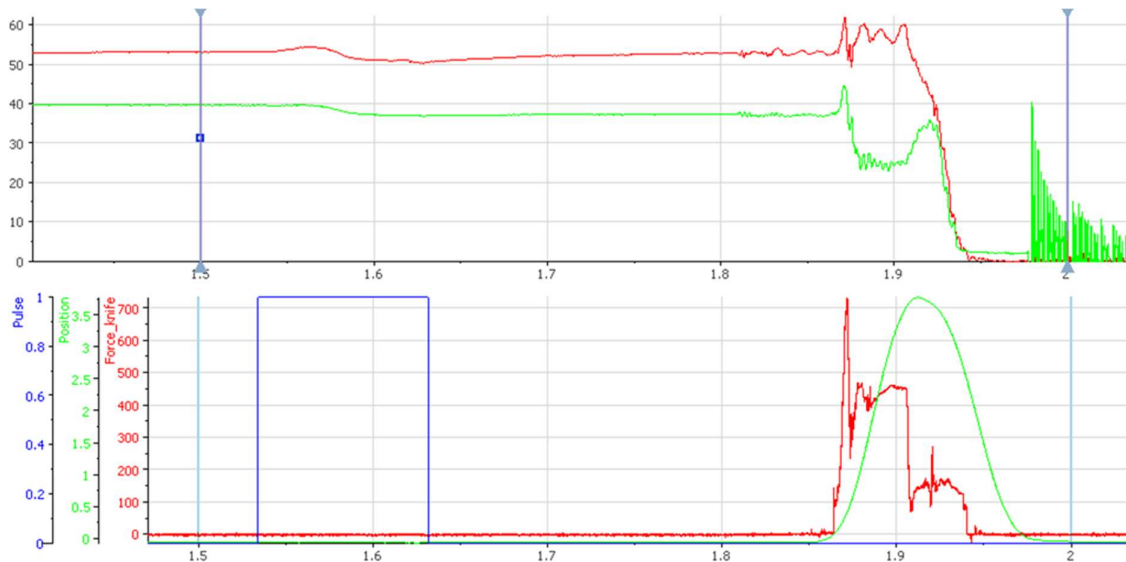


Figure 97: Tension Measurement

From the graph above it can be seen that:

- The maximum value of the cutting force (“Force_Knife”) is about 700 N because in this specific graph the trial with PM in A configuration (Single layer)
- The sealing pulse affects the trends of F_{top} and F_{bot}

In the phase b, 5 stages can be further distinguished, each with its own peculiarities in terms of the performance of the forces (see Figure 98):

1. Welding phase: F_{top} and F_{bot} have constant values, with F_{top} greater than F_{bot} in most tests
2. Knife approach to packaging material, with F_{top} and F_{bot} reaching their maximum values
3. Start of the cutting phase, with constant or slightly decreasing F_{top} and decreasing F_{bot}

4. Completion of the cutting phase, with constant F_{top} and F_{bot}
5. Phase of Knife withdrawal and opening of the jaws, with F_{top} and F_{bot} decreasing up to the value 0.

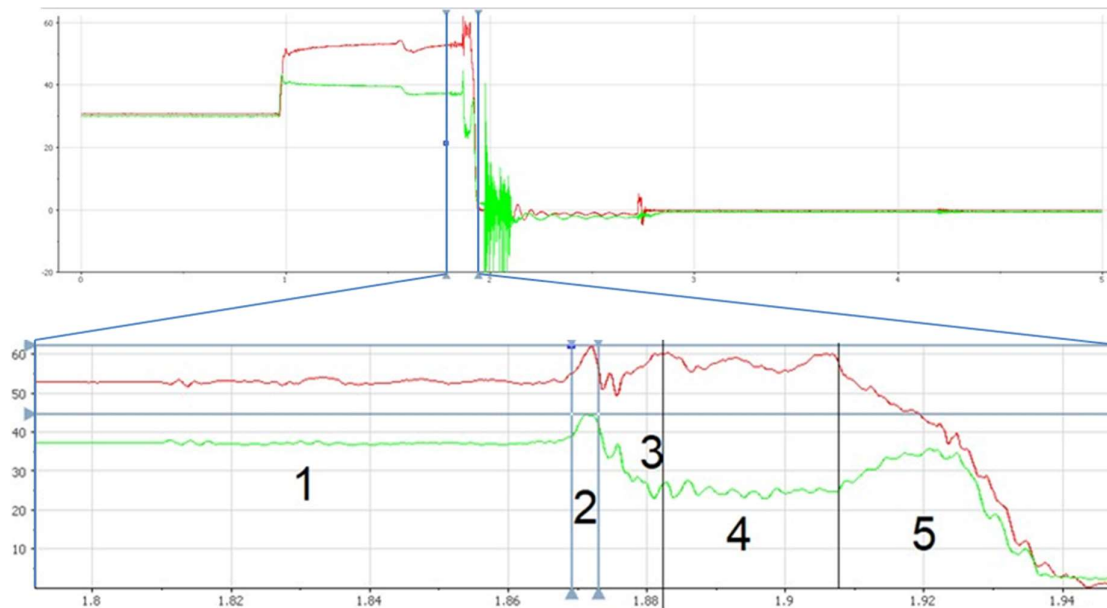


Figure 98: Tension Measurement

To evaluate the effect of the *Knife* on the variation of the internal tension of the packaging material, the difference between the peak of force reached in phase 2 (when the *Knife* approaches the packaging material still intact, which opposes the maximum resistance to the cutting action) and the almost constant force value measured in phase 1 (when the welding phase is about to be completed and the *Knife* is still stationary) is analyzed.

The following graphics summarize the results obtained by trials, highlighting the main effects of the parameters on the cutting force and on the variation of the tension during the cutting phase in the top and the bottom sections of the tool.

The Main Effect plot (see Figure 99) of the cutting forces shows that the V-shaped continuous profile would improve the cutting efficiency, by lowering the force required for separating the two edges of the packaging material. The contribute of the configurations of the packaging material demonstrated a predictable trend, but it underlines the correlation between the cutting force and the width of the packaging material is not linear and highlights the contribute of the stiffer region that are created in the corners and in the middle of the packages [35].

The effects of pretension, dolly and clamping force confirmed to have a minor impact as discovered during the formed DoE test.

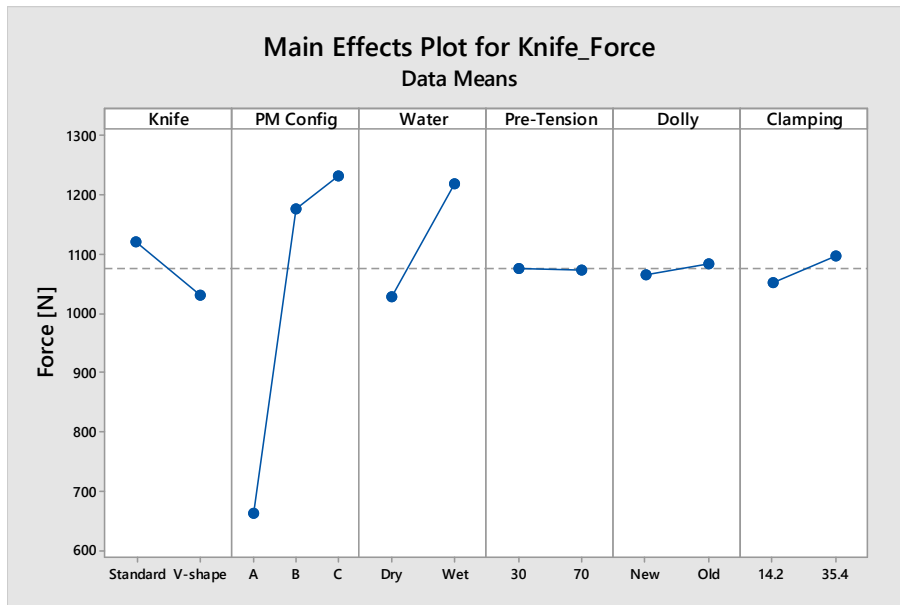


Figure 99: Main Effect Plot - Knife Force

The main effects plots elaborated for the variations of the tensions during the cutting face, showed the same correlation for both sections (see Figures 100 and 101).

An interesting aspect was related to the contribute of the shape of the *Knife*: the V-Shaped profile requires a lower force for cutting the packaging material, but the higher tension measured during the test suggest that its profile facilitate the slipping between the packaging material and the *Dolly*.

The influence of the packaging material width is coherent with the expectations, due to the increased width; more investigations will be required for confirming the effect detected in the top section.

The effect of the water on the surface of the packaging material reduced the friction coefficient, thus a higher slipping.

The ageing of the *Dolly* showed a slightly improving effect in term of sliding, it might be related either to the modifications of the surface characteristics or to the deformed shape assumed after the compression and the curvature imposed to the packaging material on the *Inductor*.

The clamping force has the dominant effect on the slipping phenomenon.

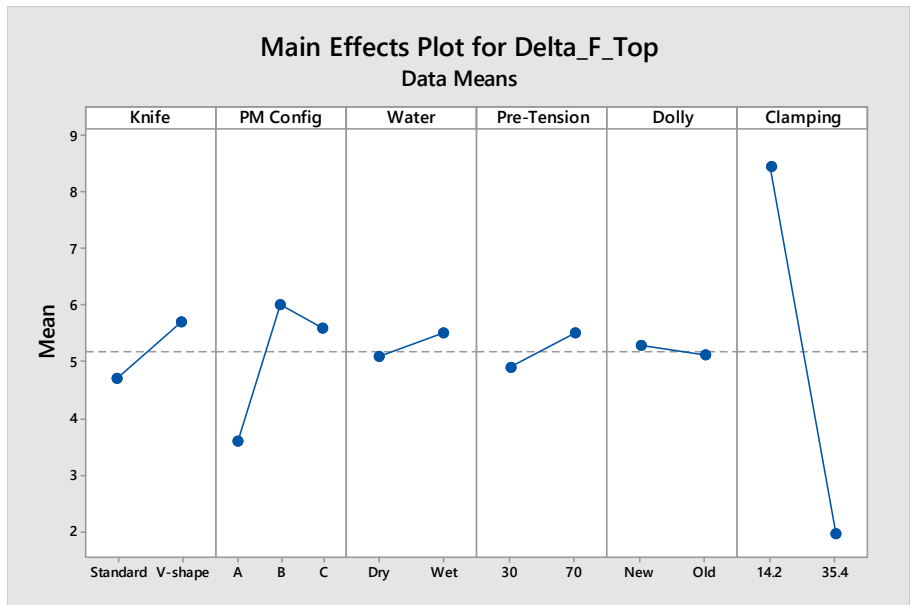


Figure 100: Main Effect Plot - Delta Tension Top Station

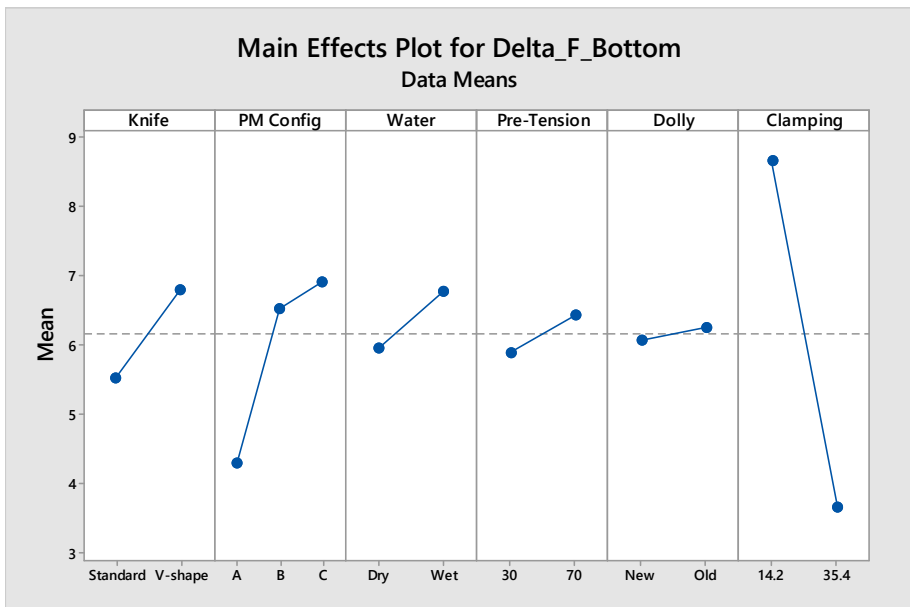


Figure 101: Main Effect Plot - Delta Tension Bottom Station

6.4 Degradation Model

The creation of a degradation model is the last aspect that should be covered for ensuring the reliability of the mechanical system: in this way it would be possible after to estimate the lifetime of the component and actuate the maintenance strategy the best fits the application.

The degradation of the performances of the *Knife* would be related to the capability of the system of performing the cutting function [30], [34].

Depending on the system where the *Knife* installed, the loss of the functionality might be related to different aspects: in the application where the *Knife* is driven by an hydraulic force, the degradation would be generated by a variation of the required force for separating the layers of packaging material, drafting the extreme scenario that the delta between the force required by the function and the one available in the actuating circuit is not sufficient for ensuring the cutting and the desired quality of the separated edges.

In the systems where the *Knife* is actuated with a cam, the loss of functionality would be connected both to critical variation of the shape of the *Knife* and to the variation of the force required for completing the process, since in this case the effects would be either a delayed cutting, that can compromise the synchronization of the equipment or the bad quality of the cut edges.

In order to cope to this need, a lifetime test was designed for being executed on the test rig adopted in the previous measuring activities.

6.5 Test rig set up

The test rig (see Figure 102) consists in six testing stations designed as the one described in the previous paragraph and integrated into a frame that ensures the supplying of packaging material in the shape of a sealed and flattened tube.

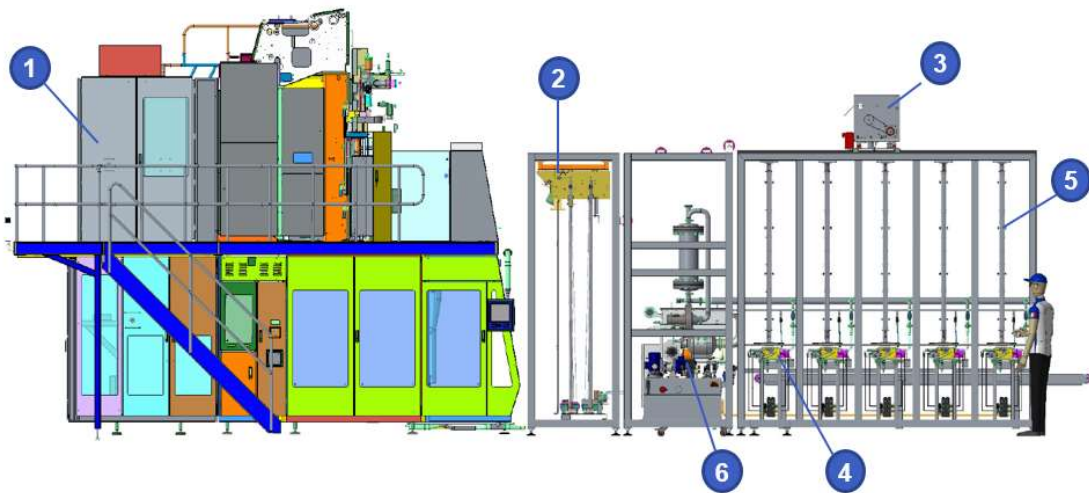


Figure 102: Test Rig

In order to feed a paper tube to the testing stations, a module derived from a *Filling Machine* is installed before the testing stations: the standard In Feed and Superstructure of a *Filling Machine* ensure the tube forming and the longitudinal sealing (1).

In the area of the machine body, the *Jaw System* was replaced by two rollers that flatten and pull the paper tube. The tube passes then through a magazine (2) analogous to the ASU one and it is supplied to the shutter (3) which cyclically refill the magazine of each testing station (5) with a segment of paper tube 2.5m long.

The Chemical Module (6) supplies to the testing stations the conditioned air, whose set point is fixed at 50°C and a chemical solution that is sprayed in the packaging material into the testing chamber for emulating the combined effect of the emulates the combined effect of H₂O₂ and the most aggressive products.

The composition of the solution was defined during laboratory tests focused on the corrosion of the inductors:

- 7,5 g/l anhydrous citric acid (CAS:77-92-9)
- 16 g/l di bibasic sodium citrate 1.5 hydrate (CAS:6132-05-4)
- 0,26 ml/l di Hydrogen Peroxide 35%
- 0,05 g/l di NaCl

Which is required for obtaining a solution having pH 4 + 100 ppm H₂O₂ + 50 ppm NaCl.

The testing station (4) is the system previously examined.

The test rig emulates all the real working conditions of the *Knife*, with the exception of the presence of the product into the tube.

The test was started on two types of knives, which differ for the raw materials Bolher and Stellite. The Stellite ensures the highest resistance to the corrosive environments, but the nominal resistance to impacts and mechanical stresses is slightly lower.

Three specimens for each material started the degradation campaign, that at the time of this publication is still on going.

The target duration of the trial is 4.5 million of cutting cycles and at the data available till the creation of this work covers the first 2 million of cycles.

The sampling routine defined for the trial measured 100 subsequent cutting cycle each 50'000 cycles, in order to draft a trend of the degradation of the system [37].

The data sets contain both the process values of the test rig and the trends of the cutting force and the displacement of the knives.

The graphics proposed in the Figures 103 and 104 show the trends of the force in the different cutting stations, and the specimens were grouped type of raw material.

The trends show some fluctuation of the measurement, which is likely related to the characteristics of the packaging material adopted during the test, but in both cases is visible a growing trend. In the future activities the correlation between the cutting force and loss functionality of the system will be mapped, in order to know both the variation rate and acceptability limit.

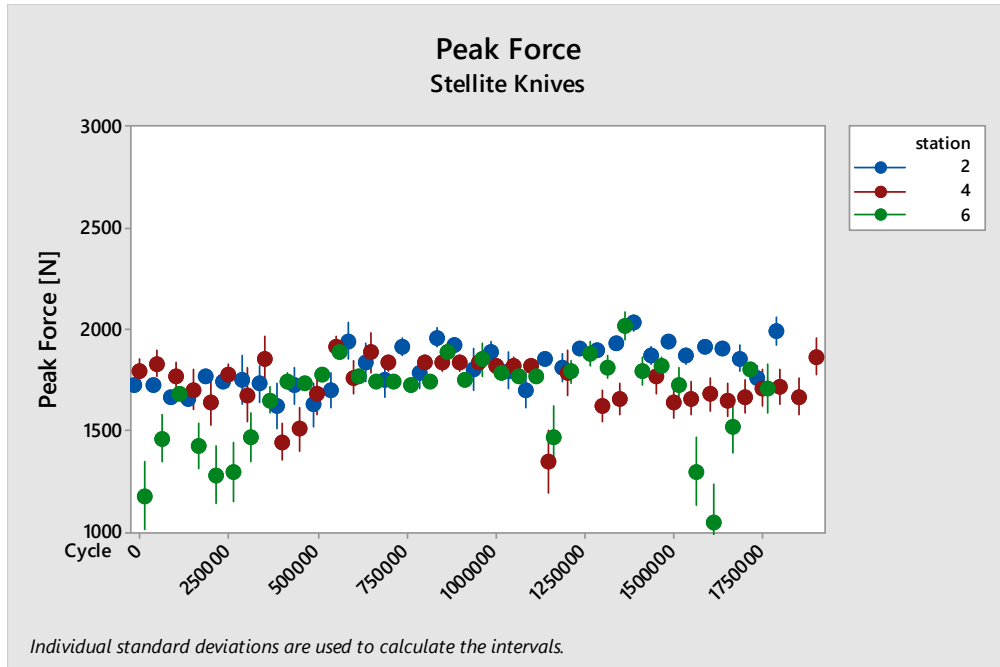


Figure 103: Peak Force Trend - Bolher Knives

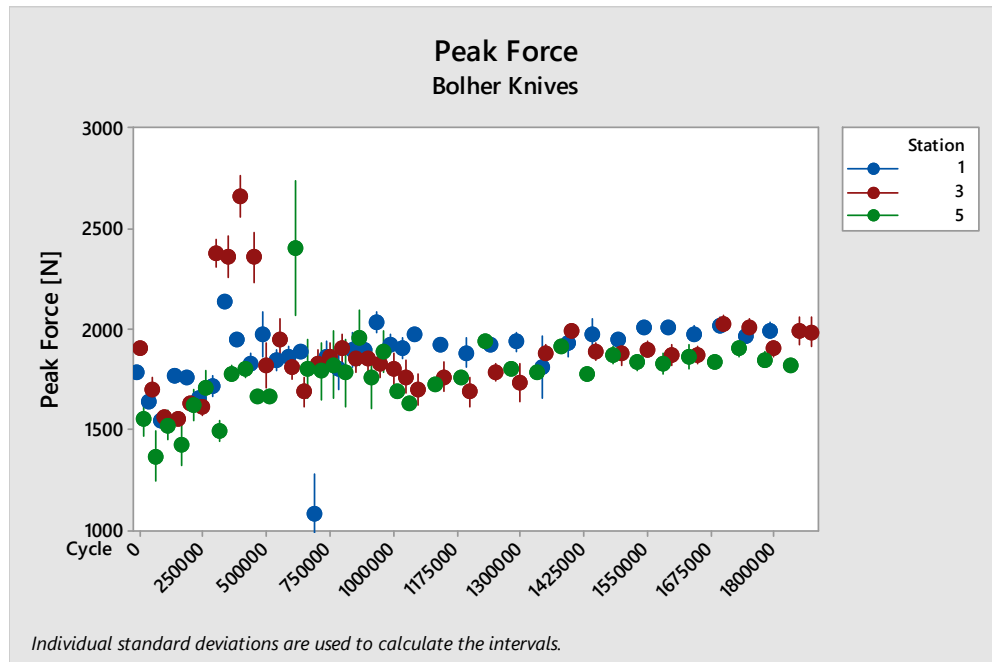


Figure 104: Peak Force Trend - Stellite Knives

Other potential predictors have been monitored, such as the cutting work, the average slope of the cutting phase or the cutting duration, but at this stage of the lifetime test none of those provided a clear trend than the cutting force [33].

In addition to the functional measurements, the specimens were physically inspected, both by means of a 2D profilometry, that highlights the reduction of the teeth height caused by the wearing process, and by a 3D laser scansion, in order to map the evolution of the wear rate on the entire *Knife* [32], [36].

The expectation is to correlate the geometrical variation of the dimensions of the *Knife* with the changes of the functional parameters, coupling both information in the same degradation model [38].

The Figure 105 shows the wear distribution of one specimen, after 1'125'000 cycles and it is referred to the scansion collected on the same component before starting the test.

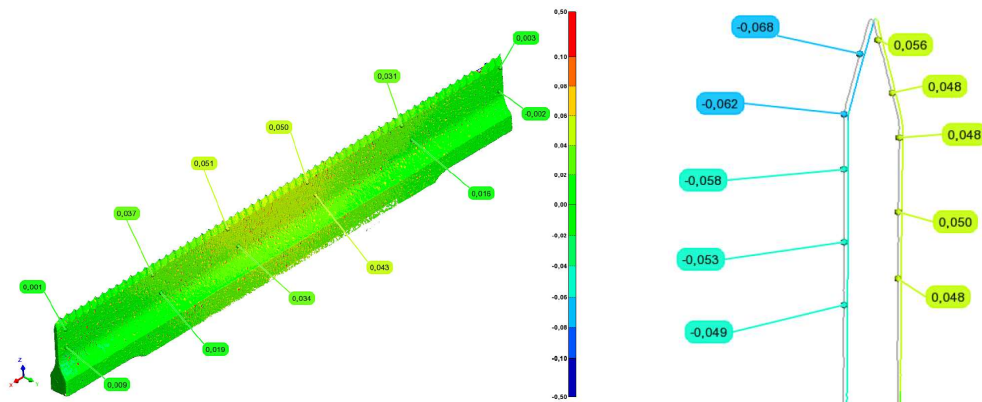


Figure 105: Laser Scansions

The measurements sampled in the 2D view shows the wear out of the component, by overlapping the profiles of the blade that were measured before starting the trial and after 1.25 million of cycles.

It can be noticed, as well, the impact of the deformation of the *Knife* in the top plane, that was highlighted by the 3D measurements, causes an apparent variation of the pitch of the teeth in the middle section.

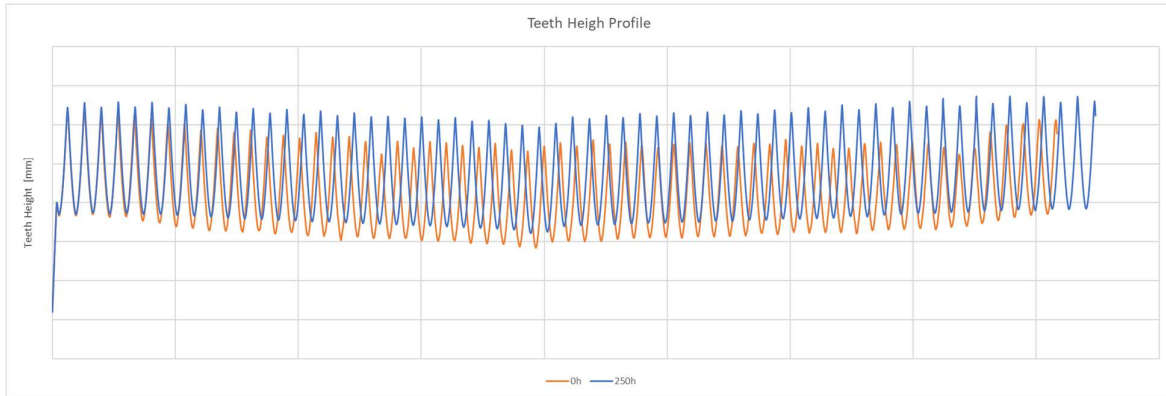


Figure 106: 2D Measure - Knife teeth profile

In order to complement the information about the wear trend of the *Knife*, an additional data was extracted from the 3D scansion, in order to provide an information about the volumetric removal of material.

For each tooth of the *Knife* it was defined an inspection volume (see Figure 107), that was mapped during each measurement, however the measurement was not considered reliable in presence of deformation of the blade, because the inspection volume was a space-fixed entity and it cannot match properly the deformed configuration of the teeth. This observation justifies the negative values reported in the box plot in Figure 108.

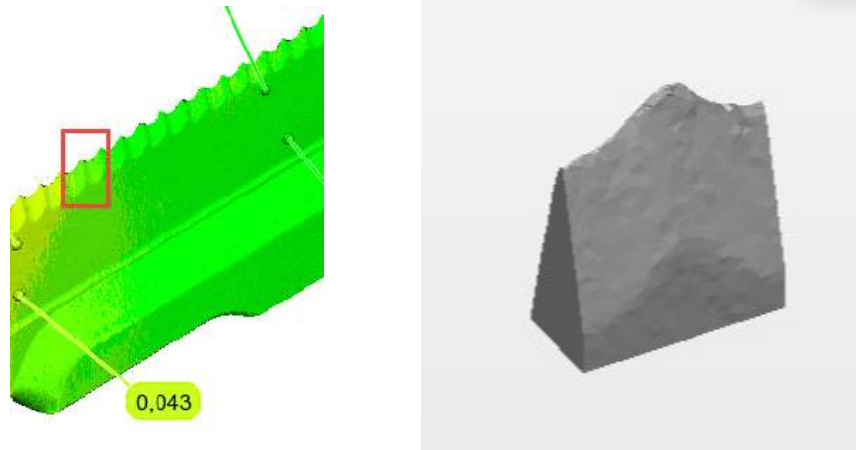


Figure 107: Tooth Inspection Volume

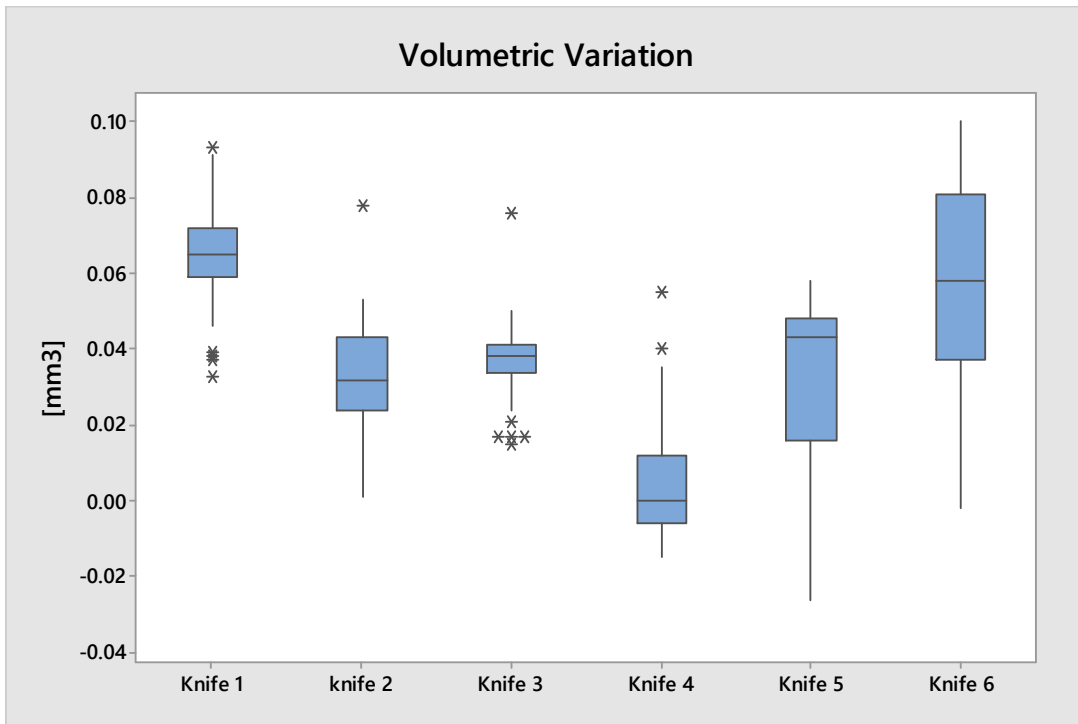


Figure 108: Tooth Volume Variation Distribution

7 Experimental Testing of Ball Bearings

This section focuses on the testing activities executed on the ball bearings installed on the *Transversal Links*.

The main purposes of the investigation were the selection of the proper component between two possible solutions produced by different manufacturers and the assessment of the reliability level for the expected lifetime of 3'000h. The manufactures were identified with the acronyms CW and SKF.

The ball bearings were designed by both suppliers for the specific application and according with their specifications the components would ensure a lifetime of 3'000h.

Previous experiences and the historical data concerning the behaviour of the ball bearing on the field raised the need of performing a dedicated testing campaign, since the real operative conditions of the *Filling Machines* are seldom properly replicated by the manufactures of the components.

The test was executed on a test rig specifically designed for the purpose, whose configuration aimed to reproduce the stresses applied on the bearing, reducing the complexity of the interfaces and the effort required for running the trial.

The test set up was defined referring to the results achieved by the virtual simulation and the measurements of the loading cycle in the real operative conditions.

7.1 Test Rig

The test rig (Figure 109) was designed with the intention of reproducing the main stresses applied on the bearing, minimizing the effort and the supervision from the operators for running the trial and reducing the testing duration.

The specimens are installed in 12 testing stations, each one carry only one ball bearing. The stations are connected to a pneumatic actuator, that is used for recreating the loading cycle of the bearing.

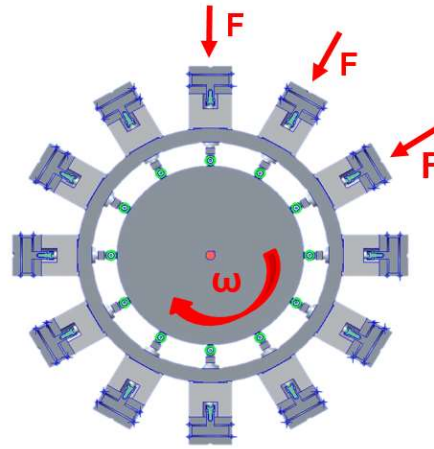


Figure 109: Test Rig

The testing stations (Figure 110) are radially displaced in reference to a central disk that is made in the same material used for the cams used in the *Jaw System* and it was manufactured according with the same process, including finishing and thermal treatment, in order to replicate the correct tribological pair.

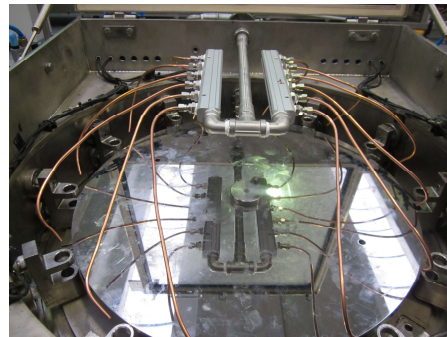
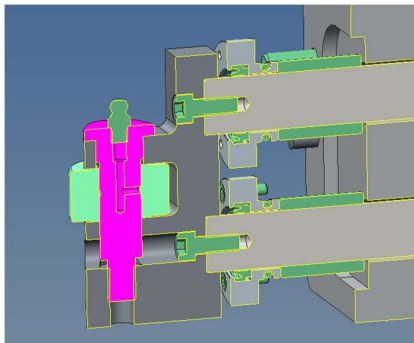


Figure 110: Testing Station detail (left) and water supplying circuit (right)

The test was executed in a conditioned chamber with the presence of a high content of humidity and liquid water, and detergents that are usually adopted during the automatic cleaning of the *Filling Machine*. The need of emulating the environmental conditions was related to the output of failure analysis executed on the ball bearing damaged on the field, which shown that the environmental stresses are critical for the lifetime of the seals, that are not able to retain the internal grease when they are aged and compromise the lifetime of the bearings.

The loading profile (Figure 111) was obtained from the curves calculated with the virtual model, shortening the overall duration by suppressing the phases of the cycle without the application of the load:

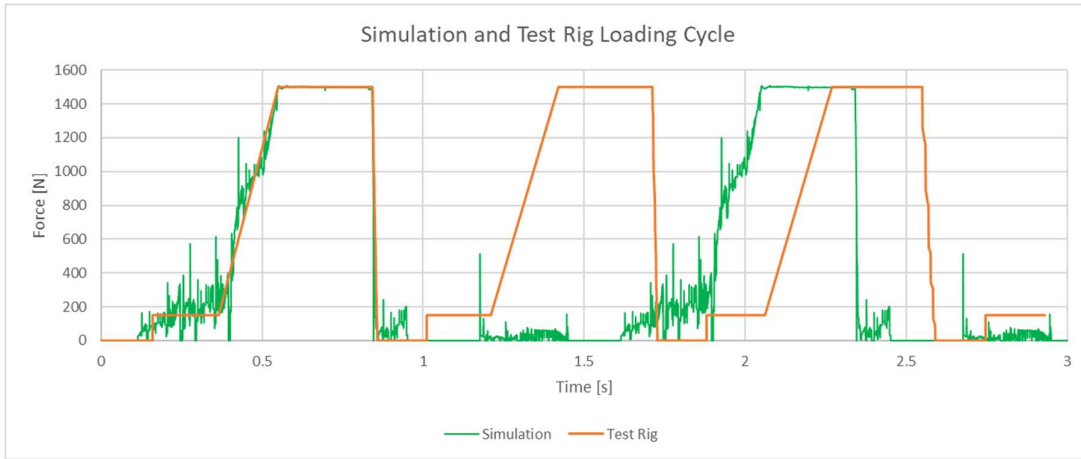


Figure 111: Loading Cycle in the operative application and in the test rig

Since the highest load was applied on the bearing when moving along a planar surface, whilst in the test rig the contact is always between curved surfaces, the pressure distribution was calculated in the two types of contacts, but there was not a relevant difference due to the wide curvature of the disk in the test rig, thus the nominal load was kept for the loading profile of the test (see Figure 112).

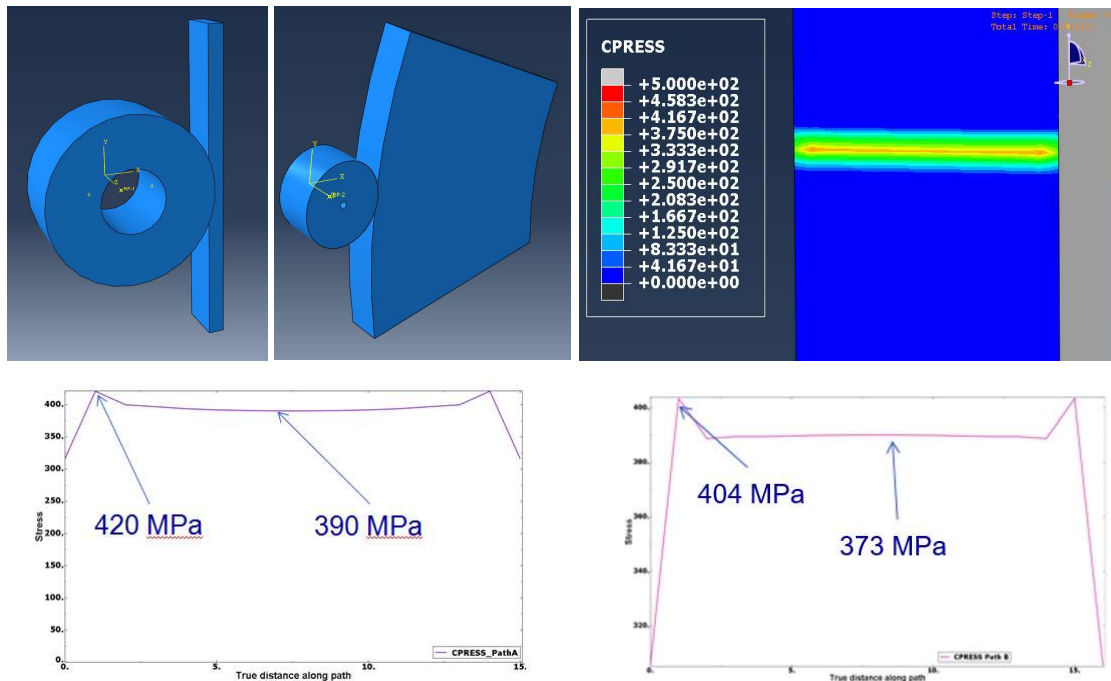


Figure 112: Contact Pressure Distribution in the Test rig (left) and in the standard application (right)

Parameter	Value
Loading Cycle	
Cycle Duration	1s
Lower Force	150 N
Higher Force	1'500 N
Cam Tangential Speed	1.23 m/s
Chamber Temperature	50 °C
Water Spraying	
Flow rate	3 l/min
Frequency	1 spray/3s
Duration	1 s
Cleaning Cycle	
Frequency	6h
Duration	1 min
Rinsing Duration	1.5 min
Agent	P3 Topax 12, Ecolab - (@3% _(w/w))

Table 12: Test Set-Up

7.2 Results

The specimens were tested for 7.2 million of loading cycles, which correspond to the target lifetime of the ball bearing installed in a *Jaw System* that operates at the production rate of 24'000 packages/hour for 3'000h.

Since the consolidated causes of failures detected for the ball bearings on the field were often related to the degradation of the lubricant, for two specimens it was planned a periodical lubrication during the measurement stops.

The integrity of the specimens was monitored by position sensors installed on the rod of the pneumatic actuators: the sudden variation of the position represented the breakage of the ball bearing, and in the majority of the cases displacement in the range of 0.3-0.5mm in a time frame of 30s were sufficient for stating the failure of the component. In the case of sudden displacement, the testing station was moved back for separating the bearing from the cam and preserving the integrity of the testing equipment. The confirmation of the failure was stated by the operator [25].

In order to monitor the status of the specimens, periodical acquisition of the vibration signal of the bearing were scheduled each 100 running hours, the selected sampling frequency was 10 kHz. Due to the constant speed of the cam adopted during both the test and the measurement operations, the vibrations signals have been then analysed calculating the:

- RMS

- Kurtosis
- Characteristic Frequencies of the ball bearing

The RMS and the Kurtosis of the signal are the statistical parameters mostly investigated for the fault detection, and the analysis in the frequency domain of the characteristic frequencies of the ball bearings, since they are a representation of the average overall energy content of the signal and of the presence of impulsive events, that shift the dataset away from a normal distribution [18], [19].

The manufactures of the ball bearing declared the characteristic frequencies of the components, that usually are could be associated to damages located in specific parts of the component.

The characteristic frequencies are function of the rotation speed of the shaft (f_r) and are defined by geometrical properties of the component, the internal diameter (D) of the outer race, the externa diameter of the inner race (d), the number of spheres (n) adopted and the contact angle (φ) [20], [24]. The analytical definition of the frequencies is:

Ballpass frequency, outer race:	$BPFO = \frac{nf_r}{2} \left(1 - \frac{d}{D} \cos\varphi \right)$
Ballpass frequency, inner race:	$BPFI = \frac{nf_r}{2} \left(1 + \frac{d}{D} \cos\varphi \right)$
Fundamental train frequency (cage speed):	$FTF = \frac{f_r}{2} \left(1 - \frac{d}{D} \cos\varphi \right)$
Ball (roller) spin frequency:	$BSF = \frac{D}{2d} \left[1 - \left(\frac{d}{D} \cos\varphi \right)^2 \right]$

Table 13: Ball Bearing Characteristic Frequencies

The manufactured of the ball bearing declared the values of their components, hence those were used for monitoring the integrity of the specimens.

Mode	SKF	CW
BPFO	27.30 Hz	25.44 Hz
BPFI	43.87 Hz	41.24 Hz
BSF	36.6 Hz	33.2 Hz

Due to the layout of the test rig it was not possible have sensor on board for the entire duration of the run, hence each 200h working hours an accelerometer has been mounted on the shaft

carrying the specimens and oriented as in the Figure 113. During the measurements only the station equipped with the accelerometer has been activated, in order to reduce the noises of the signals.

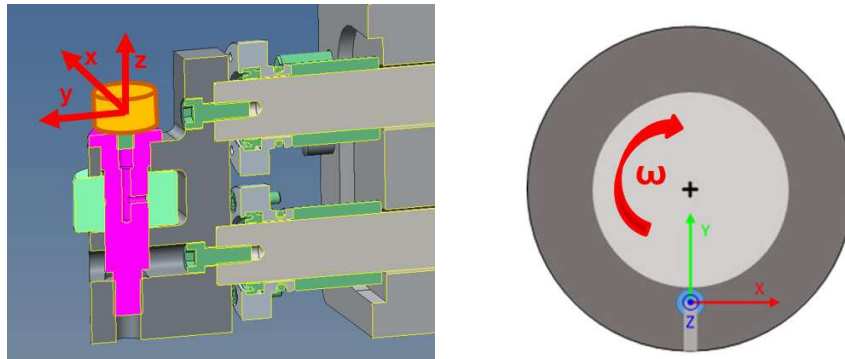


Figure 113: Installation position of the triaxial accelerometer

Even if the time between two measurements was almost long, it was sufficient for detecting variation of the spectrum of the signal.

The graphics in Figures 114-120 show the evolution of the vibration spectra for the different measurement intervals of some failed specimens (Bearing #9 and #11) and of some survived components.

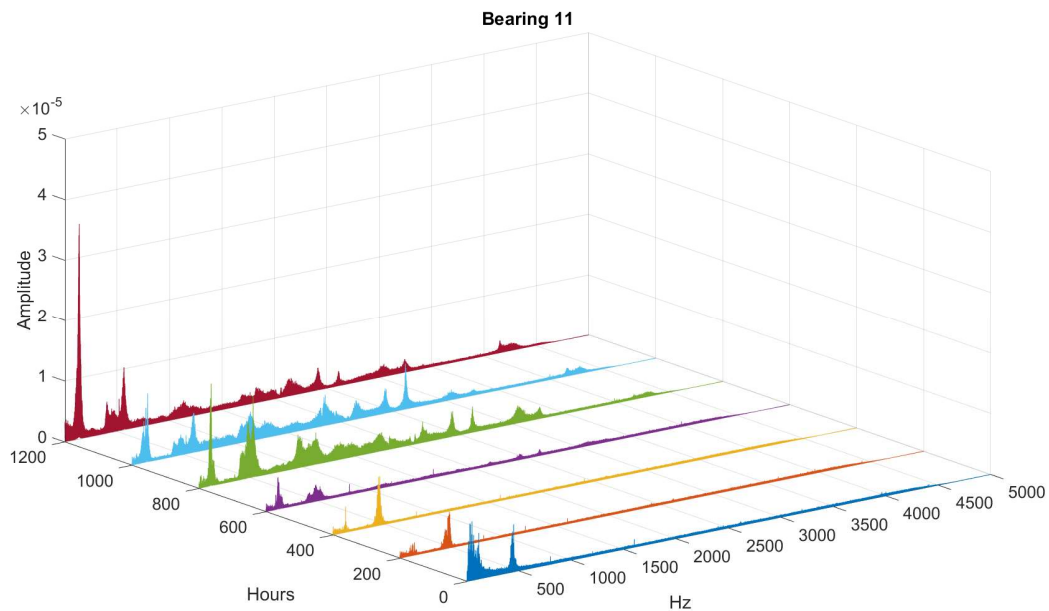


Figure 114: Vibration Spectrum of the Specimen 11 at different testing stages

The analysis of the variation of the spectrum of the Bearing 11 (Figure 114) showed that the since 800h some damages occurred on the out race and later on determined the damage of the

spheres. The comparison of the variation of the signal from the beginning of the test and the last check before the failure shows a generalized damage (Figure 115), likely evidence of wear and lack of lubrication, and the most intense amplitude was related to the highest harmonics of the BPFO.

The visual inspection of the ball bearing showed that the damage was correlated to the degradation of the lubricant and to the evolution of corrosive phenomenon in the component.

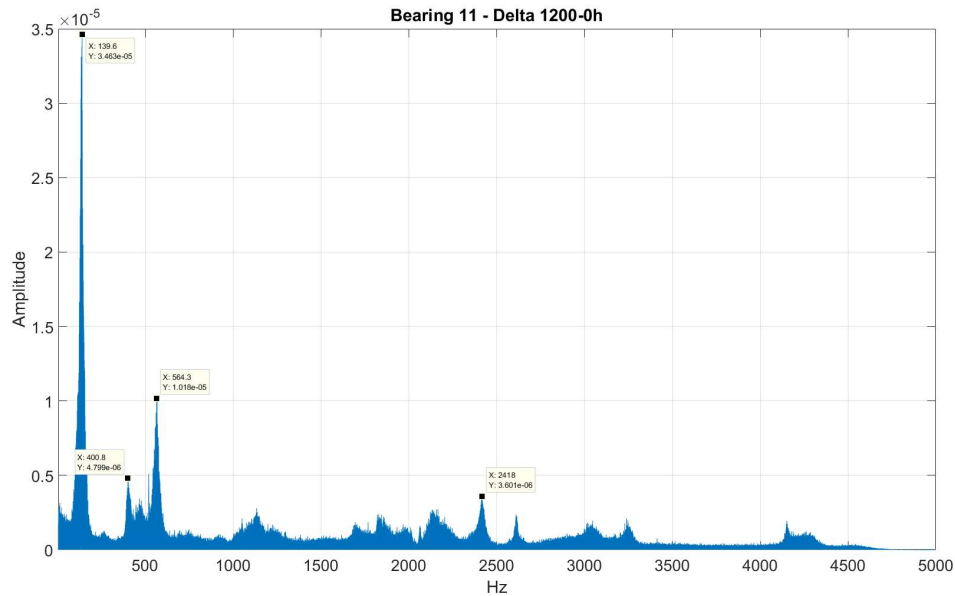


Figure 115: Vibration spectrum of the Specimen #11 after 1'200h

A comparable behaviour was noticed in the curves sampled on the Bearing 9 (Figure 116), where the failure occurred for a longer operative life. Approaching the end of the test the spectrum is characterized by a generalized enhancement of the energy content, but the frequency with the highest magnitude are the one correlated to the BPFO (Figure 117).

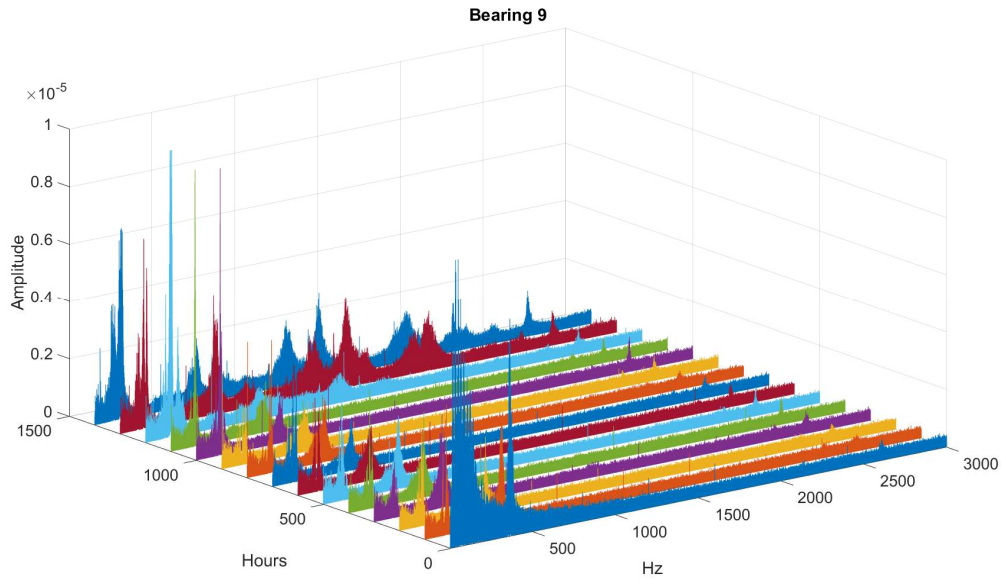


Figure 116: Vibration Spectrum of the Bearing 9

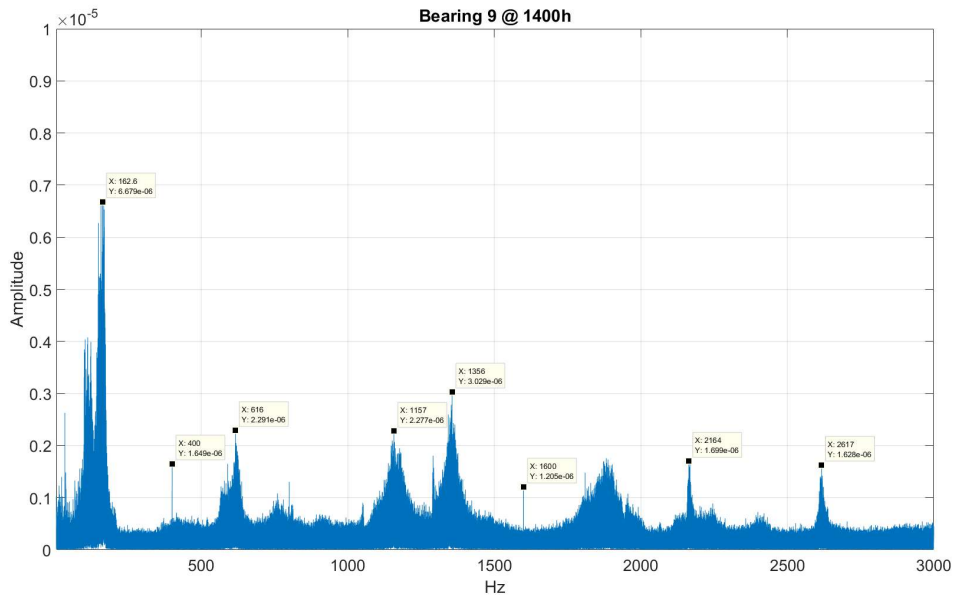


Figure 117: Vibration Spectrum of the Bearing 9 at 1'400h

The peak of the amplitude was noticed at the frequencies of 162.5 Hz, which should likely correspond to the 6th harmonic of the BPFI, whose theoretical value is 163.8 Hz, and 1356 Hz which should likely correspond to the 31st harmonic of the BPFO, whose theoretical value is 1359.97 Hz the difference between the theoretical and the real measured frequency would be

related to the speed control of the driving motor of the cam. The ball bearing failed 300h after the detection due to the breakage of the outer race of the bearing.

The generalized enhancing of the intensity of the vibrational spectrum was noticed also on the specimens that did not fail during the test, and the analysis of the FFTs showed that even in those ball bearing the principle of damage was starting from the outer race (Figures 118 and 119).

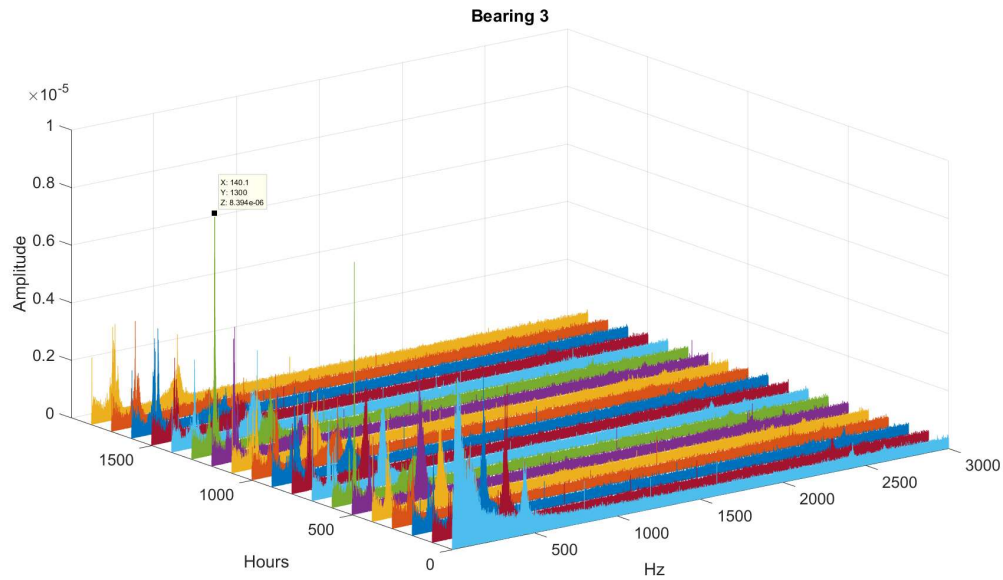


Figure 118: Vibration Spectrum of the Bearing 3

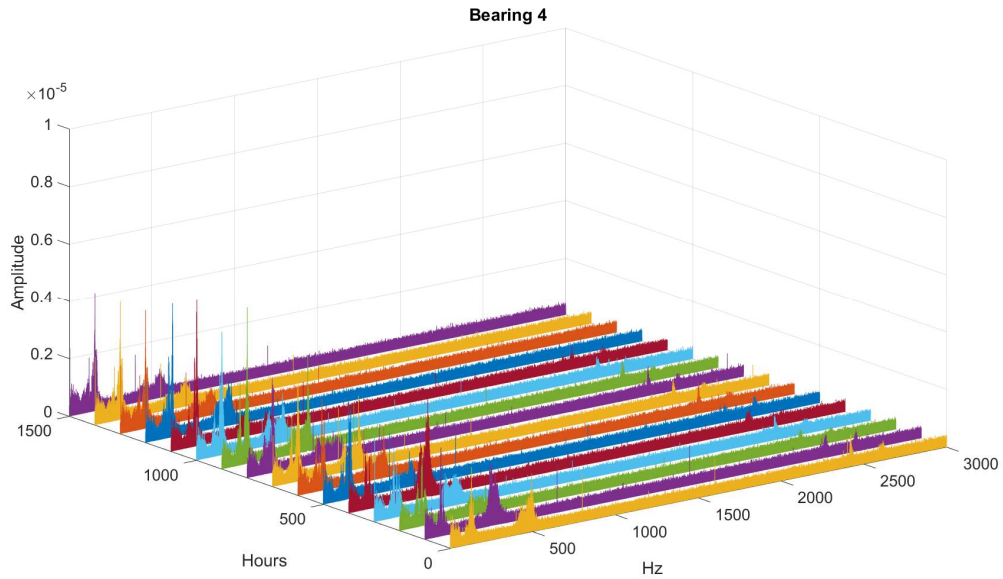


Figure 119: Vibration Spectrum of the Bearing 4

The specimens Bearing #2 and #8 were periodically re-lubricated during the measurement stops, they survived to the test and the evolution of their FFT curves (Figure 120) showed a smoother variation of the spectrum, confirming the sensitivity of the components to the efficiency of the lubrication.

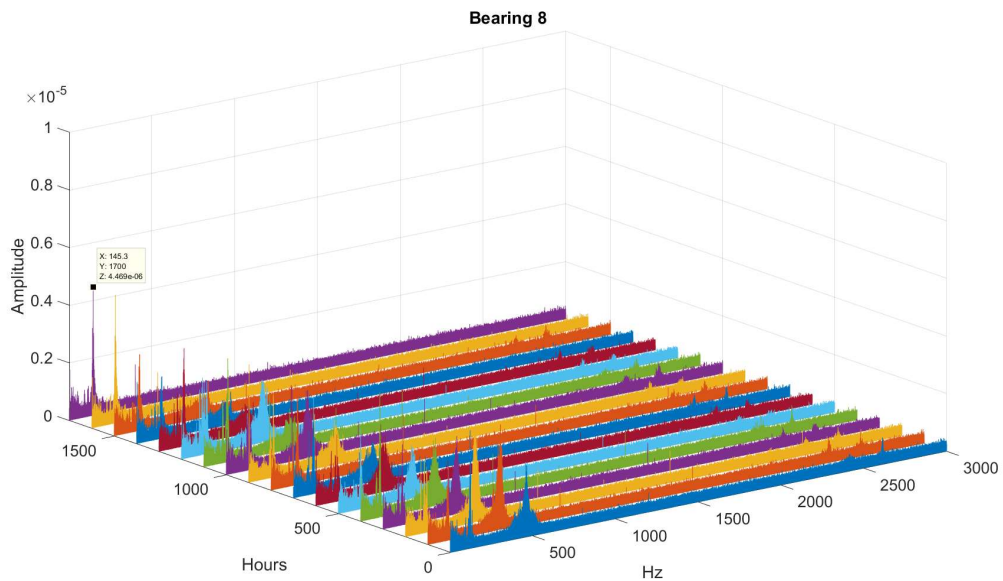


Figure 120: Vibration Spectrum of the Bearing 8

The analysis of the trends of the RMS (Figure 121) and the Kurtosis (Figure 122), showed that the failure of the Bearing #9 and #11 was associated to the growth of both predictors:

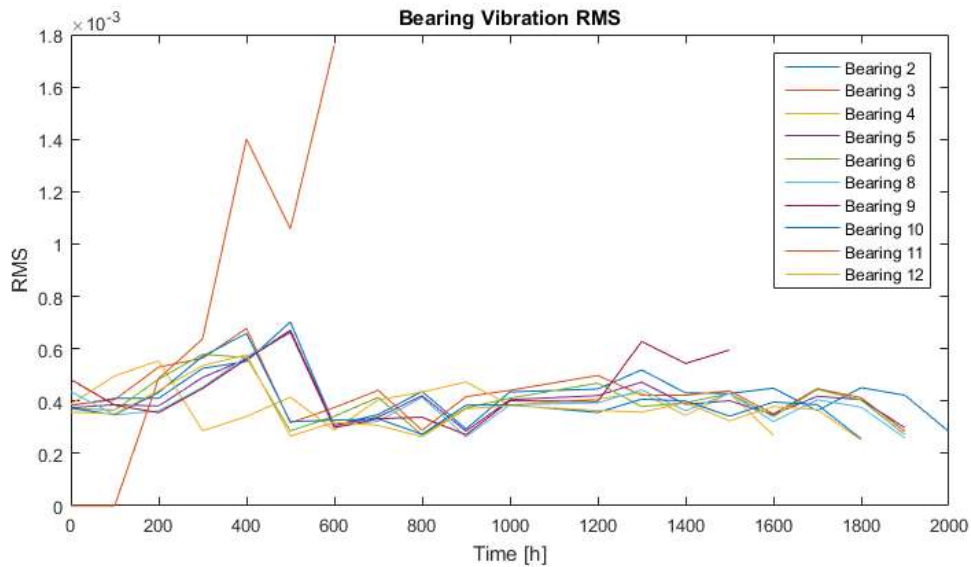


Figure 121: RMS Trend

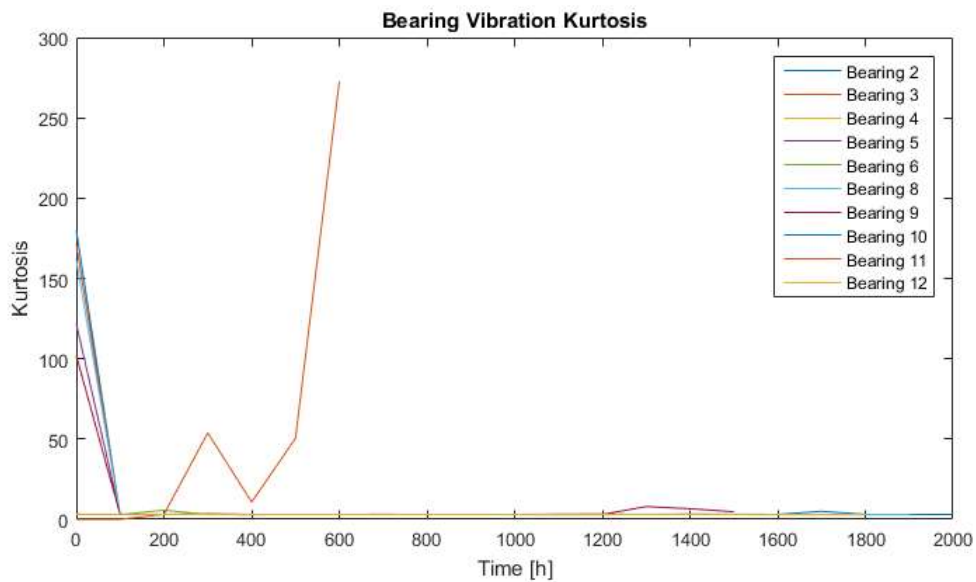


Figure 122: Kurtosis Trend

The main failure mode detected during the test was the breakage of the out race and in many cases evidence of corrosion were detected on the internal component of the bearings (Figures 123-125).

The specimens that passed the test without the breakage showed during the visual inspection relevant backlash between the internal and external races and the typical coloration of rust surrounding the seals.



Figure 123: Test Rig damaged bearing



Figure 124: Test Rig damaged bearing

The analysis of the failure time data of the specimens showed that both the Weibull and Lognormal probability functions provide a good description of the failure rate of the specimens, even if in the case of the SKF the dataset is disposed as two different types of failure modes compete to the damage of the ball bearing, a deeper understanding might be achieved by analysing the internal components of the bearing. The model selected for the lifetime analysis was the Weibull function, since it predicted lower lifetimes, which was a conservative estimation from the machine availability perspective.

The version of ball bearing CW demonstrated the best performances and a higher reliability at the target lifetime (Figure 126).

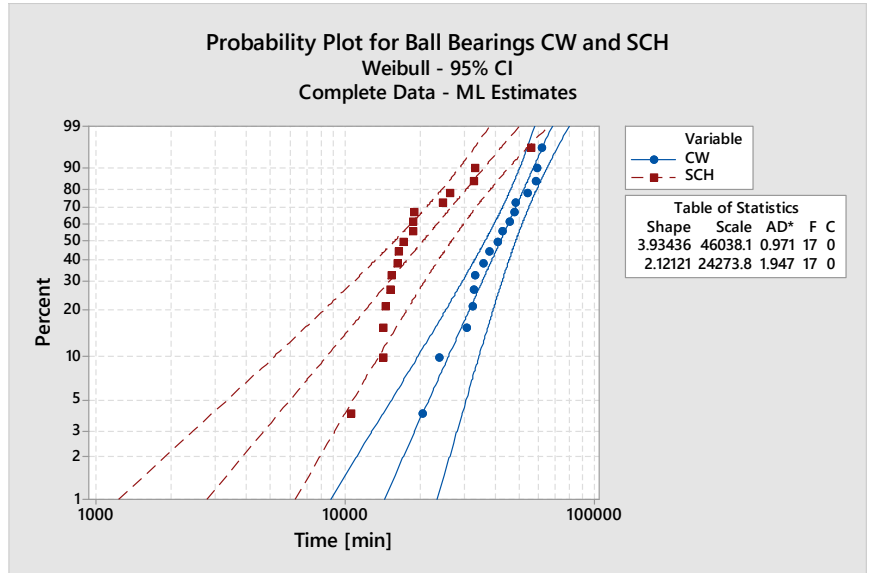


Figure 125: Failure Distributions of CW and SCH samples

8 Vibration Data Analysis

This section focuses on the method adopted for increasing the reliability of the *Jaw System* by correlating information and data collected at different steps of the development process.

In the early stage, the design is always supported by the FMECA (Failure Modes Effects and Criticality Analysis), that is a structured method for identifying the potential failure modes, correlating them with the possible causes and estimate both the likelihood of the occurrence, the magnitude of the consequences and the detectability [27].

The analysis was carried out on the results provided by the virtual models and technician's experience. On the bases of the FMECA outputs, the risk of facing failures is managed acting either at the design or at the operational level, such as defining the maintenance strategy.

The FMECA evaluation, should be then confirmed, updated and integrated with the data from the field, for tuning the both the technical solutions and the mitigation actions adopted.

The results of the conjunct examination of FMECA and field data was crosschecked with the technical details of the design of the *Jaw System*, for identifying the critical components and investigating more accurate monitoring method for detecting and predicting the failure.

The analysis of the vibrations generated by the *Jaw System* during the standard production could provide information about the status of the equipment.

In order to properly understand the vibration signals provided by the subsystem it is crucial to cover the following steps:

- Identification of all events that can activate the dynamic response of the frame, the components that are involved in the event and the potential failures that can activate.
- Correlate those events with specific features of the vibrational signals
- Identify the correct estimators that can describe the evolution of the status of the component competing to the creation of the excitation
- Identify the thresholds that would represent the degradation of the functionality of the components or subsystems and the incipient failure

The achievement of the information required in the steps described above started from the analysis dynamic response of the *Jaw System*, provided by the model described in the first section of this work.

Once that a virtual model built on the key events that characterize the operating cycle of the *Jaw System* was defined, it was correlated with the vibrations signals provided by a test rig, that was a simplified unit operating without the presence of packaging material.

The further step was the comparison of the signal provided by the test rig and the one collected in a complete *Filling Machine*, which was indispensable for extending the usage of the virtual model to the equipment on the field.

The last phase of the process was the identification of the signals generated by a damaged device, this stage was covered again on the test rig, due to practical limitations in using damaged components in a full operating *Filling Machine*.

8.1 Maintenance Strategies

The quality of a mechanical device is often evaluated through its availability, that is intended as the ability of the system to perform its function under stated condition for a stated period of time.

In order to achieve the availability target, both the reliability and the maintainability of the system should be optimized.

The reliability represents the probability that the system is properly operating at a specific time, with a defined confidence level; it is experimentally evaluated, by means of tests that correlate the lifetime distributions of the components and the mechanisms, with the type and the magnitude of the stresses that the equipment is subjected to during the operative life.

The maintainability is defined as the probability of performing a successful repair action within a given time. In other words, maintainability measures the ease and speed with which a system can be restored to operational status after a failure occurs.

The maintenance strategies are defined balancing the availability requirements with the cost and the risks associated to the operations defined during the FMECA. The most common maintenance strategies are three:

➤ *Maintenance at the Event:*

the equipment is operated until a failure occurs inhibiting the functionality of the system.

➤ *Preventive Maintenance:*

The components of the equipment are replaced at specific times, before their damage.

The maintenance interval is based on the evaluations of reliability and maintainability

➤ *Predictive Maintenance:*

the equipment is maintained on the base of its actual status, evaluating signals and parameters that describe the integrity of the system.

Moving from the Maintenance at the Event to the Predictive Maintenance, the availability of the system significantly increases, as well as the complexity and the manufacturing cost of the equipment, whilst the maintenance cost is reduced, since the component are run until the incipient failure, instead of being early replaced on the base of statistical evaluations of their lifetime.

The Predictive Maintenance anchors its effectiveness on: the quality of the signals, the robustness of the predictors identified for describing the status of the system, the robustness of the predicting models that connecting the degradation of the system the remaining useful life activates the maintenance tasks.

In the last decade was characterized by a rapid transition to the transition the Predictive maintenance Approach, due to the fast evolution of the technology, the rapid growing of calculation power, the development of neural networks, development of more robust sensors, able to withstand to the operational stresses for longer time, etc.

The degradation of a system could be monitored by several types of sensors, whose measuring principle might be based on different physical parameters.

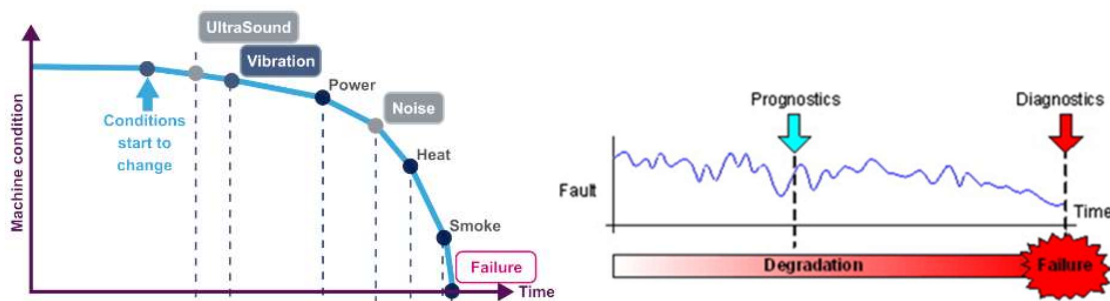


Figure 126: Prognostic and Diagnosis of Failures

However, creating the predictive models and setting the correct thresholds is the biggest challenge for this method. In this section is described a first attempt of correlating the vibration signals provided by the *Jaw System* with the operational phases of the mechanism in the time domain [23].

8.2 Filling Machine Equipment

The *Filling Machine* is already equipped with a dedicated structure (Industrial PC, Data Logger, Fieldbus Network) for monitoring the status of some specific sub-system and functions during critical operational phases of the process [21], [22].

The data is firstly analysed onboard, for screening corrupted or empty files, performing the diagnosis of the sensors, evaluating major deviation for activating the alarms. The data is then stored in a cloud and processed; then post processing reports are distributed.

The accessibility to the components installed in the *Jaw System* is dramatically low, since the majority of the maintained component are installed on the Chains, that cannot be reached by wired sensors, and also because of mechanical constrains, that reduces the availability of space for installing the sensors to narrow windows.

Basing on those limitations, the way that in the past was selected for investigating the status of the *Jaw System* was through three monoaxial piezo-accelerometers installed on the frame: two are in the front, oriented along the horizontal direction and one on the side, parallel to the horizontal plane and normal to the sensing direction of the others (Figure 127).

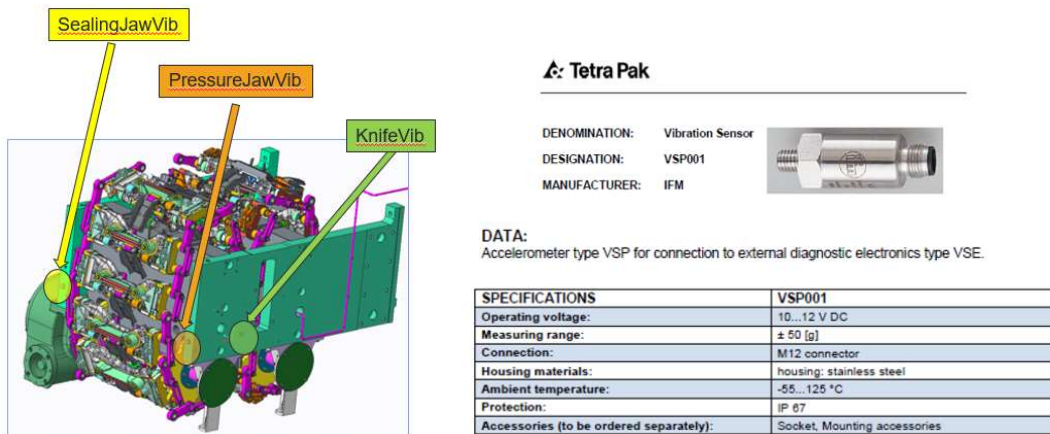


Figure 127: Positioning of the accelerometers (left) and datasheet details (right)

8.3 FMECA and Field Data

The FMECA analysis highlighted 12 major failure modes (Table 14) that can inhibit the main function of the system and 27 possible causes that activate one or more of those failure modes (Figures 128 and 129).

The *Jaw System* consists in many similar subsystems (e.g. transversal links), hence the probability of failure of the equipment is dramatically increase by the amount of systems competing to the overall functioning of the equipment.

The most critical parts that were identified by cross-checking the FMECA and the Field Data were:

Component	Failure Modes
Ball bearings	1. Breakage 2. Seizure
Volume Flaps	1. Breakage
Cams	1. Wear 2. Corrosion
Knives	1. Breakage 2. Bluntness
Inductors	1. Wear 2. Corrosion 3. Breakage

Table 14: Failure Modes List



Figure 128: Failures: Volume Flap (left) and Ball Bearing (right)

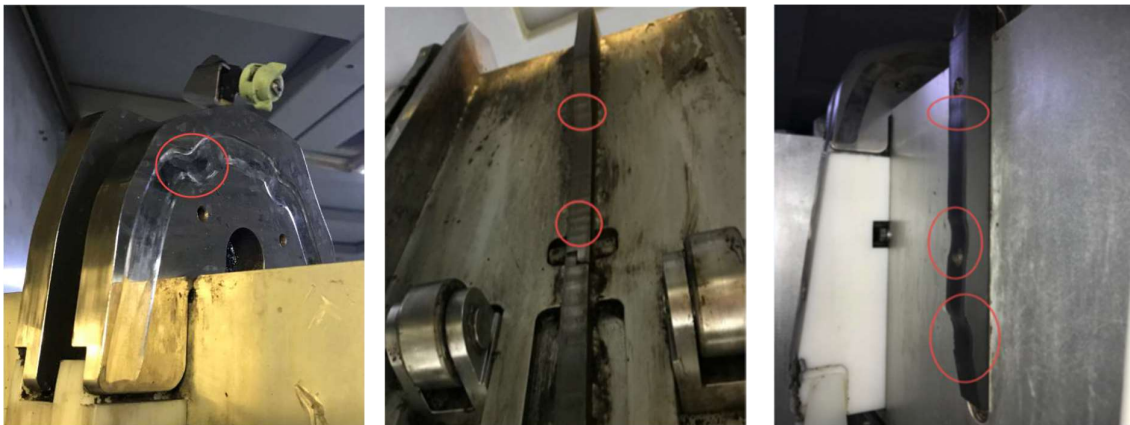


Figure 129: Failures: Main Cam (left), Volume Cam (middle and right)

8.4 Virtual Model

The virtual model of the system was used for identifying all the critical phases of the Chain cycle that can generate either unexpected stresses on the mechanisms and components, or impulses and vibrations of the frame.

A curve abscissa R was defined along the trajectory of the transversal link and normalized on the length, in order to have it varying in the range [0;1] (Figure 130).

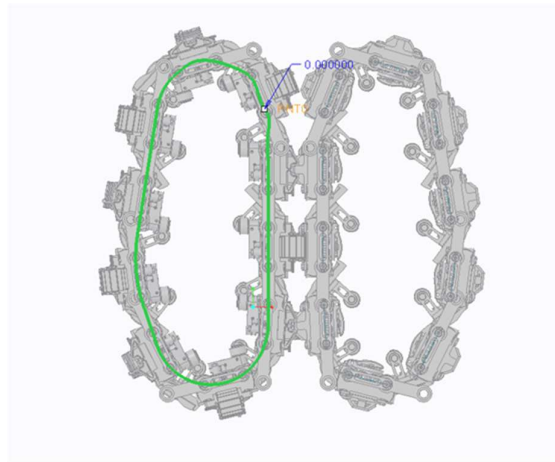


Figure 130: Ball Bearing Trajectory and R Abscissa

The transient phases, the potential hurts, the contacts with the cams and the possible hurts between the components of the *Jaw System* have been mapped and correlated to the abscissa R (Figures 131-133).

Since the Chain is composed by 10 transversal links, the position of each link is always known by adding 0.1 to the position of the previous link.

R Value	Event
0	<i>Contact with the packaging material tube</i>
0.030	<i>Contact Volume Box bearing and Volume cam</i>
0.035	<i>Contact Folding Flaps bearing and Cam</i>
0.050	<i>In-movement ready</i>
0.060	<i>Start Design Correction</i>
0.068	<i>Start Sealing pulse</i>
0.075	<i>End Jaw Pressure application</i>
0.085	<i>End Design correction</i>
0.093	<i>Folding Flaps closed</i>
0.104	<i>Volume Flaps parallel</i>
0.130	<i>End Folding Flaps completely closed</i>
0.148	<i>Folding Flaps opened in MID position</i>
0.205	<i>Discontinuity between Volume box and Cam in the Pressure Jaw Chain</i>

0.220	<i>Discontinuity between Volume box and Cam in the Sealing Jaw Chain</i>
0.226	<i>Folding Flaps completely open</i>
0.245	<i>Start cutting</i>
0.263	<i>Maximum Knife stroke</i>
0.275	<i>Knife back</i>
0.280	<i>Start Jaw Pressure release</i>
0.290	<i>Jaw Pressure release</i>
0.375	<i>Rig Inductive Sensor</i>
0.695	<i>Contact between Link and the Tensioner</i>
0.729	<i>Contact between the Side Roller and the Cam</i>

Table 15: List of Relevant Events

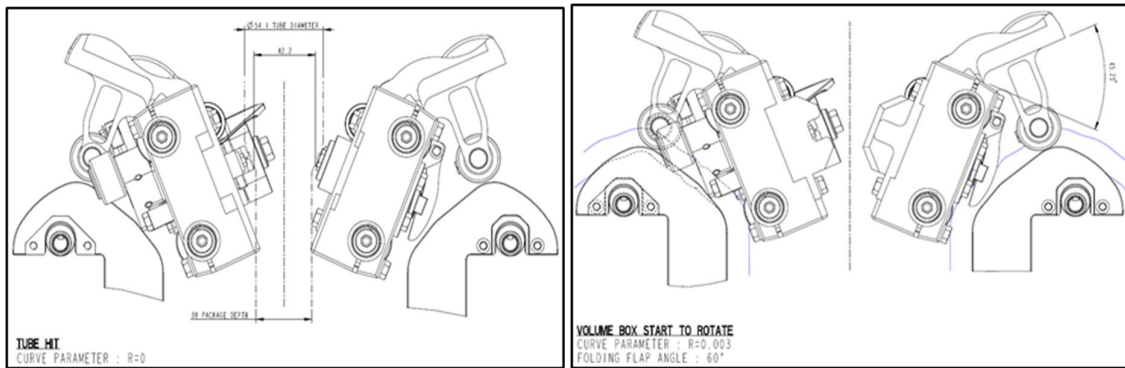


Figure 131: Tube Hit (left), Contact Volume Cam and Ball Bearing (right)

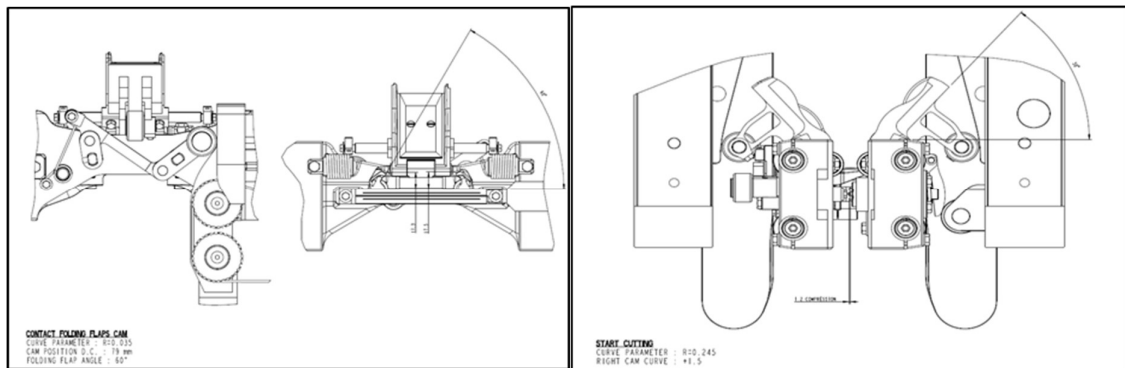


Figure 132: Contact Folding Flap and Cam (left), Cutting Phase (right)

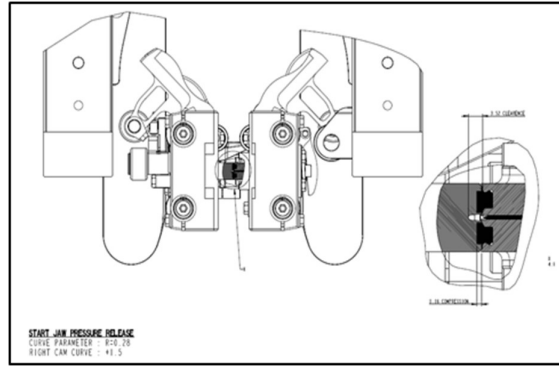


Figure 133: Release of the pressure between the Transversal Links of the Pressure and Sealing Chains

8.5 Vibration Data: Test Rig

The measuring campaign of the vibration data was executed on the test rig, since it was adaptable to the modifications required in the different trials and easier to manage. The test rig is a simplification of the *Filling Machine*, that operates without the packaging material and product, hence it can run also without some on the mechanisms installed in the *Jaw System* [26].

The frame was the same than the standard *Filling Machine*, as well as the accelerometers, which were installed in standard position, in order to exactly emulate the real configuration.

The position of the *Chains* was monitored by means of two independent sensors: an encoder that was installed on the shaft of the *Wheel* and an inductive sensor that reads the passage of one specific *Transversal Link* each complete rotation of the *Pressure Chain* (Figure 134).

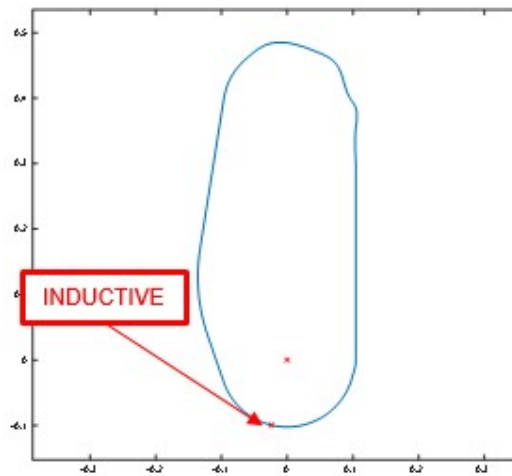
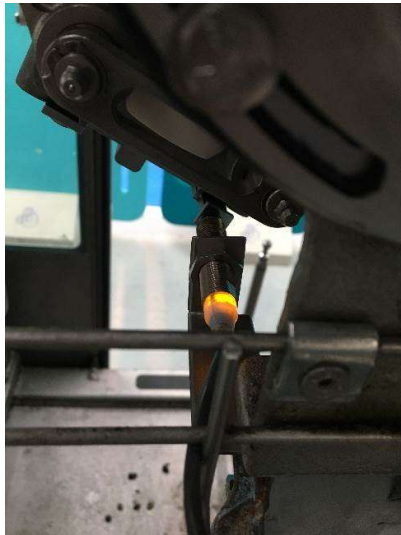


Figure 134: Inductor Sensor Positioning

The sensors were used in parallel because the encoder provides a more accurate positioning of the *Chain*, that is indispensable for the trials, whilst the inductive sensor is already available in all *Filling Machine*, hence its presence is required for understanding if the accuracy of its data is sufficient for the purposes of the monitoring.

The inductive sensor provides a feedback a square wave, whose width depends on the sensitivity versus the metallic element that is moving in front of the sensor. The Figure 135 represents a vibration signal and the inductive one, the red bandwidth represents the region where a specific event might belong, according a with a model phased with the inducive signal, the risk is related to the capability of identified that specific event instead of another one happening in a close timeframe.

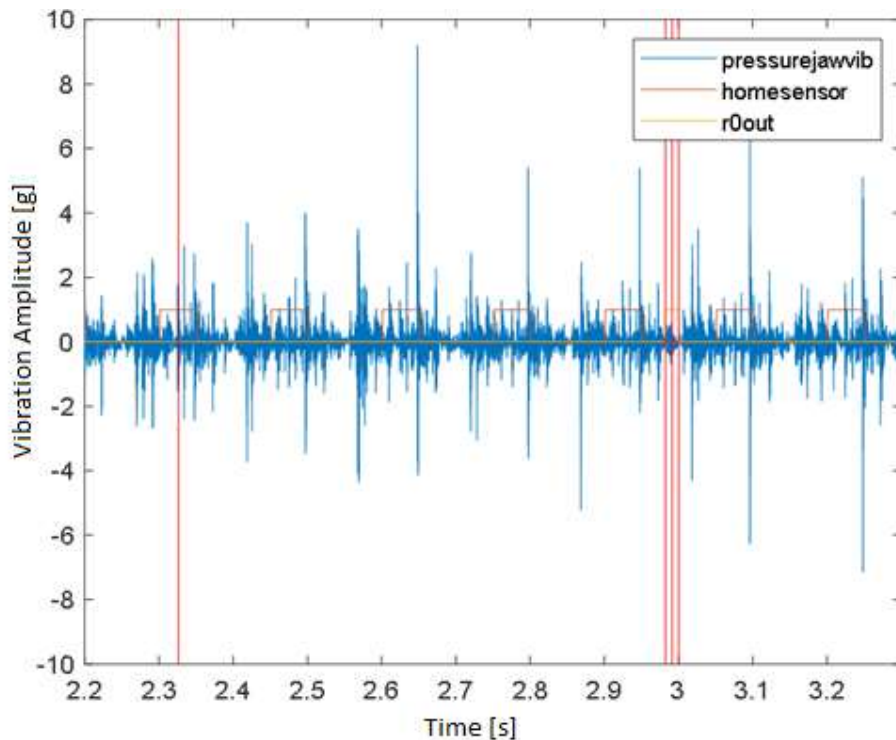


Figure 135: Jaw System Vibration Signal

The test rig was equipped with the same Beckhoff CPU that is available on the standard equipment for measuring the vibrational data, which was collected at the sampling rate of 20 kHz.

The events listed in the Table 15 refer to one single *Transversal Link*, hence the complete cycle of the *Chain* is obtained by overlapping in the space domain this sequence of events of each *Transversal Link*, which are shifted of one pitch, corresponding to the 10% of the overall R abscissa This operation highlights that many events of different transversal links happen in

very tight time frame, thus the association of the peaks of the vibration signals with the correct event might be affected by errors.

The results obtained by the dynamic model, showed that the linear speed of the *Transversal Links* is characterized by some fluctuations (Figure 136), which should be considered when passing from the space to the time domain and phasing the virtual model (space defined) with the vibrational data (time defined).

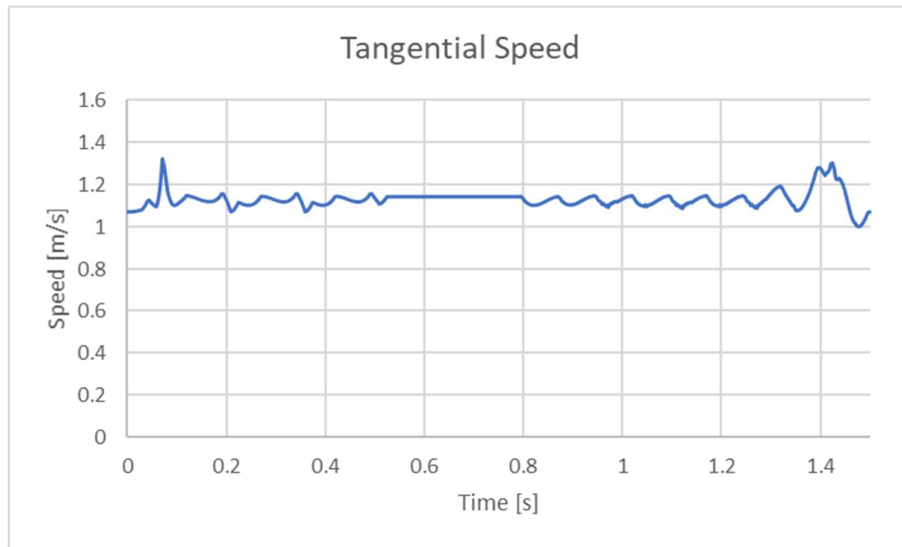


Figure 136: Transversal Link calculated Velocity

The accurate normalization of the signal in the time scale was obtained as well by using the data provided by the encoder.

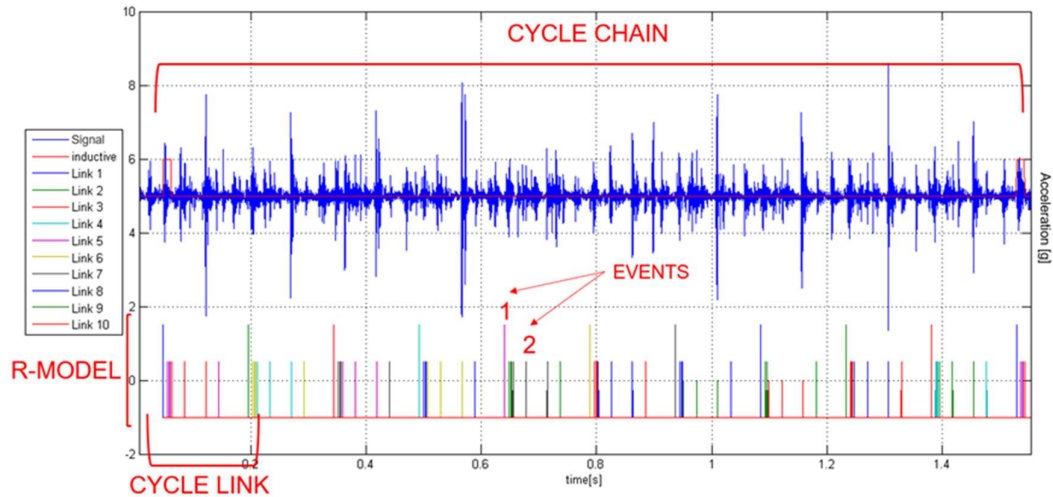


Figure 137: Vibration Signal and Events in the time domain

The graphic in the Figure 138 shows the overlapping of the vibrational signal and the sequence of events. The high number of potential events that can influence the vibrational spectrum, required a step incremental approach, that by the inhibition of some stressors would simplify the identification the correlation of the peaks of the vibration signals [16].

The linearization hypothesis of the superposition of the effects was considered a sufficient approximation of the reality.

The sequence of the runs was:

1. Standard Configuration-in: Leaving all the components to their place.
2. No Folding Flaps: Removing the Chains and the Folding Flaps
3. No Pressure springs and spacers: Removing pressure springs and spacers.
4. No Side Rollers: Removing the bearings.
5. No Volume Box: Removing the Volume Boxes
6. No Cutting: Removing the cutting components.

Among this sequence of tests, the ones that provided more useful results were the Test 5 and the Test 6.

The test without the presence of some *Volume Boxes* in some *Transversal Links*, highlighted the presence of an impulsive event in correspondence to the change of the curvature of the *Volume Cam* (blue circle) and one when passing in front of the discontinuity of the two elements of that cam (green circle) as shown by the spike detected in the dynamic model (Figure 138 and 139).

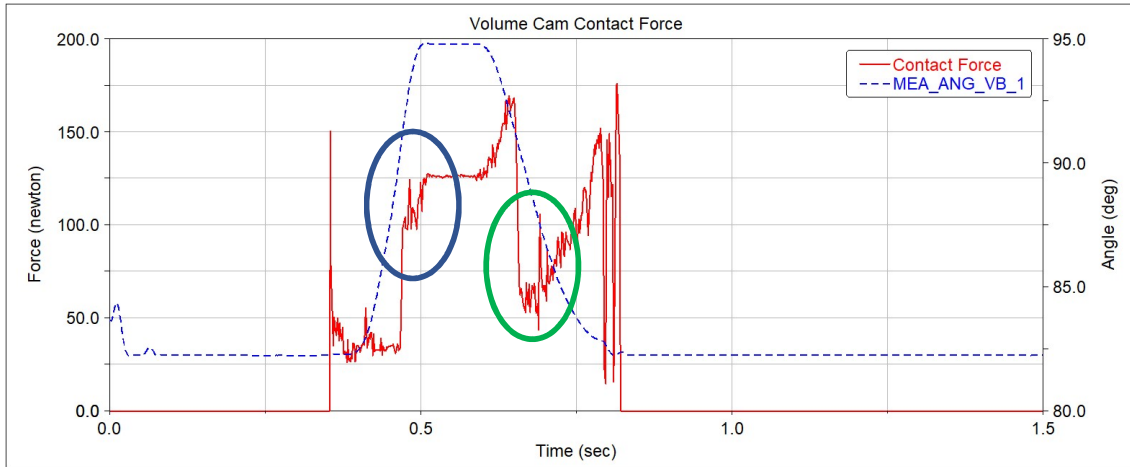


Figure 138: Volume Cam calculated Contact Force

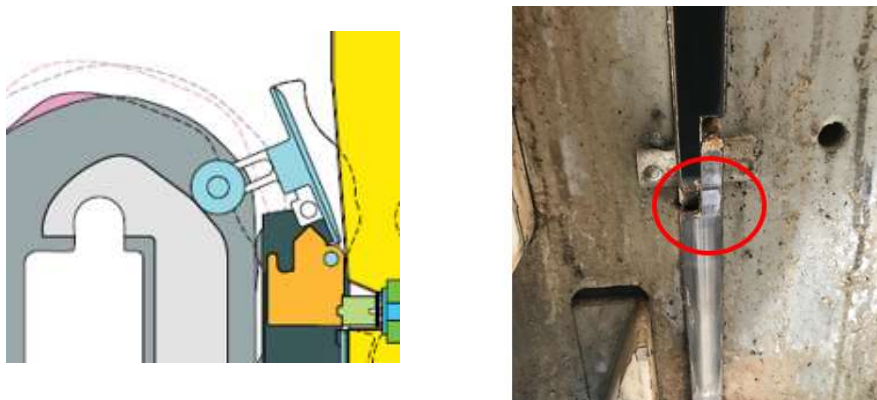


Figure 139: Volume Cam discontinuities

The Figure 140 shows the effect of the discontinuities of the *Volume Cam* produced in the vibration signals: comparing the vibration trends of the Test 1 (Standard Configuration) and the Test 5 (Without some *Volume Boxes*), it is possible to highlight the absence of the *Volume Boxes* determine the absence of vibrational peaks in some sections of the *Transversal Link* path (red squares).

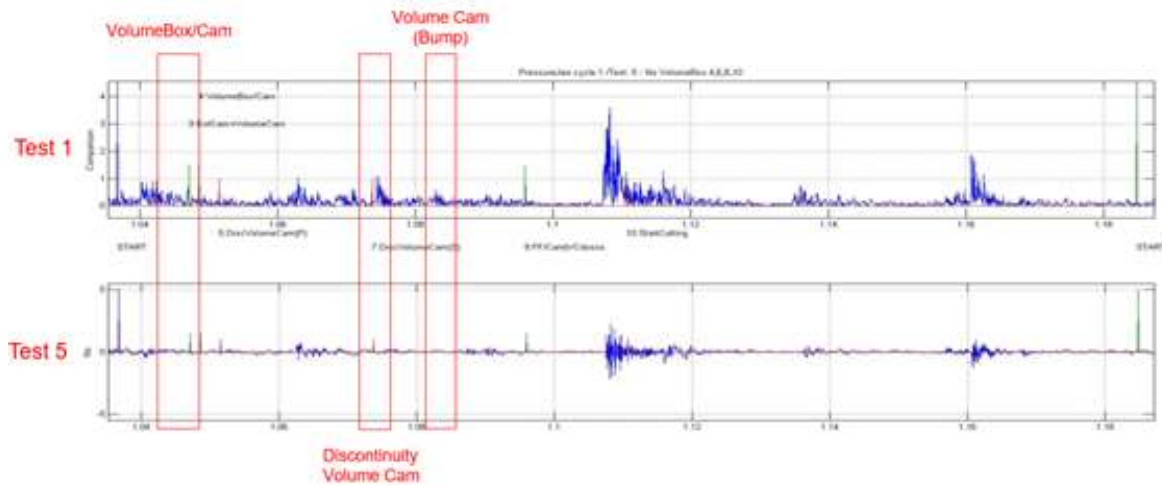


Figure 140: Vibration signals

As discussed in the previous Chapters, the cutting event is a relevant contributor to the vibration of the *Frame*, due to the intensity of the forces applied during the cutting cycle.

The Test 6 clearly showed that removing the *Cutting Bearing* a specific feature disappeared from the vibrational signal. The Figure 141 overlaps the vibration signals of the Test 1 (top graphic) and Test 6 (bottom graphic) showing that the absence of the cutting cycles produces a relevant variation of the signal, removing the stresses in the region highlighted by the red circle.

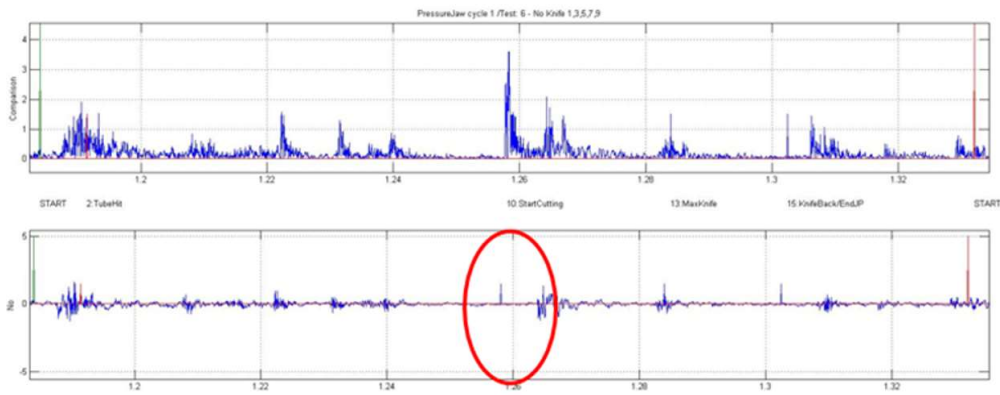


Figure 141: Absence of the stresses deriving from the cutting phase: comparison of Test 1 (top) and Test 6 (bottom)

A relevant observation that should be pointed out is that the cutting event detected in the test rig was mostly related to the impact between the *Cutting Cam* and the *Cutting Bearing*, since the test rig operates without the use of the packaging material, hence the cutting itself cannot be detected.

The first sequence of tests executed on the test rig highlighted that the best signal is provided by the *Pressure Side* accelerometer, since the peaks have a higher magnitude and can be more easily. The reason of this behaviour would be in the intrinsic characteristics of the *Frame*: the *Sealing Side* is connected to the power train, hence it has both an additional rigid connection to the *Frame* and the noises deriving from the gear box; the accelerometer in the *Knife Side* is oriented along the transversal direction, whilst the majority of the events have the major component oriented along its normal direction.

The Figure 142 overlaps the vibration signals provided by the three accelerometers during one complete rotation of the *Chain*, aiming to compare the magnitude of the vibrations detected by the different sensors for the same stressing events and identifying the position that would provide the best response and likelihood of detecting damages.

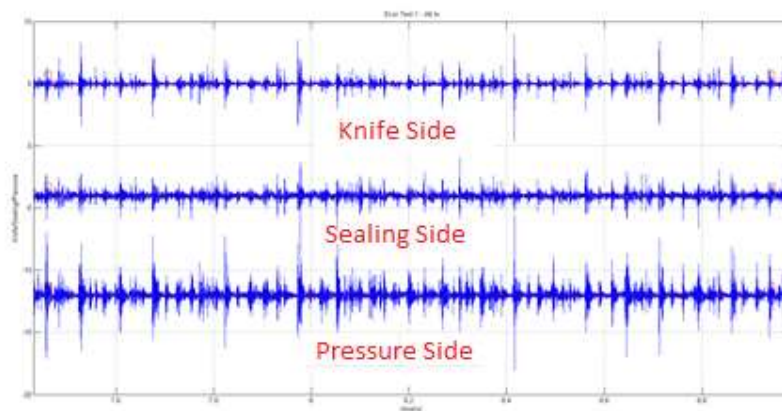


Figure 142: Accelerometers Comparison

8.6 Vibration Data: *Filling Machine*

The vibrations signals sampled in the complete *Filling Machine* operating with the product and the packaging material showed appeared slightly different from the one of the one measured on the test rig, highlighting the effect of the presence of the packages: new peaks related to the cutting phase and the activation of the folding flap mechanism have been identified and their magnitude of those peaks was higher than the average amplitude detected in the test rig, making cleared their detection [17].

The events with major differences were:

- Tube hit, because the Links meet the paper during this phase;
- Start cutting, of course the paper makes resistance;

- Jaw Pressure Application;
- Jaw Pressure release is the moment in which the package is release;
- Folding Flaps closed, when the flaps in the package are created.

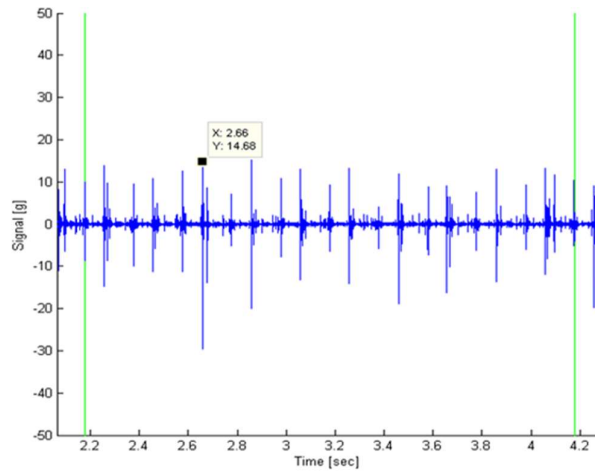


Figure 143: Vibration signal of a Filling Machine

Since the data collected from the *Filling Machine* (Figure 143) did not contain any reference about the position of the transversal link, neither the one of the encoder nor the one of the inductive sensor, the cross correlation algorithm was adopted for phasing the signals from the rig and the one from the field and overlapping the event sequence, that had been already phased in the previous step. The Figure 144 shows the result of the cross-correlation, that was used for shifting and aligning the vibration signal and the model of the physical events.

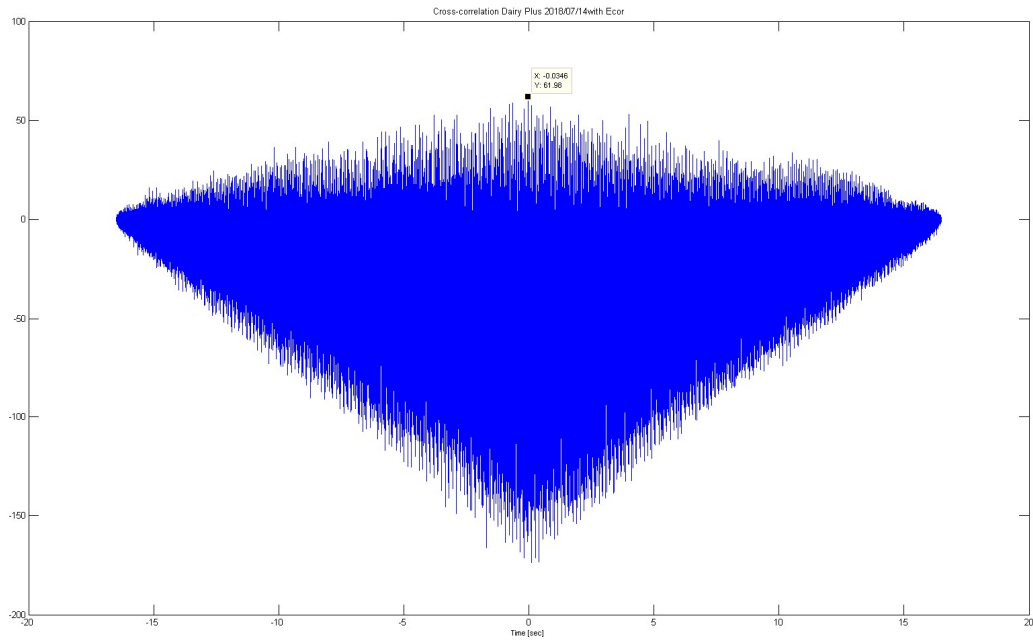


Figure 144: Cross-correlation algorithm

The Figure 145 shows the comparison of the signals collected on the rig (red) and on the standard equipment:

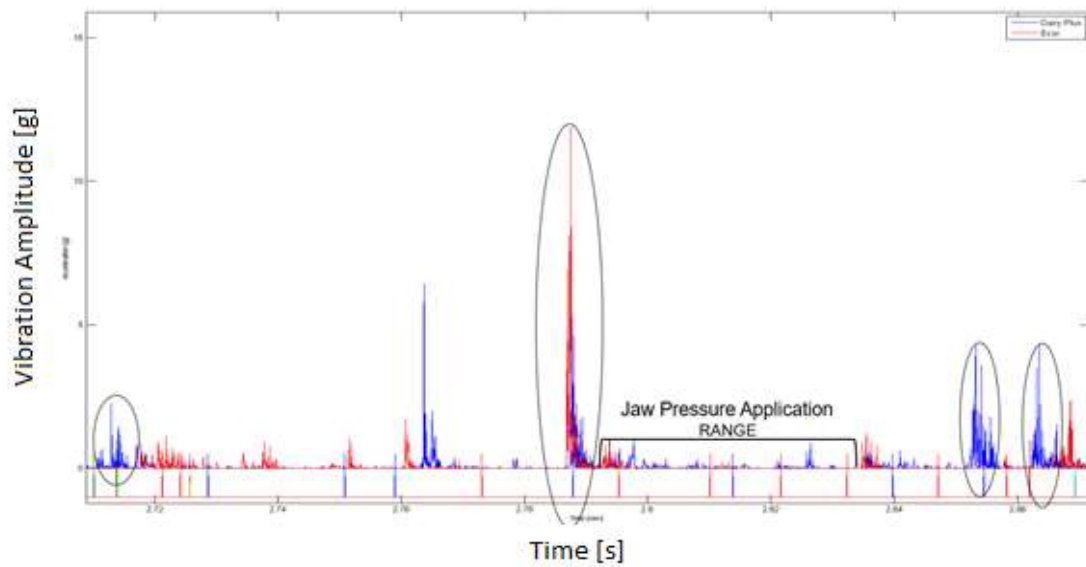


Figure 145: Overlapping of vibration signals from Test Rig and Filling Machine

The examination of the results achieved from the analysis of FMECA, field data, vibration signals, led to the identification of the failure modes that could be detected and predicted with higher probability of success.

- The criteria adopted for the selection were:
- Phenomenon characterized by a degrading trend
- Components influenced by lifetime shorter than expectations
- Components involved in the identified events

the components that will be investigated are:

- Ball bearing
- Inductors
- Cams

For the elements in the list, an additional testing campaign has been planned, aiming to compare the variations of the signals for different stages of degradation and the changes for the failed part, in order to identify and set the proper thresholds for the replacement.

8.7 Fault Injection

The creation of intentional damages of the *Jaw System* is a crucial phase for understanding the effects on the degraded component on the dynamic response of the equipment.

According with the prioritization defined in the previous paragraph, a new testing campaign was planned in the test rig, focalizing on specific failures.

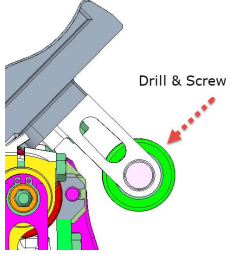


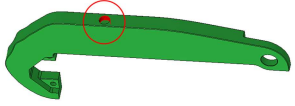
The components and the failure mode examined were:

Component	Failure Mode	Description
Roller Volume Box	Seizure	Due to the wear or the degradation of the coupled bushings, it can cause a severe wear of the Volume Cam
	Wear	In case of seizure the Roller slides on the metallic part of the Volume Cam. This can generate a failure even before the wear of the Volume Cam caused by the seizure
Main Cam	Surface fatigue	The cyclic stresses applied during the Clamping/Cutting phase in conjunction with the environmental stresses and principle of corrosion might cause the creation of surface fatigue
Volume Cam	Spot facing enlargement	In some equipment the contact between the Volume Box and the Volume Cam starts close to a spot facing, that when enlarges its diameter because of the cyclic impacts of the roller, modifies the

		impact angle and generates increased stress in the weakest section of the Volume Box
Side Roller	Seizure	In case of seizure it determines a permanent damage of the Main Cam, creating a track along its trajectory
Cam Follower	Seizure	In case of seizure of the ball bearing, it slides on the cam, and might create additional issues

Table 16: Fault Injection Tests

The standard components were modified as follows:

Component	Failure Mode	Description
Roller Volume Box	Seizure	 A 3D CAD model of a roller volume box assembly. A red dashed arrow points to a hole in the roller, labeled "Drill & Screw".
	Wear	 A 3D CAD model of a roller volume box assembly, similar to the one above, but with a green highlight on the roller's surface indicating wear.
Main Cam	Surface fatigue	 A photograph of a metal cam component. The surface shows dark, irregular marks and a rough texture, indicating surface fatigue.
Volume Cam	Spot facing enlargement	 A 3D CAD model of a green volume cam. A red circle highlights a specific area on the cam's surface, indicating a spot facing enlargement.

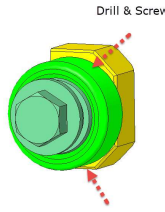
Side Roller	Seizure	
Cam Follower	Seizure	TBD

Table 17: Fault execution

Despite the amount of trials planned, only few tests could be executed due to the closure and the limitation of the accessed to the plant imposed by the pandemic virus COVID-19.

Before starting the testing campaign, the test rig was completely restored, in order to recreate a reliable baseline of the system.

The trials were executed by running the system in a steady state condition, after 30 min of warm-up, in order to avoid any transient phase for the mechanisms and each run was repeated 10 times.

Seized Roller Volume Box

The analysis of the signal of this test were focused on the partition of the vibration signal containing the time frame when the seized roller was in contact with the *Volume Cam*.

It should be notices that even sampling a reduced window of the signal, these sections contains anyhow the contribute of all rollers that are in contact with the *Volume Cam*, the one before in the starting frame of the window and the one after at the end of the window.

The graphic in the Figure 145 shows the boxplot of the signal, sampled according to the length of those windows and associate it to the specific *Transversal Link*

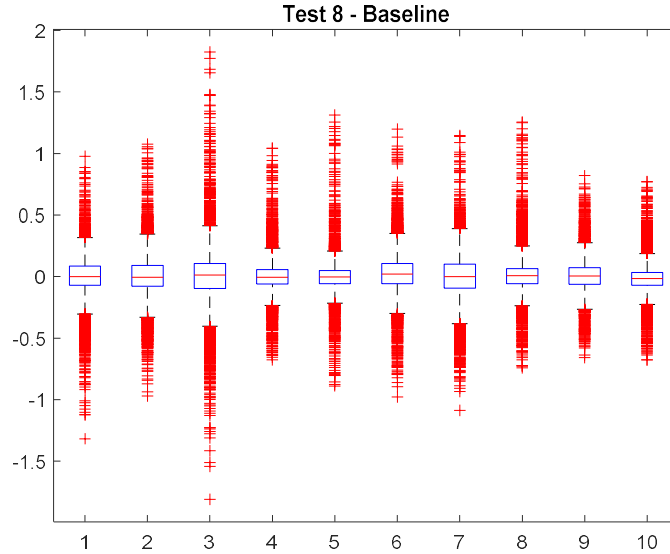


Figure 146: Box Plot of Vibration Signal along the Volume Cam

Although the data collected in each boxplot represents an average value of more *Transversal Links*, it can be noticed that the dispersion of the signal in the Position #3 is higher than the other, suggesting the occurrence of more intense impulses that in the other cases. The Position 3 corresponds to the *Transversal Link* carrying the damaged component.

Analysing the signal entire signal in the time domain and focusing on the window where the *Transversal Link* #3 is in contact with the *Volume Cam* (from $R=303$ to $R=0.9$), it was noticed that the more intense vibration is generated close to the last contact positions, which reflect the last impulsive contacts estimated with the dynamic model (see Figure 137).

The analysis of this fault was completed by monitoring the RMS value of the signal for each window associated to the contact between the roller and cam.

An interesting finding came from the comparison of this value between the Baseline Test, executed with the restored test rig, and the actual test.

The reference trend in the plot is the black one and it was noticed that in all runs executed in this configuration the value of the RMS associated to that *Transversal Link* was shifted in the bottom part of the plot.

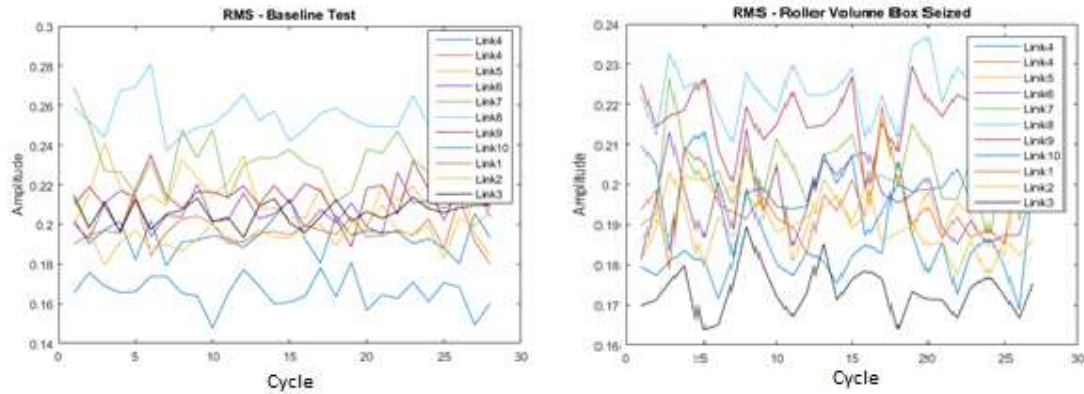


Figure 147: RMS Comparison

Such result was not expected, and it might be justified by a smoother movement between in condition of sliding between the external race of the roller, that has a well finished surface and an high hardness and the polymeric cam, instead of the case of the dynamic friction between the bushing installed into the roller and its shaft. Nevertheless, it should be underlined that in the test rig there is not the load deriving from the package, hence this behaviour should to be verified in the real operative conditions, since the action of the forming load might produce the opposite effect.

The test was used also for verifying the proper response of the cross-correlation function, when applied on the signal produced by the same mechanical system with and without the presence of a damaged part.

The algorithm was applied on the signals related to the Baseline Test and the actual one, and once the signal was shifted according with the result of the cross-correlation, the two signals appeared properly matching, hence it was concluded that this approach would provide reliable results also in presence of the seizure of the roller on the *Volume Box*.

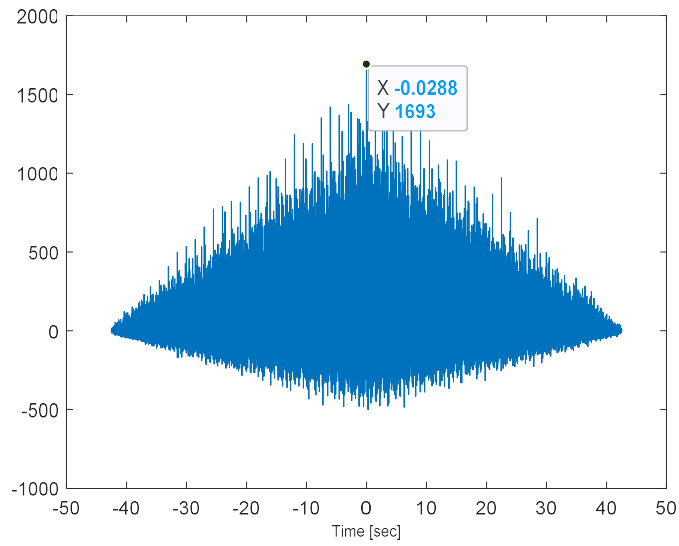


Figure 148: Cross-Correlation Test with fault and baseline

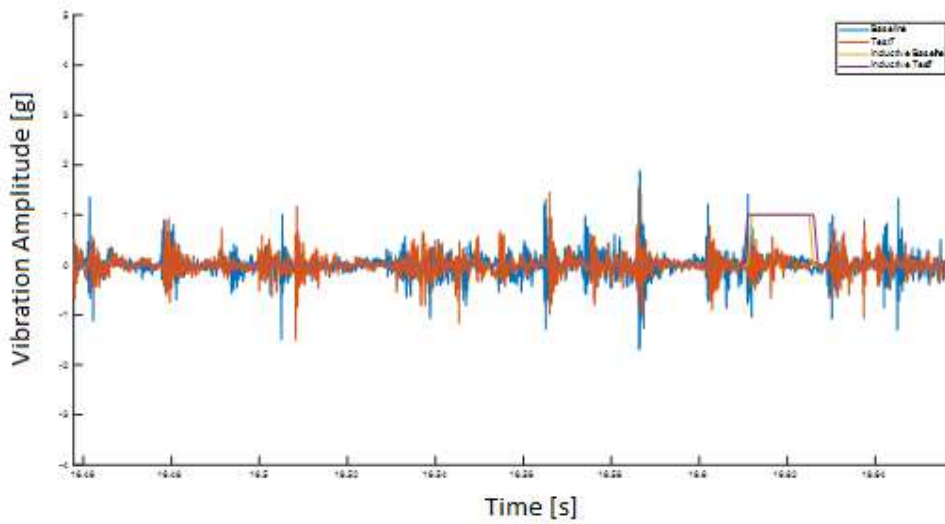


Figure 149: Overlapping of cross-correlated signals

9 Conclusion

The study showed that delivering reliable systems requires a methodological approach, that should integrate all the phases of the developing process, correlating theoretical information, measurements and data provided from the field, in order to deeply understand the behaviour of the equipment and to ensure its quality.

The creation and the validation of the virtual model was a fundamental step for the identification of the potential criticalities of the equipment, setting the proper monitoring tactic and defining the stressing factors to be adopted during the internal tests.

The dynamic model provided a good representation of the real behaviour of the equipment and its validation was mostly based on the correlation of the calculated and measured values of the forces applied on a shaft carrying a ball bearing of the *Transversal Links*. The process required the manufacturing of both a test rig and special parts equipped with strain gauges.

The customized sensors captured the evolution of the stresses applied on the *Transversal Links* of the *Chains* due to the interactions with the *Cams* and the elements along the motion trajectory (Figure 150), which was crucial for tuning the contact parameters adopted in the dynamic model. The Table 18 summarizes the optimized values:

Body 1	Body 2	Stiff. [$\frac{kN}{mm}$]	Damp. [$\frac{Ns}{mm}$]	Exp.	Pen. Depth [mm]	μ_s	μ_d
Ball Bearing	Main Cam	85	55	1.50	0.1	0.3	0.05
Ball Bearing	Vol. Cam	4	13	1.9	0.1	0.15	0.08
Ball Bearing	Tensioner	3.7	20	1.8	0.1	0.13	0.08
Shaft	Wheel	5	50	1.55	0.1	0.13	0.09
Roller	F.F. Cam	5	50	1.55	0.1	0.13	0.09
Ball Bearing	Cut. Cam	90	55	1.50	0.1	0.3	0.05
Folding Flap	Pin	85	55	1.50	0.1	-	-
Volume Box	Damper	2.5	90	1.05	0.1	-	-

Table 18: Contact Parameters

The measurements on the test rig presented a good matching with the simulation, highlighting some deviations that might be generated on the system due to the manufacturing process of the mechanism.



Figure 150: Overlapped curves of measured and calculated Forces on the Transversal Links

The customized sensors installed in the cutting mechanism allowed the possibility of studying the evolution of the force during a cutting cycles (Figure 151), highlighting the contribute of the most relevant subphases of the process and providing the data set that was implemented into the dynamic model for achieving an accurate simulation of the contributes of the cutting process to the overall response of the *Jaw System*.

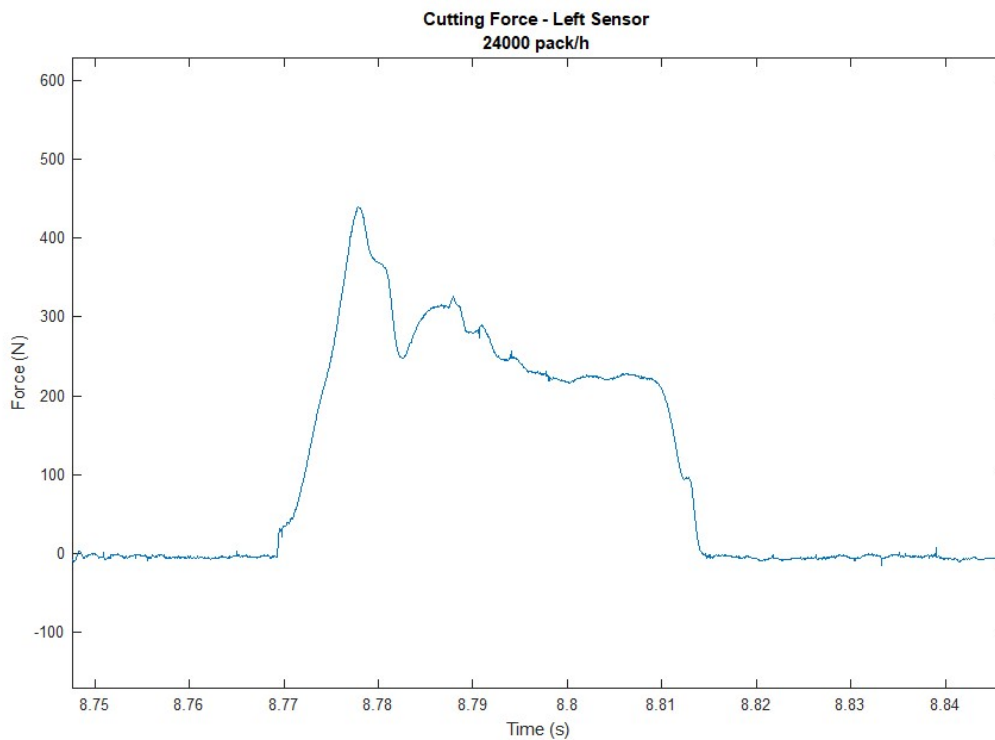


Figure 151: Measured Cutting Force on one Cutting Bearing

The tuned dynamic model was used for investigating the operating conditions of the *Jaw System* out of the nominal ones, which represent undesired events related to the breakage, the

damage or the wear of components of the mechanical system, such as the springs of the *Tensioner* and the one of the *Volume Box*, the *Damper* of the *Volume Box* and the *Stop Pin* of the *Folding Flap Mechanism*.

The cutting subsystem was experimentally investigated in detail, focusing on the parameters that mostly influence the cutting efficiency, analysed through the values of the maximum force required for separating the packaging material during the standard functioning of the *Filling Machine*. The investigation campaign required the design and manufacturing of a testing equipment able to emulate the real stresses and to manage the variables of the cutting process: clamping force, pulling force, sealing heat power, duration and cooling time, type of filled product into the packages. The results were achieved by the defining a design of experiments on 5 parameters at 3 stressing levels, according with the Taguchi Methodology. The results (Figure 152) of the study provided fundamental results for the understanding of the process.

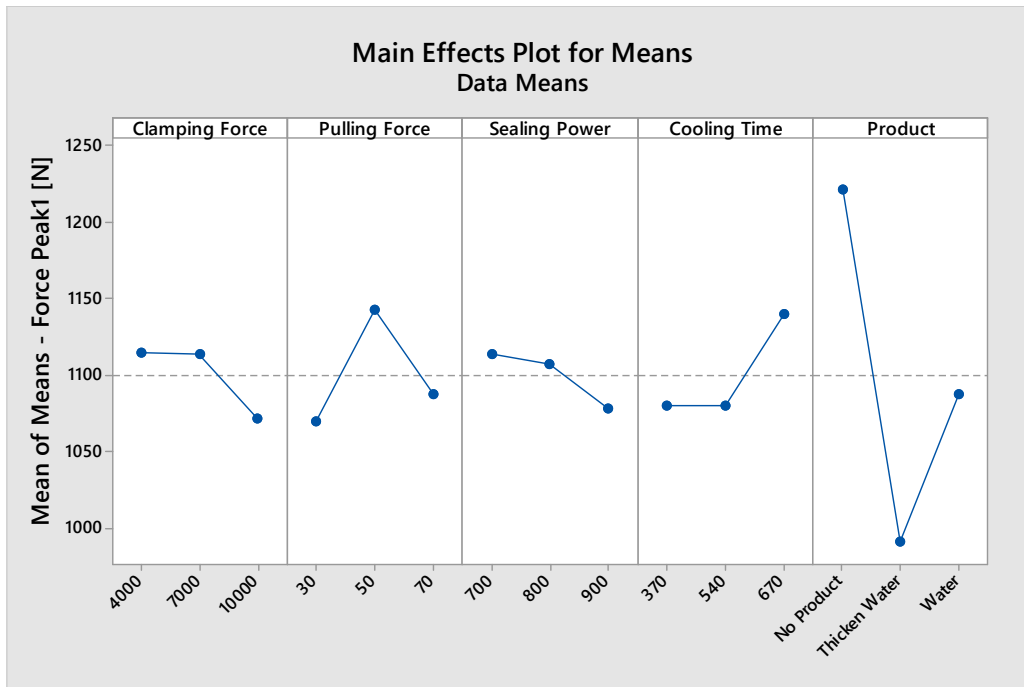


Figure 152: Main Effect Plot of Cutting Parameters

The test rig was used for executing a lifetime test on different versions of the knives as well, in order to investigate the geometrical wear of the blade and the degradation of the cutting performances. The test was still running at the time of the publication of this work, but the preliminary results showed that the 3D scansion for investigating the wearing process is the most accurate method for analysing this topic and that the variation of the peak cutting force is

the most accurate parameter to be monitored and correlated to the degradation process (Figure 153).

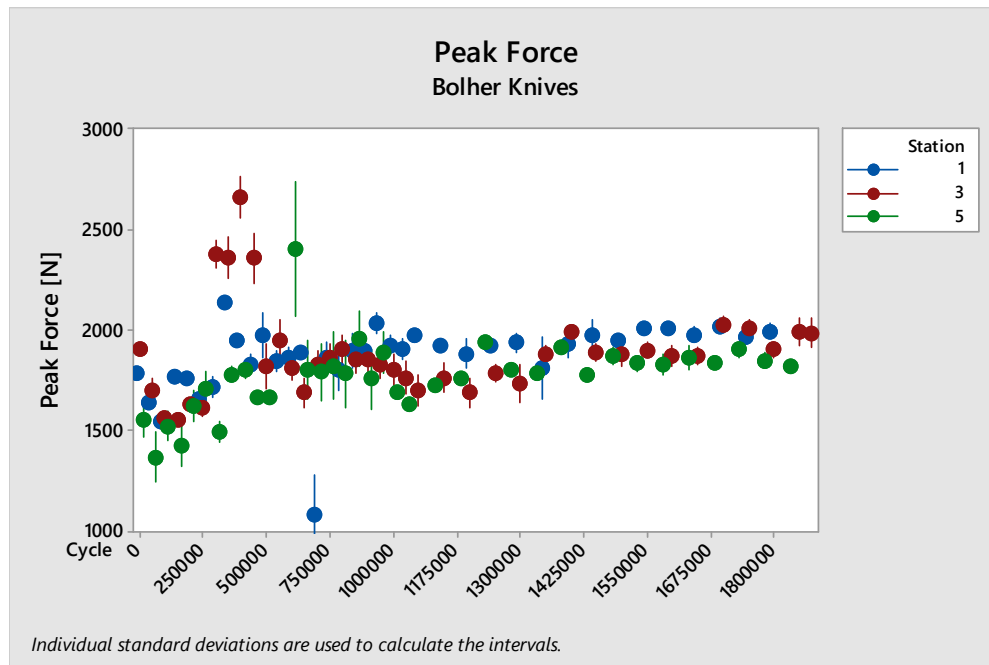


Figure 153: Peak Force Trend

A test rig was designed and developed for testing the ball bearings with a mission profile that was obtained starting from the experimental measurements and optimized for accelerating the test and reducing its duration.

The test run provided information about the lifetime performances of the component, highlighting the differences between the responses of two types of ball bearing manufactured by different suppliers (Figure 154).

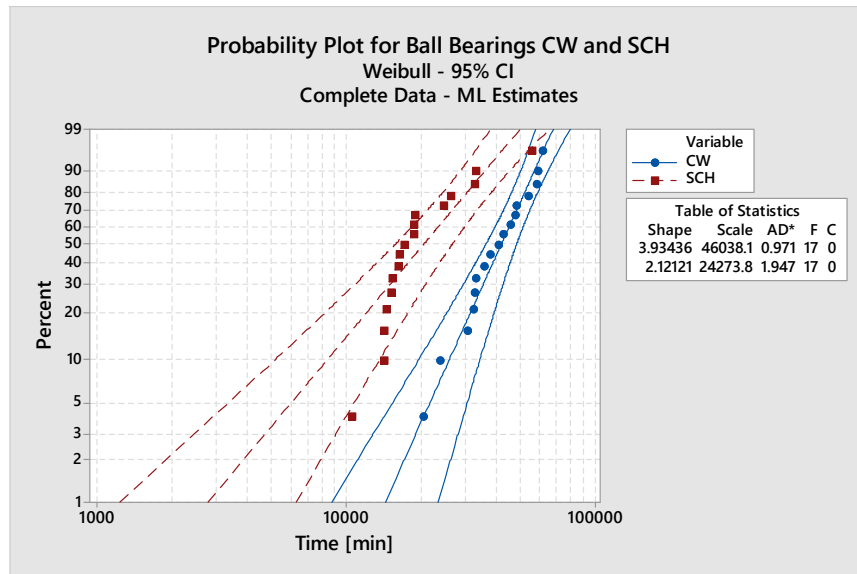


Figure 154: Lifetime distributions of ball bearings

The analysis of the vibration spectrum of the bearing (Figure 155) clearly showed the deterioration of the specimens, highlighting that in the majority of the cases the failure of the ball bearing started from a defect on the external race and it was strongly influenced by the degradation of the grease and the occurrence of corrosive phenomena.

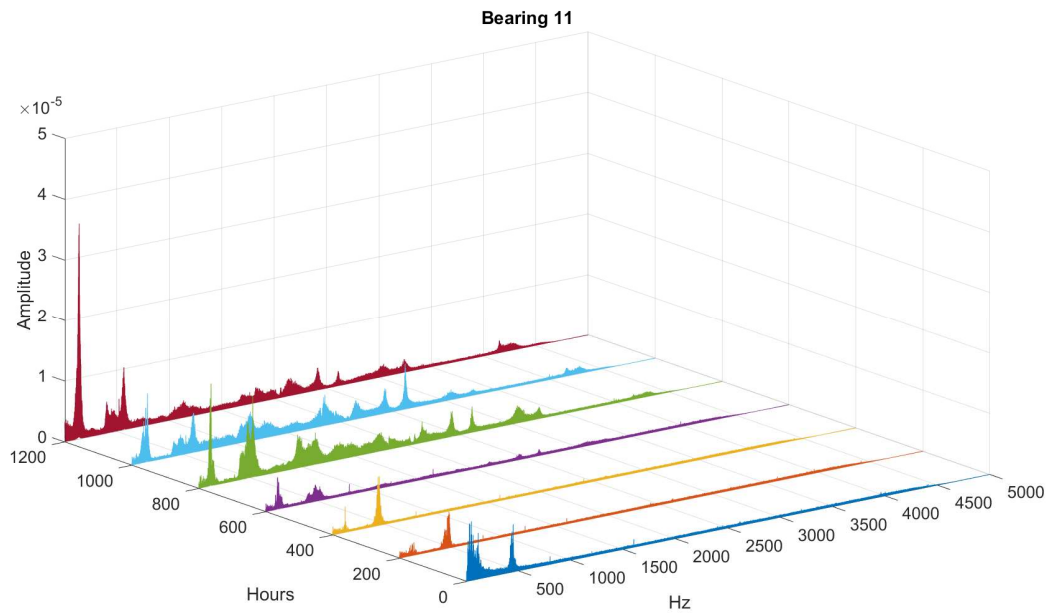


Figure 155: Vibration Spectrum of the Specimen 11 at different testing stages

The last part of the work focused on the analysis of the vibration signals collected on the test rig and on the field and their correlation with the major stressing events that characterize the

operation cycle of the *Chains* in the *Jaw System*. The investigation led to the correct interpretation of the vibration signals and to the identification of the component that can be monitored with higher probability of success for the diagnosis of system and the implementation of predictive maintenance tactics.

The future stages of the analysis would involve all the different tracks described in the present work, by:

- completing the experimental measuring campaign of the forces exchanged between the mechanisms of the *Jaw System*;
- proceeding with the lifetime testing of the knives and monitoring the degradation trend, focusing on multiple parameters (e.g. cutting work, shape of the cutting curve, cutting slope, etc.);
- concluding the creation of the simplified cutting model and validating it;
- continuing the testing sequence of injected faults
- investigating the dynamic response of the frame of the *Jaw System* by the application of Transfer Path Analysis techniques, in order to increase the accuracy of the detection and the prediction of specific damages.

10 References

- [1] Tanninen, P., Leminen, V., Matthews, S., Kainusalmi, M., Varis, J., *Process cycle optimization in press forming of paperboard*, Packaging Technology and Science, 31 (5), pp. 369-376, 2018. DOI: 10.1002/pts.2331
- [2] Golzar, M., Ghaderi, A., *Effect of temperature on the spring back of cellulose-based sheet in hot pressing*, International Journal of Advanced Manufacturing Technology, 42 (7-8), pp. 633-642, 2009. DOI: 10.1007/s00170-008-1626-y
- [3] Zippo, A., Barbieri, M., Iarriccio, G., Pellicano F., *Nonlinear vibrations of circular cylindrical shells with thermal effects: an experimental study*, Nonlinear Dynamics, (in press), 2019. <https://doi.org/10.1007/s11071-018-04753-1>.
- [4] Zippo, A., Barbieri, M., Pellicano, F. *Temperature gradient effect on dynamic properties of a polymeric circular cylindrical shell*, Composite Structures, 216, pp. 301-314, 2019. DOI: 10.1016/j.compstruct.2019.02.098
- [5] Sapietová, A., Dekýš, V., *Dynamic analysis of rotating machines in MSC.ADAMS*, Procedia Engineering, 136, pp. 143-149, 2016. DOI: 10.1016/j.proeng.2016.01.188
- [6] Arbor, A., Negrut, D., Dyer, A., *ADAMS/Solver primer*, Simulation Based Engineering Lab University of Winsconsin website, 2004
- [7] Margarida Machado, Pedro Moreira, Paulo Flores, Hamid M. Lankarani, *Compliant contact force models in multibody dynamics: Evolution of the Hertz contact theory*, Mechanism and Machine Theory 53 pp. 99–121, 2012.
- [8] Friedrich Pfeiffer *, Martin Foerg, Heinz Ulbrich, *Numerical aspects of non-smooth multibody dynamics*, Comput. Methods Appl. Mech. Engrg. 195, pp. 6891–6908, 2006.
- [9] M. Jean, *The non-smooth contact dynamics method*, Comput. Methods Appl. Mech. Engrg. 177, pp. 235-257, 1999.
- [10] T. Klisch, *Contact mechanics in multibody systems*, Mechanism and Machine Theory 54 pp. 665-675, 1999.
- [11] Binder, R.C., *Mechanics of the roller chain drive: Based on mathematical studies by R.C. Binder*, Prentice-Hall, Upper Saddle River, New Jersey, 1956.
- [12] Flores, P., Claro, J.C.P., Ambrósio, J., Lankarani, H.M. and Koshy, S., *Study of Contact-Impact Force Models in Multibody Mechanical Systems*, Tenth Conference on Nonlinear

Vibrations, Stability, and Dynamics of Structures, Virginia Polytechnic Institute and State University, July 25-29, 2004.

- [13] P. Alart, A. Curnier, *A mixed formulation for frictional contact problems prone to Newton like solution methods*, Computer Methods in Applied Mechanics and Engineering 92 553-375, North-Holland, 1991.
- [14] Borsari, R., Dunge, F., *Functional design and kinematic synthesis of a chain driven high-speed packaging machine*, Company internal documentation, Tetra Pak Packaging Solutions S.p.A, 2000.
- [15] Shabana, *Dynamics of Multibody Systems*, Fourth Ed., 2013, Cambridge University Press.
- [16] H. Fleischmann, J. Kohla and F. Jörg, *A Modular Architecture for the Design of Condition Monitoring Processes*, Elsevier, 2016.
- [17] J. Lee, B. Bagheri and H. Kao Kao, *A Cyber-Physical Systems architecture for Industry 4.0-based manufacturing systems*, Manufacturing Letters, 2015.
- [18] Gelman, L., Harish Chandra, N., Kurosz, R., Pellicano, F., Barbieri, M., Zippo, A., *Novel spectral kurtosis technology for adaptive vibration condition monitoring of multi-stage gearboxes*, Insight: Non-Destructive Testing and Condition Monitoring, 58 (8), pp. 409-416, 2016. DOI: 10.1784/insi.2016.58.8.409.
- [19] Aditya*, M. Amarnath, P.K. Kankar, *Failure Analysis of a Grease-Lubricated Cylindrical Roller Bearing*, 2nd International Conference on Innovations in Automation and Mechatronics Engineering, ICIAME 2014
- [20] M.D. Haneef*, R.B. Randall, W.A. Smith, Z. Peng, *Vibration and wear prediction analysis of IC engine bearings by numerical Simulation*, Wear 384–385, 2017.
- [21] S. F.Ochoa, G. Fortino and G. Di Fatta, *Cyber-physical systems, internet of things and big data*, elsevier, 2017.
- [22] H. Fleischmann, J. Kohla and J. Frankea, *A Modular Architecture for the Design of Condition Monitoring Processes*, in 49th CIRP Conference on Manufacturing Systems, Erlangen, Germany, 2016.
- [23] A. K.S.Jardine, D. Lin and D. Banjevic, *A review on machinery diagnostics and prognostics implementing condition-based maintenance*, Elsevier, 2006.

- [24] R. B. Randall, *Vibration-based Condition Monitoring: Industrial, Aerospace and Automotive Applications*, John Wiley & Sons, 2011.
- [25] JayLee, F. Wu, W. Zhao, M. Ghaffari, L. Liao and D. Siegel, *Prognostics and health management design for rotary machinery systems—Reviews, methodology and applications*, *Mechanical Systems and Signal Processing*, vol. 42, no. 1-2, pp. 314-334, 2014.
- [26] M. Cocconcelli, L. Capelli, J. C. C. Molano and D. Borghi, *Development of a methodology for condition-based*, *Machines*, 21 March 2018.
- [27] A. BOUTI and D. A. KADI, *A State-Of-The-Art Review Of Fmea/Fmeca*, *International Journal of Reliability, Quality and Safety Engineering*, pp. 515-543, 1994.
- [28] Montgomery D.C, *Design and Analysis of Experiments*, Eighth Ed. Wiley, 2013.
- [29] Bernardino Chiaia, *Fracture mechanism induced in a brittle material by hard cutting indenter*, *International Journal of Solid and Structures* 38, pp. 7747-7768, 2001.
- [30] S. Mezlini a,*, Ph. Kapsa a, J.C. Abrya, C. Henonb, J. Guillemenet, *Effect of indenter geometry and relationship between abrasive wear and hardness in early stage of repetitive sliding*, *Wear* 260, pp. 412–421, 2006.
- [31] D. Gasioreka, P. Baranowskib, J. Malachowskib,*, L. Mazurkiewicz, M. Wiercigroch, *Modelling of guillotine cutting of multi-layered aluminum sheets*, *Journal of Manufacturing Processes* 34, pp. 374–388, 2018.
- [32] Jaroslav Čech *, Petr Haušild, Ondřej Kovářík, Aleš Materna, *Examination of Berkovich indenter tip bluntness*, *Materials and Design* 109, pp. 347–353, 2016.
- [33] S. Schuldt*, G. Arnold, J. Kowalewski, Y. Schneider, H. Rohm, *Analysis of the sharpness of blades for food cutting*, *Journal of Food Engineering* 188, pp. 13-20, 2016.
- [34] K.H. Laua, D. Meib, C.F. Yeunga,*, H.C. Ma, *Wear characteristics and mechanisms of a thin edge cutting blade*, *Journal of Materials Processing Technology* 102, pp. 203 - 207, 2000.
- [35] Tim Brown *, Stephen J. James, Graham L. Purnell, *Cutting forces in foods: experimental measurements*, *Journal of Food Engineering* 70, pp. 165–170, 2005.
- [36] C.T. McCarthy a,*, A. Ní Annaidh b, M.D. Gilchrist b, *On the sharpness of straight edge blades in cutting soft solids: Part II – Analysis of blade geometry*, *Engineering Fracture Mechanics* 77, pp. 437–451, 2010.

- [37] S. Schuldt, G. Arnold, J. Roschy, Y. Schneider, H. Rohmn, *Defined abrasion procedures for cutting blades and comparative mechanical and geometrical wear characterization*, *Wear* 300, pp. 38–43, 2013.
- [38] G.A. Reilly, B.A.O. McCormack, D. Taylor, *Cutting sharpness measurement: a critical review*, *Journal of Materials Processing Technology* 153–154, pp. 261–267, 2004.